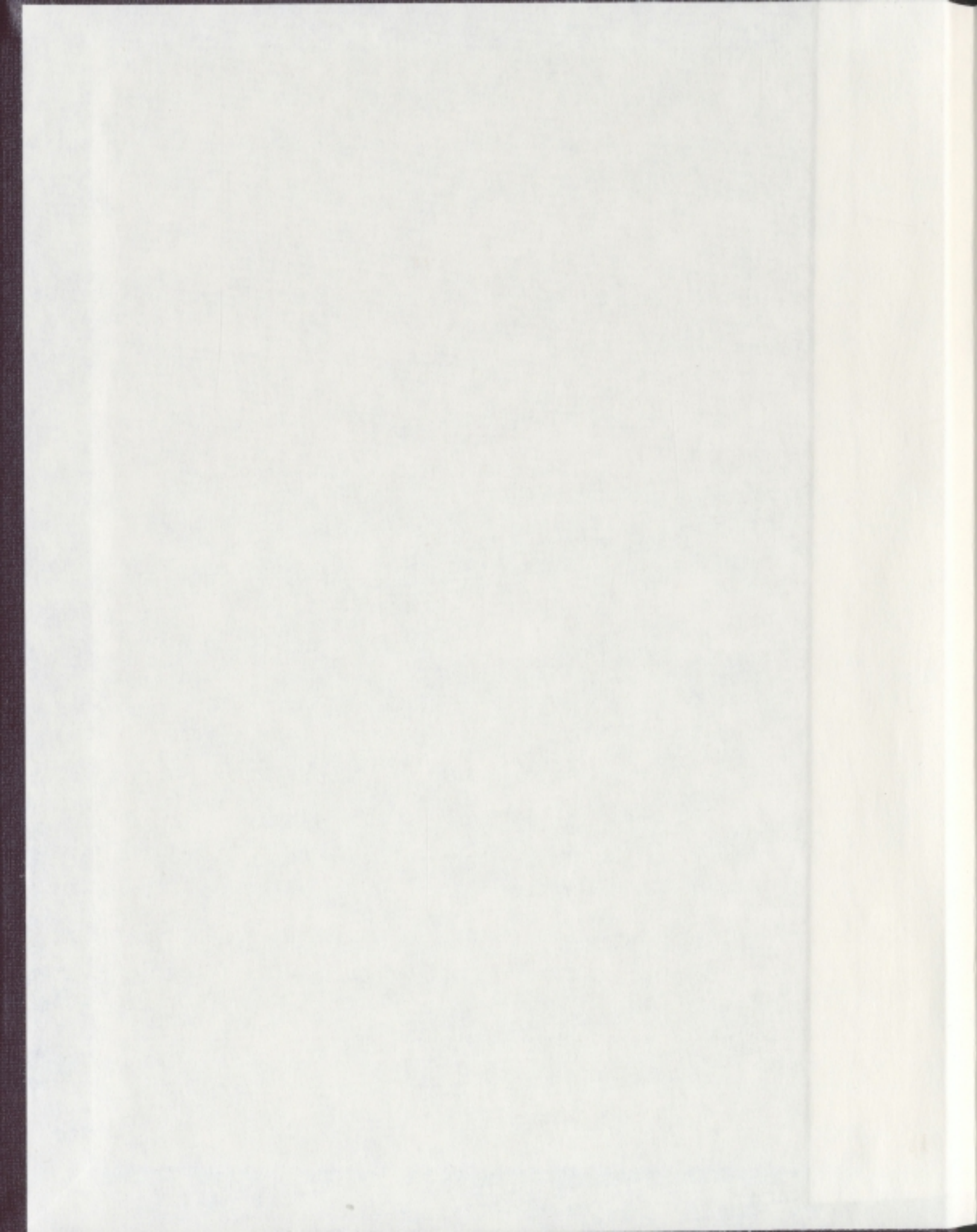


ICEBERG AND SHIP DETECTION AND  
CLASSIFICATION IN SINGLE, DUAL AND QUAD  
POLARIZED SYNTHETIC APERTURE RADAR

CARL HOWELL









Library and Archives  
Canada

Published Heritage  
Branch

395 Wellington Street  
Ottawa ON K1A 0N4  
Canada

Bibliothèque et  
Archives Canada

Direction du  
Patrimoine de l'édition

395, rue Wellington  
Ottawa ON K1A 0N4  
Canada

*Your file Votre référence*  
ISBN: 978-0-494-80860-3  
*Our file Notre référence*  
ISBN: 978-0-494-80860-3

#### NOTICE:

The author has granted a non-exclusive license allowing Library and Archives Canada to reproduce, publish, archive, preserve, conserve, communicate to the public by telecommunication or on the Internet, loan, distribute and sell theses worldwide, for commercial or non-commercial purposes, in microform, paper, electronic and/or any other formats.

The author retains copyright ownership and moral rights in this thesis. Neither the thesis nor substantial extracts from it may be printed or otherwise reproduced without the author's permission.

In compliance with the Canadian Privacy Act some supporting forms may have been removed from this thesis.

While these forms may be included in the document page count, their removal does not represent any loss of content from the thesis.

#### AVIS:

L'auteur a accordé une licence non exclusive permettant à la Bibliothèque et Archives Canada de reproduire, publier, archiver, sauvegarder, conserver, transmettre au public par télécommunication ou par l'Internet, prêter, distribuer et vendre des thèses partout dans le monde, à des fins commerciales ou autres, sur support microforme, papier, électronique et/ou autres formats.

L'auteur conserve la propriété du droit d'auteur et des droits moraux qui protège cette thèse. Ni la thèse ni des extraits substantiels de celle-ci ne doivent être imprimés ou autrement reproduits sans son autorisation.

Conformément à la loi canadienne sur la protection de la vie privée, quelques formulaires secondaires ont été enlevés de cette thèse.

Bien que ces formulaires aient inclus dans la pagination, il n'y aura aucun contenu manquant.

Canada



Iceberg and ship detection and classification  
in single, dual and quad polarized  
synthetic aperture radar

by  
© Carl Howell, B.Sc.

A thesis submitted to the School of Graduate Studies  
in partial fulfillment of the requirements for the degree of  
Master of Science

Computational Science Program  
Memorial University of Newfoundland

May 2008

## **Abstract**

Iceberg and ship identification in satellite synthetic aperture radar (SAR) data is an essential part of offering an operational iceberg surveillance program. Identification here refers to detection of ocean SAR targets and then classification of these targets as iceberg, ship, or unknown. Maximizing the detection and minimizing incorrect classification of iceberg and ship targets are required. Because coarser resolution satellite SAR data is at times not as intuitive as satellite optical data for manual human interpreted target classification, this process can be labor intensive, subjective, and error prone. Therefore, it is desired that an automated method for iceberg or ship identification be implemented. The methodology investigated here follows a well known standard in supervised pattern recognition, the maximum likelihood-quadratic discriminant function. The goal here in this thesis is to build class models from known iceberg and ship targets. Each class model is based on features that describe targets such as brightness, texture, and shape. Based on these descriptors as training input into the discriminant functions, future unknown targets can be compared with the class model for best fit. The best fit (or minimum distance) is used to assign class status for these unknown targets. One major consideration when using this type of pattern recognition approach is feature selection. Feature selection is based on the notion that some subset (subspace) of the descriptive metrics will lead to improved classification accuracy when comparing discriminant functions. Sequential forward selection and variants of exhaustive search algorithms are implemented and compared. RADARSAT-1, ENVSIAT AP (HH/HV), and EMISAR SAR iceberg and ship targets are used for algorithm training, feature selection, and performance estimation.

## Acknowledgments

This thesis would not have been possible without support from several sources. First, my wife, Andrea, and son, Andrew who have sacrificed many nights and weekends, to you I am eternally grateful for your love and support. Second, to my supervisors Andy Foster (Math and Statistics) and Ray Gosine (Engineering), their guidance and persistence has led the way to stitching a collaborative mixture of course, project, and self guided work together. Third, to my fellow C-CORE employees, especially Des Power, James Youden, Kelley Dodge, Thomas Puestow, Sherry McHugh, Julien Choisnard, Jamie Warren, Baxter Smith, and Jason Mills. Your collaborative support in the technical aspects of SAR, remote sensing, image processing, and pattern recognition went along way to achieving the current capabilities and level of understanding of the problem at hand. Finally, thank you to the investments made by C-CORE and its clients and partners, the Canadian Ice Service (CIS), the International Ice Patrol (IIP), Provincial Airlines Limited (PAL), Petro-Canada, Chevron Canada Resources, Husky Oil, Norsk Hydro Canada, ExxonMobil Canada, Program of Energy Research and Development (PERD), MacDonald Dettwiler and Associates (MDA), Canadian Space Agency (CSA) and the European Space Agency (ESA) who supported the development of operational iceberg and ship SAR surveillance initiatives.

# Table of Contents

Abstract .....	i
Acknowledgments.....	ii
Table of Contents .....	iii
List of Tables .....	vi
List of Figures .....	vii
List of Abbreviations and Symbols.....	viii
List of Appendices .....	x
1      Introduction.....	1
1.1 <i>Purpose of Study</i> .....	2
2      Relevant Background.....	4
2.1 <i>Fundamentals of Radar</i> .....	4
2.1.1    Synthetic Aperture Radar.....	5
2.1.2    SAR Ocean Backscatter.....	7
2.1.2.1   Processing Ocean Backscatter for Target Detection using CFAR.....	8
2.1.3    Physical Properties of Iceberg Backscatter.....	12
2.1.4    Physical Properties of Ship Backscatter .....	14
2.2 <i>Digital Image Processing and Analysis</i> .....	17
2.2.1   Target Detection.....	17
2.2.2   Local/Adaptive Threshold and CFAR .....	20
2.2.3   Region Growing.....	21
2.2.4   Feature Extraction.....	23
2.3 <i>Pattern Recognition</i> .....	23
2.3.1   Bayesian Decision Theory .....	24
2.3.1.1   Maximum Likelihood: a Quadratic Discriminant Function.....	24
2.3.2   Feature Selection.....	25
2.3.2.1   Sequential Forward Selection .....	26
2.3.2.2   Exhaustive Search .....	26
2.3.3   Discriminant Performance .....	28
2.4 <i>Previous Works</i> .....	29
2.4.1   Marthaler's Iceberg and Ship Detection with SLAR.....	29
2.4.2   Vachon's Ship Detection with SAR .....	31
2.4.3   C-CORE's Iceberg Detection with SAR.....	32

2.4.4	Haykin's Remote Sensing of Iceberg, Ship, and Sea Ice Targets.....	33
2.4.4.1	The Detection of Ship Targets by Ground Radar .....	34
2.4.4.2	Bayesian Classification of Icebergs and Sea Ice.....	35
3	SAR Iceberg and Ship Target Detection.....	37
3.1	<i>Data</i> .....	37
3.1.1	RADARSAT-1.....	37
3.1.2	ENVISAT .....	38
3.1.3	EMISAR .....	39
3.2	<i>Target Detection and Correlation</i> .....	40
3.2.1	RADARSAT-1.....	40
3.2.2	ENVISAT .....	43
3.2.3	EMISAR .....	47
4	SAR Iceberg and Ship Target Discrimination .....	52
4.1	<i>RADARSAT-1</i> .....	54
4.1.1	SFS 2-Class .....	54
4.1.2	ES 2-Class .....	55
4.1.3	ERS 2-Class.....	55
4.1.4	SFS 4-Class .....	55
4.2	<i>Discussion of RADARSAT-1 Results</i> .....	55
4.3	<i>ENVISAT AP HH/HV</i> .....	58
4.3.1	SFS 2- Class .....	59
4.3.2	ERS 2-Class.....	59
4.3.3	LES 2-Class.....	59
4.3.4	SFS 6-Class .....	59
4.4	<i>Discussion of ENVISAT AP HH/HV Results</i> .....	60
4.5	<i>EMISAR</i> .....	64
4.5.1	Quad Polarization with Cameron.....	65
4.5.2	Quad Polarization.....	65
4.5.3	Dual Polarization HH/HV .....	65
4.5.4	Dual Polarization HH/VV .....	66
4.5.5	Dual Polarization VH/VV .....	66
4.5.6	Single Polarization HH .....	67
4.5.7	Single Polarization VV .....	67
4.5.8	Single Polarization HH (without shape) .....	67
4.6	<i>Discussion of EMISAR Results</i> .....	67
5	Computational Considerations.....	71
5.1	<i>The Necessity for Cross Validation</i> .....	71
5.2	<i>Maximum Likelihood Mean and Covariance Calculation</i> .....	73

5.3	<i>Benchmarking Exhaustive Search</i> .....	74
5.4	<i>Variants of Exhaustive Search</i> .....	75
5.5	<i>Non-Intrusive Parallel Exhaustive Search</i> .....	77
6	Conclusion .....	80
6.1	<i>Future Work</i> .....	83
7	References.....	85
	Appendix I – Pseudo code algorithm for Sequential Forward Selection (SFS) .....	90
	Appendix II - Pseudo code algorithm for Exhaustive Search (ES) .....	91
	Appendix III - Pseudo code algorithm for Exhaustive Ranked Search (ERS) .....	92
	Appendix IV - Pseudo code algorithm for Limited Exhaustive Search (LES).....	93
	Appendix V - Pseudo code algorithm for Parallel Exhaustive Search (PES).....	94
	Appendix VI - Confusion Matrix Notation.....	95

## List of Tables

Table 3.1: Summary of RADARSAT-1 iceberg and ship data.....	43
Table 3.2: Summary of ENVISAT ASAR AP (HH/HV) iceberg and ship data. ....	47
Table 3.3: Summary of EMISAR iceberg and ship data. .....	51
Table 4.1: Summary of RADARSAT-1 iceberg and ship classification accuracy.....	57
Table 4.2: Summary of ENVISAT ASAR iceberg and ship classification accuracy. ....	63
Table 4.3: Summary of EMISAR iceberg and ship classification accuracy.....	70
Table 5.1: RADARSAT-1 validation methodologies.....	73
Table 5.2: ES benchmark for ENVISAT AP data. ....	76
Table AVI.1: Class confusion matrix for an $n$ class system.....	96

## List of Figures

Figure 2.1: Side-looking radar and variable incidence angle .....	6
Figure 2.2: Ocean Backscatter $\sigma^0$ for C-band VV and HH polarization [2] .....	9
Figure 2.3: ENVISAT ASAR histogram of ocean clutter in HH $\sigma^0$ .....	10
Figure 2.4: RADARSAT-1 SCW with variable ocean features .....	12
Figure 2.5: RADARSAT-1 Wide mode probability of detecting small icebergs [18]. ....	14
Figure 2.6: RADARSAT-1 S3 minimum detectable ship length [2]. ....	16
Figure 2.7: RADARSAT-1 Figure-of-merit for ship detection [2].....	16
Figure 2.8: EMISAR sample iceberg detection via histogram local minima. ....	18
Figure 2.9: ENVISAT ASAR ship detection via adaptive threshold.....	19
Figure 2.10: RADARSAT-1 ship target region growing example. ....	22
Figure 3.1: RADARASTA-1 imagery overview.....	40
Figure 3.2: RADARSAT-1 W3 icebergs.....	41
Figure 3.3: RADARSAT-1 W3 ships.....	42
Figure 3.4: ENVISAT ASAR AP (HH/HV) imagery overview.....	44
Figure 3.5: ENVISAT AP icebergs. ....	45
Figure 3.6: ENVISAT AP ships.....	46
Figure 3.7: EMISAR imagery overview.....	48
Figure 3.8: EMISAR HH icebergs.....	49
Figure 3.9: EMISAR HH ships.....	50
Figure 4.1: ENVISAT ASAR ES benchmark.....	53
Figure 4.2: RADARSAT-1 SFS – 4 class decision tree structure. ....	56
Figure 4.3: RADARSAT-1 feature selection comparison .....	58
Figure 4.4: SFS ENVISAT AP 6-Class decision tree structure. ....	60
Figure 4.5: ENVISAT ASAR HH/HV: Large iceberg and ship classification.....	61
Figure 4.6: ENVISAT ASAR feature selection comparison. ....	62
Figure 4.7: EMISAR quad polarization iceberg and ship classification.....	66
Figure 5.1: RADATSAT-1 accuracy for leave-one-out and re-substitution.....	72
Figure 5.2: Non-intrusive parallel exhaustive search (NIES) screen saver .....	79

## List of Abbreviations and Symbols

{ }	Set
AOI	area of interest
AP	alternating polarization, ASAR
ASAR	advanced synthetic aperture radar
CFAR	constant false alarm rate
CIS	Canadian Ice Service
CSA	Canadian Space Agency
dB	normalized unit-less intensity measure
DF	Discriminant Function
ERS	exhaustive ranked search
ES	exhaustive search
ESA	European Space Agency
$\phi$	wind direction relative to SAR sensor
FLAR	forward-looking airborne radar
GIS	geographic information system
HDC	High detection confidence, IDS
HH	horizontal send / horizontal receive polarization
HV	horizontal send / vertical receive polarization
IDS	iceberg detection software
IIP	International Ice Patrol
IS	image swath
IM	single polarization, ASAR
LDC	Low detection confidence, IDS
LES	limited exhaustive search
MDA	MacDonald Dettwiler and Associates
MDC	Medium detection confidence, IDS
NESZ	noise equivalent sigma zero
NIES	Non-Intrusive Exhaustive Search
OS	ordered statistic
PAL	Provincial Airlines Ltd
$P_d$	probability of detection
PERD	Program of Energy Research and Development
PES	parallel exhaustive search
$P_{fa}$	probability of false alarm
QD	Quadratic Discriminant
RAM	random access memory

SAR	synthetic aperture radar
SCW	Scan SAR Wide
SFS	sequential forward selection
SLAR	side-looking airborne radar
SLC	single look complex
$\sigma^0$	radar cross section
SR	slant range
VH	vertical send / horizontal receive polarization
VV	vertical send / vertical receive polarization

## **List of Appendices**

Appendix I	Sequential Forward Selection Algorithm
Appendix II	Exhaustive Search Algorithm
Appendix III	Exhaustive Ranked Search Algorithm
Appendix IV	Limited Exhaustive Search Algorithm
Appendix V	Parallel Exhaustive Search Algorithm
Appendix VI	Confusion Matrix Notation

# 1 Introduction

In the extremes of the northern and southern hemispheres, there are hazardous environmental conditions that threaten exposed manmade structures. In the North Atlantic Ocean, off the east coast of Newfoundland, Canada, is the Grand Banks. This area is rich in natural resources, such as oil reserves and fish stocks. Each spring, the final treks for the Greenland born icebergs follow the Labrador Current—a natural oceanic flow that follows the Labrador and Eastern Newfoundland coastline. Some icebergs that travel the Labrador Current make it as far south as the Grand Banks or even further. The combination of North Atlantic shipping lanes, oil platforms, oil platform support vessels, and fishing vessels cause a significant human presence in the Grand Banks region. To minimize the monetary and life risks associated with iceberg-infested waters, organizations such as the International Ice Patrol (IIP), the Canadian Ice Service (CIS) and Provincial Airlines Ltd (PAL) have taken an active role in iceberg management. This entails knowing where the icebergs are, predicting where they will drift and passing this information on to the public and private sector. Current operational iceberg reconnaissance from the IIP and PAL are collected with airborne forward-looking and side-looking airborne radar (FLAR and SLAR), which is supported by visual confirmation when weather conditions permit.

One alternative to aerial ocean surveillance is satellite remote sensing. Satellites offer a variety of sensor types, swath coverage, and resolutions. Synthetic aperture radar (SAR) is one type of sensor that is commercially available from earth's orbit. SAR is an active microwave sensor, where active implies that it emits its own energy and receives a portion of that energy back. The energy received is largely dependent on the send and receive wave polarizations and the interaction of the wave with the ground. The wave interaction with the ground is dependent on geometry and dielectric properties of the medium with which the wave interacts. SAR (unlike optical) is not dependent on sunlight, and thus can be acquired at day or night. Additionally, for the specific SAR frequencies used here, a minimal interaction is expected between the air and water

droplets that occur in the earth's atmosphere, hence SAR signals are capable of passing down and back through cloud, rain and fog. This is especially important when considering the maritime environment of the Grand Banks where these conditions are the norm.

### ***1.1 Purpose of Study***

The purpose of this research is to demonstrate the capabilities of SAR-based sensors for automated iceberg and ship surveillance. Automated SAR target identification is accomplished here by first using histogram methods for target detection and second by using target-based features for iceberg and ship classification. Additionally, since current and newly available spaceborne sensors have advanced polarization capabilities at various resolutions, the direct comparison for the probability of classification for single, multi, and quad polarization SAR is investigated.

Many works have shown that both iceberg and ship detection with SAR is possible using histogram processing methods [1, 2, 3]. These works however do not specifically address the matter of classification for SAR iceberg and ship detected targets. This said, one SAR group from McMaster University [1] has applied pixel-based Bayesian classification methodologies to radar data for iceberg and sea ice classification [4, 5].

The approach for detection of iceberg and ship targets in this work follows a histogram methodology as presented by [3, 6]. The proposed approach for classifying detected iceberg and ship targets focuses on supervised Bayesian classification models with assumed multivariate Gaussian distributions and feature space optimization. Success for this approach is highly dependent on the known sample (or training data) representing the general population. Specifically, the number of samples and feature space distribution of the training data must represent the general population in order to build a reliable and robust model. Two forms of feature space optimization are evaluated. The first is a sequential search, sequential forward selection (SFS), which is computationally inexpensive. This is due to the relatively small proportion of the feature space being

evaluated. The second is the exhaustive search (ES). This search method can be extremely computationally expensive due to the evaluation of all possible combinations of the feature set. Two variants of the ES are developed and implemented here based on a limited and ranked exhaustive feature space search.

In addition to target detection and supervised classification, other works have also shown advances in SAR technology that have increased the ability over standard single channel sensors for differentiating specific target backscatter. Specifically, polarimetric aerial SAR sensors have been tested and several unsupervised pixel-based classification methods have been proposed [7, 8, 9, 10, 11]. These methods are physically modeled after specific SAR backscatter from primitive geometric shapes or primitive scatter classes. Physical constraints based on geometry, dielectric properties of the medium, and polarimetric measurement describe these primitives. It is important to note that these are not modeled specifically for iceberg or ship targets; however, if dominant scatter types differ between iceberg and ship targets, then these methods add potential for increased classification accuracy. Here, Cameron decomposition was tested using the EMISAR polarimetric data [7]. The author modified and further developed MATLAB source code provided by MacDonald Dettwiler and Associates (MDA) for this purpose.

## 2 Relevant Background

This background focuses on remote sensing fundamentals concerning iceberg and ship identification with SAR data. Included here is a summary of radar theory relevant to iceberg, ship and ocean response, image processing and pattern recognition. As well, reviews of technical papers are included which are particularly relevant to iceberg and ship detection and iceberg and sea ice classification in radar data.

### 2.1 Fundamentals of Radar

Radio detection and ranging (radar) was developed as a means of using radio waves to detect the presence of objects and to determine their range. The process entails transmitting short bursts of microwave energy in a direction of interest and recording the strength and origin of the echoes (reflections) received from objects [12]. The range or distance to an object is found by measuring the time it takes for the transmitted energy, which is traveling at the speed of light, to travel to the target and back [13]. From this, the distance measure, which is commonly referred to as range ( $R$ ), is given by

$$R = \frac{ct}{2} \quad (2.1)$$

where  $c$  is the speed of light and  $t$  is the time from pulse transmission to scatter reception. The factor of 2 is included since the echo has to make a return trip to the measured object and back to the sensor.

One of the most useful models for describing radar performance is the radar equation. The radar equation gives the received signal power  $P_r$  of the scattering from an object as

$$P_r = \frac{P_t G_t}{4\pi R^2} \times \frac{\sigma}{4\pi R^2} \times A_e. \quad (2.2)$$

The first factor is the power density at a distance  $R$  meters from the radar, where  $P_t$  is the power that is radiated from the antenna in watts,  $G_t$  is the antenna gain, and  $4\pi R^2$  accounts for the divergence of the electromagnetic waves as they radiate out from the antenna/object in a spherical pattern. The second term is the radar cross section,  $\sigma$ ,

which is also normalized with respect to electromagnetic divergence. The product of the first two terms represents the power per square meter returned to the radar.  $A_e$  is the effective aperture area—a factor that represents the portion of power that the antenna actually receives [13].

The radars considered here are all monostatic. This means they transmit and receive from the same antenna. For monostatic sensors, the effective aperture area ( $A_e$ ) and the antenna gain ( $G_t$ ) are related by

$$A_e = \frac{G_t \lambda^2}{4\pi}, \quad (2.3)$$

where  $\lambda$  is the wavelength of the radar electromagnetic energy. By directly substituting Equation 2.3 into 2.2, we get

$$\sigma = \frac{P_r (4\pi)^3 R^4}{P_t G_t^2 \lambda^2}. \quad (2.4)$$

The radar cross section ( $\sigma$ ) is the intensity of the energy scattered back from the object to the source of the transmitted wave. It is equivalent to consider  $\sigma$  as the projected area ( $m^2$ ) of a variably sized perfectly conducting sphere that, if substituted for the object, would scatter identically the same power back to the radar [14]. The radar cross section is normalized with respect to radar resolution by taking the fraction of  $\sigma$  to the area of the image sample spacing ( $m^2$ ). Thus, normalized radar cross section ( $\sigma^0$ ) is a unitless ratio of area for a perfectly conducting sphere to the area of the image sample spacing [13].

### 2.1.1 Synthetic Aperture Radar

An airborne or spaceborne radar sensor can have a side, forward, or moving antenna for sending and receiving microwave energy. This study includes only side-looking radar technology for both aerial and satellite sensors. For instance, a side-looking radar flying in the azimuth direction transmits and receives microwaves in the range (orthogonal to azimuth) direction.

A consequence of using side-looking radar technology is that a varying look direction or incidence angle is collected. Formally, the incidence angle is a measure of the angle between the radar wave and the altitude normal. As can be seen in Figure 2.1, the first range data sample is collected at a steep incidence angle (towards normal) while the last range data sample is collected at a shallow incidence angle (away from normal). This incidence angle variation is important to consider as both target and ocean clutter radar signature (backscatter) can vary as functions of incidence angles.

The resolution of radar is not trivial due to the differing process of collecting data in the range and azimuth directions. The ground range resolution of a radar image can be found directly from the slant range resolution. The slant range resolution is defined as the distance it takes for emitted energy to travel half a pulse length. This is also the minimum distance required to detect point targets separately. Based on the definition of range in Equation 2.1, we can formulate the ground range resolution through trigonometry as

$$R_r = \frac{c\tau}{2 \sin \theta} \quad (2.5)$$

where  $\tau$  is the pulse length and  $\theta$  is the incidence angle. It is important to note that range resolution is independent of altitude. As well, as the pulse length decreases the range resolution becomes finer. However, pulse length is inversely proportional to system bandwidth and amplitude requirements for detection. Most radar systems today use chirp radar that allows for a small pulse length while maintaining the required bandwidth and amplitude.

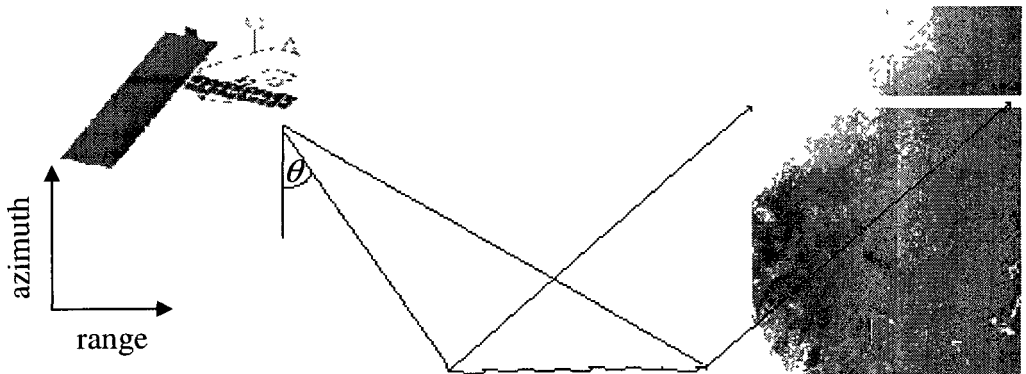


**Figure 2.1:** Side-looking radar and variable incidence angle

Resolution in the along track (azimuth) dimension for a traditional (real-aperture) radar is defined by

$$R_A = \frac{R\lambda}{L_a}, \quad (2.6)$$

where  $R$  is the slant range distance,  $\lambda$  is the wavelength of the transmitted energy, and  $L_a$  is the antenna length [15]. From Equation 2.6, by increasing the antenna length the azimuth resolution will become finer.

The breakthrough in radar technology came with the realization of synthetic aperture radar (SAR), discovered by Wiley in 1965 [15]. It was observed that two point targets at slightly different angles with respect to the track of the moving radar have different speeds relative to the radar platform. From this, the radar pulse when reflected from the two targets will have two distinct Doppler frequency shifts. Using the Doppler shifts and the flight path of the sensor a longer antenna can be synthesized from a physically shorter one. It has been shown that for SAR, the azimuth resolution is

$$R_A = \frac{L_a}{2}, \quad (2.7)$$

which shows that resolution becomes finer for smaller antennas [15]. This was originally seen as counter-intuitive because it is the opposite of real aperture systems. There are lower bound limiting factors for this equation to be valid however, where transmitting at least one plus each time the radar platform travels a distance equal to one half an antenna length is required [15].

### 2.1.2 SAR Ocean Backscatter

SAR interaction with the ocean surface is highly complex. Here we must consider that the dynamics of the sea surface are affected by wind, sea currents, swells, atmospheric effects and sea surface temperature. This is in addition to the microwave interaction with the water surface, which is affected by the dielectric properties of salt water, wave geometry and the continuously oscillating wave surface, the sensor frequency, sensor polarization and the local incidence angle. However, generally an oceanic radar return is

strongly correlated with local surface roughness. This surface roughness is in turn highly correlated with wind-generated capillary waves. Thus wind is typically a strong factor when considering ocean backscatter. In addition to wind, gravity waves and currents modulate the capillary waves on the sea surface to produce characteristic patterns in the SAR imagery [14]. This leads to a two tier scattering model, which is dependent on the small capillary waves and larger gravity waves that interact with the emitted microwave. The capillary waves are on the order of the length of the emitted sensor wavelength, where C-band is 5.5 cm and capillary waves are  $7 \pm 1$  cm [14]. SAR microwaves do not penetrate beyond a few millimeters of the ocean surface.

In the absence of wind, the ocean surface will be smooth and hence specular, reflecting the radar energy away from the sensor. Increasing wind speed will result in increasing ocean roughness and hence increased backscatter as more energy is returned to the sensor. It is important to note however that sensor constraints exist such as the noise equivalent sigma zero (NESZ)—which is a random white Gaussian noise—can overwhelm ocean backscatter for low wind speeds collected at shallow incidence angles [14]. Presented in Figure 2.2, the ocean backscatter is demonstrated to be dependent on wind speed, direction, SAR polarization and incidence angle [2]. It is clear from this figure that  $\sigma^0$  increases as a function of wind speed but decreases as a function of incidence angle. It is also apparent that the  $\sigma^0$  C-band VV polarization is greater than HH for all wind speeds, directions, and incidence angles. Additionally, the HH  $\sigma^0$ 's for winds blowing in the direction of the radar sensor ( $\phi = 0$ ) are shown to be larger than cross winds ( $\phi = 90^\circ$ ).

### **2.1.2.1 Processing Ocean Backscatter for Target Detection using CFAR**

Generally, targets on the oceans surface can be detected by radar when the ocean background contrasts with the targets of interest. Thus, if we consider a histogram of an ocean backscatter region (Figure 2.3), the ocean response will form a single modal distribution and any targets that are visually discernable (based on intensity) will appear in the upper or lower tail boundary of the histogram. In this work, we are only interested

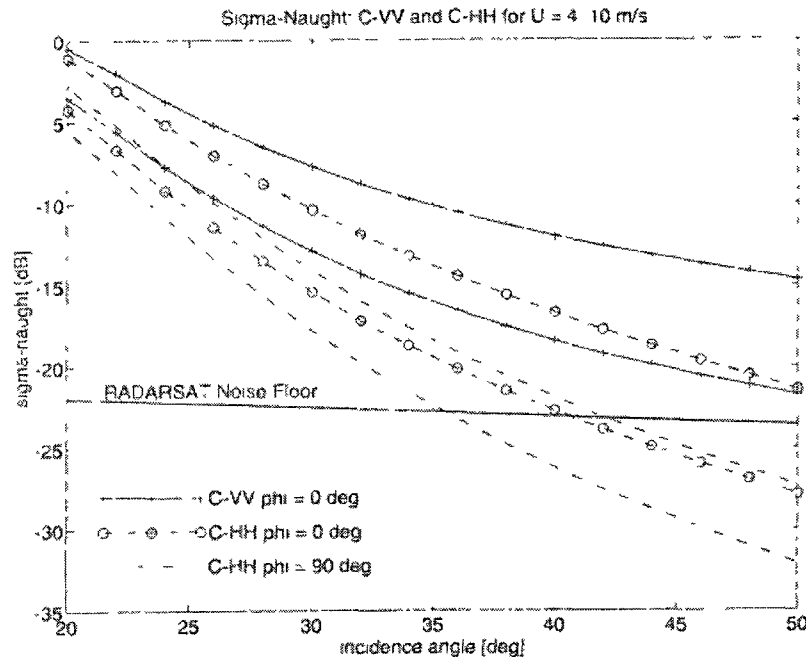


**Figure 2.2:** Ocean Backscatter  $\sigma^0$  for C-band VV and HH polarization [2]

in targets that have strong scattering properties that appear brighter than the ocean background. Target identification can then be maximized by selecting image modes that produce the greatest signal to clutter ratio (the ratio of target backscatter to ocean backscatter).

SAR sensors offer many different data forms or modes to choose from. These modes have varying image size, resolution, NESZ's and polarizations. Image modes with high resolution and low NESZ offer an improved signal to clutter ratio. Also, imagery with varying incidence angles and polarizations have to be considered collectively. It is true that the ocean backscatter decreases as a function of increased incidence angle. However, the backscatter of the targets of interest may also decrease as a function of increased incidence angle. It is also vital to consider polarization where it is known that VV will produce the greatest response from ocean, then HH, and then HV. The HV ocean backscatter response is considerably lower than HH or VV and is susceptible to being buried in the NESZ depending on mode and sensor. However, the type of targets of

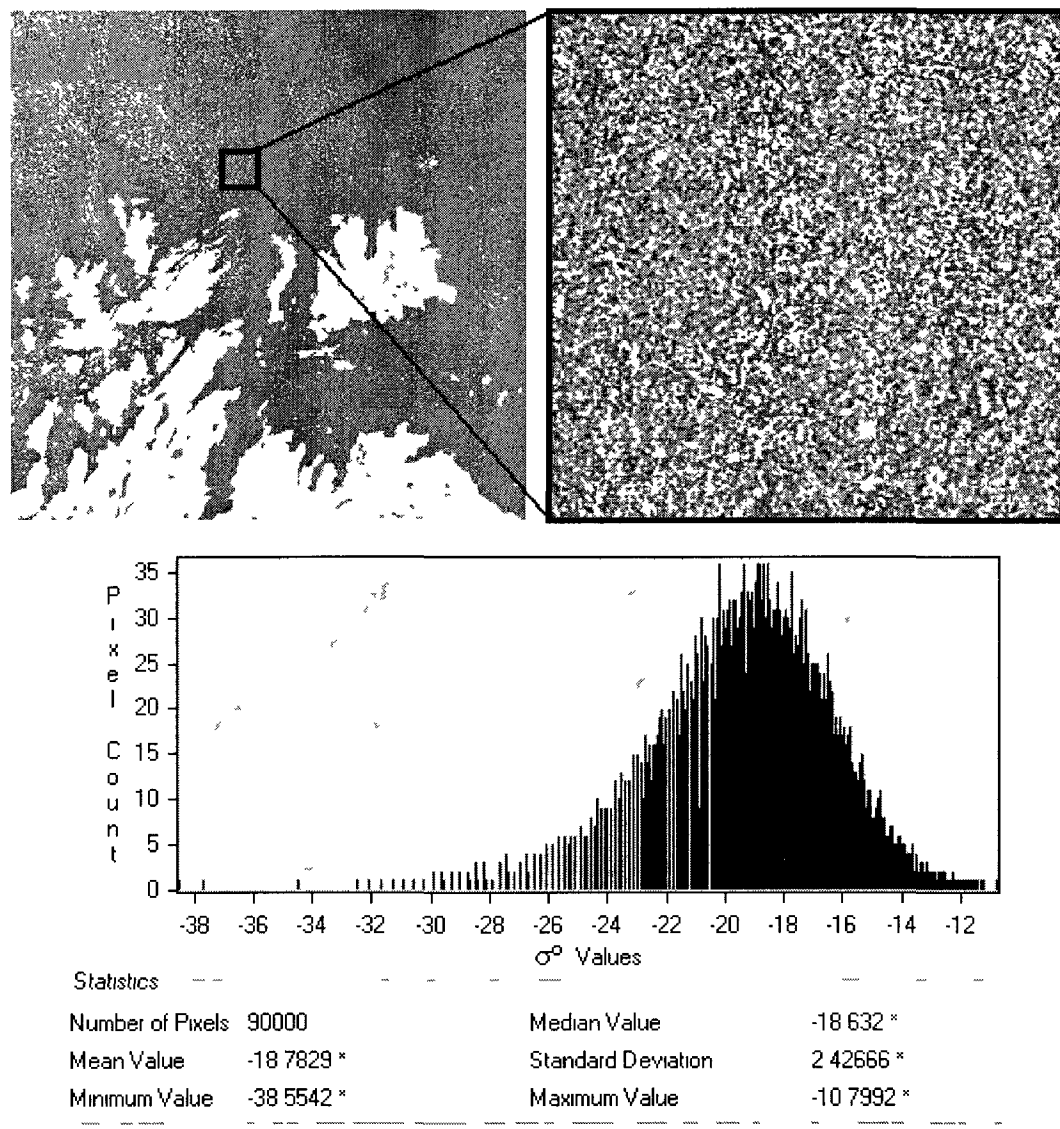


**Figure 2.3:** ENVISAT ASAR histogram of ocean clutter in HH  $\sigma^0$

interest will also backscatter differently based on polarization. Thus, in order to optimize SAR mode selection, resolution, incidence angle, NESZ and polarization have to be considered together.

It is desired to maximize the probability of detection  $P_d$  and minimize the probability of false alarms  $P_{fa}$  for iceberg and ship detection on an ocean background. Manual interpretation of SAR data in this way can be labor intensive, subjective, and error prone.

Thus, developing an automated algorithm for target detection which standardizes and benchmarks the technology capabilities ( $P_d$  and  $P_{fa}$  trade-offs) is desired. Considering that both the ocean and target backscattering mechanisms are variable and complex systems, it is unlikely that target detection will be modeled in an optimal way. From this, there will always be a trade-off effect where a higher detection rate is desired and potentially achievable but at the expense of an increased false alarm rate.

Monitoring the ocean with SAR has several issues that must be addressed. As described in the previous section, there are incidence angle and wind dependencies that significantly effect local SAR ocean response. From this, the statistics of ocean clutter can vary significantly over the coverage area of the radar. Attempting to set a fixed decision threshold will result in a similarly wide varying  $P_{fa}$  [1]. As can be seen in Figure 2.4, one SAR scene with a wide coverage area (approximately 500 km<sup>2</sup> in this case) can have several distinguishable problematic phenomena such as land, sea ice, atmospheric effects, nadir ambiguities, and significant incidence angle variation. Applying a global threshold for detection to this data would be at the expense of a paired lesser detection rate and/or an increased false alarm rate. As a consequence, using an adaptive threshold to determine the decision criteria based on local conditions would be beneficial. One such method is a constant false alarm rate (CFAR), which is one specific form of adaptive image processing.

It is known that when estimating statistical parameters that describe the ocean background, a large number of independent samples are required. However, local variation in ocean backscatter can significantly affect the expected single modal distribution. As a side, it is also important to process an image efficiently in software, thus, scanning an image and storing background clutter in a multi-pass way should be avoided if possible due to computational constraints. The accepted standard [1, 2, 3] is a CFAR sliding window approach, where a processing window is imposed over the image, the ocean response is extracted in the form of mean, standard deviation, and distribution shape and finally an adaptive threshold is run based on the ocean response. This CFAR

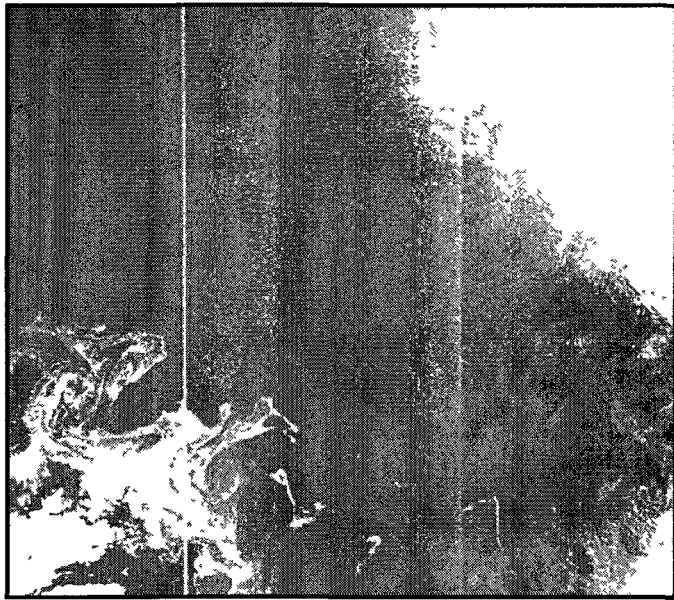


**Figure 2.4:** RADARSAT-1 SCW with variable ocean features

has to take into account the possibility of targets that are on the boundary of the processing window and thus truncated. This can be achieved by having a window overlap that is larger than the expected maximum target size. This way a potentially truncated target will be captured in its entirety in at least one processing window.

### 2.1.3 Physical Properties of Iceberg Backscatter

Glacial ice, unlike sea ice, has its origins on land. Glaciers form where precipitation in the form of snow exceeds evaporation and over time the snow compresses to become ice. Under the pressure of their own weight, glaciers flow from higher altitude to sea level. The ocean and glacier interface or glacier tongue is constantly exposed to tides and sea level changes which inevitably causes large pieces of ice to calve. It is this process by which icebergs are born [16].

The radar backscatter from an iceberg arises from two mechanisms, specifically surface scattering and volume scattering. For glacial ice there is extensive penetration of the radar wave into the ice. The scattering mechanisms controlling the return of energy are driven by the surface and volume multiple scatter [17].

Volume scattering is due to the low absorption of the non-saline glacial ice, allowing considerable penetration of the radar energy into the iceberg. For RADARSAT-1 at a frequency of 5.3 GHz, the penetration depth for glacial ice has been cited to vary from 3 to 14 meters, depending on the specific ice properties [16]. The penetrated energy is scattered by dielectric discontinuities that are due to trapped air pockets. Surface scattering is dependent on the specific surface structure of individual icebergs, including variations due to any snow or water on the surface of the iceberg, which may also reduce or alter the signal penetration. The orientation of local surface roughness to the SAR antenna and vertical relief relative to other portions of the iceberg and the sea surface are also contributing factors in the total backscattered intensity.

In instances with high clutter and small icebergs relative to the resolution of the SAR, the response from an iceberg may be indistinguishable from the bright ocean backscatter or speckle [6]. As can be seen in Figure 2.5, the  $P_d$  rate (calculated using a CFAR of  $2.46 \times 10^{-5}$ ) for small icebergs is directly dependent on wind speed and incidence angle [18]. In general, for HH and VV SAR, as wind speed increases the probability of detection of icebergs decreases. As well, for HH and VV SAR, as incidence angle increases the probability of detection of icebergs increases. From this, HH and VV SAR modes of choice for iceberg detection should favor increased (shallower) incidence angles. Current spaceborn SAR sensors have relatively high NESZ considering the ocean response in the HV channel and as such the background observed in the cross channel when monitoring ocean environments can be contributed to the NESZ. Thus, modes offering improved NESZ for the cross channel will improve the signal to noise ratio for both iceberg and ship targets.

#### **2.1.4 Physical Properties of Ship Backscatter**

The radar backscatter from a metal ship predominately arises from surface scattering. This is based on the premise that a metal ship's reflectivity is absolute. From this, we

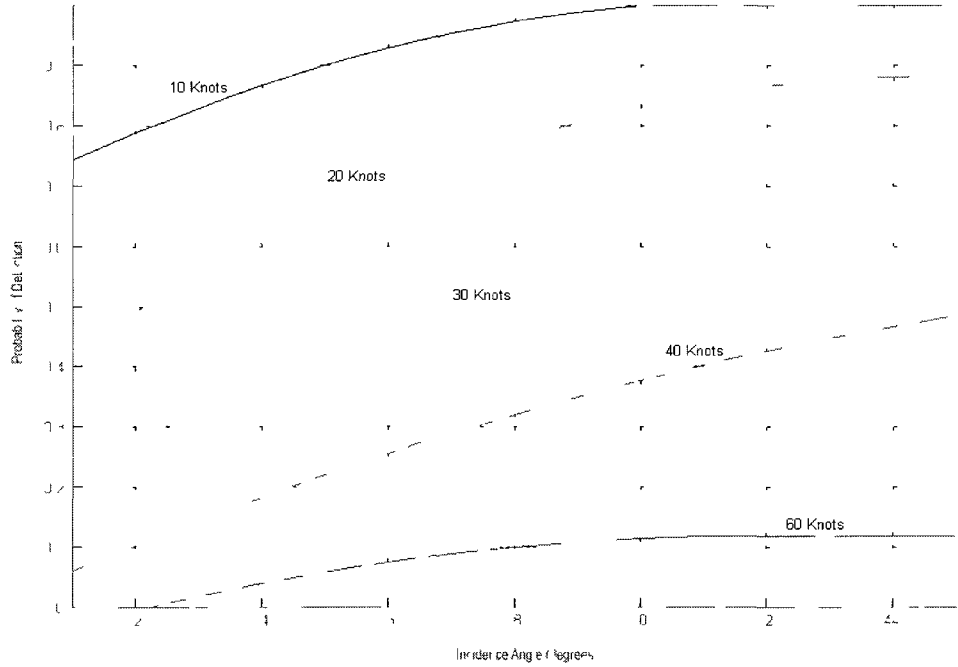


**Figure 2.5:** RADARSAT-1 Wide mode probability of detecting small icebergs [18].

expect that dominant scattering behavior would occur between the ships deck and superstructure and as well between the ocean and above-water portion of the ship hull itself. The strength of the return would depend on the orientation of the ship to the SAR sensor, structure and size of ship, and any deck equipment. Deck items for consideration include anchor, anchor chain, cylindrical tanks, storage boxes, and ballast stabilizers.

For describing ship scatter we considered dihedral, trihedral, and multi-bounce scatter as dominant. A dihedral (two bounce) response occurs when the transmitted radar wave is orthogonally aligned with a 90 degree pseudo-corner reflector. Predominant dihedral response would nominally occur from a ship superstructure and deck intersection when a ship's heading is toward, away, or parallel to the sensor direction of flight. There will also be a quasi-dihedral response from the ocean and the side of the vessel in calm sea states. A trihedral (three bounce) response would nominally occur when the send wave is aligned with a 90 degree horizontal  $x$ , 90 degree horizontal  $y$ , 90 degree vertical  $z$  degree

pseudo-corner reflector. Predominant trihedral response would nominally occur from the corners (acting pseudo-corner reflectors) between the ship superstructure and the deck interface. The trihedral response for a ship target is expected to be strongest when the heading is 45 degrees toward, away, or parallel to the sensor direction of flight. Multi-bounce scatter is expected from complex alignment with the deck equipment and the ship itself. Ship backscatter is a combination of dihedral, trihedral, and multi-bounce surface scatter where variables such as ship size, materials and orientation affect the significance of contribution of these elementary scattering phenomena.

It has been shown [13, 2] that empirical models for estimating ship size from the radar scatter have been successful. Vachon et al. [2] has presented a modified version of Skolnik's empirical radar cross-section as a function of ship length

$$\sigma = 0.08l^{7/3}, \quad (2.8)$$

where the units are such that  $\sigma$  is the radar cross-section of the ship in square meters and  $l$  is its length in meters.

In instances with high clutter (due to high wind speed), ship targets have been shown to have a decreasing detection rate based on ship size [2]. As can be seen in Figure 2.6, the minimum detectable ship length decreases as a function of increasing wind speed. Here the solid lines represent the upwind direction (i.e., the largest  $\sigma^0$ , hence, worst case) while the dotted lines represent the crosswind direction (i.e., the smallest  $\sigma^0$ , hence, best case).

From this, ship detection is directly dependent on ship size, wind speed, and wind direction. In addition, it is well known that ocean clutter is dependent on incidence angle. As seen in Figure 2.7, as the incidence angle increases the minimum detectable ship size also decreases. In general, as wind speed increases, the probability of detection for ships decrease. As well, as incidence angle increases, the probability of detection for ships increase. From this, the modes of choice for ship detection with SAR imagery are those with larger incidence angles.

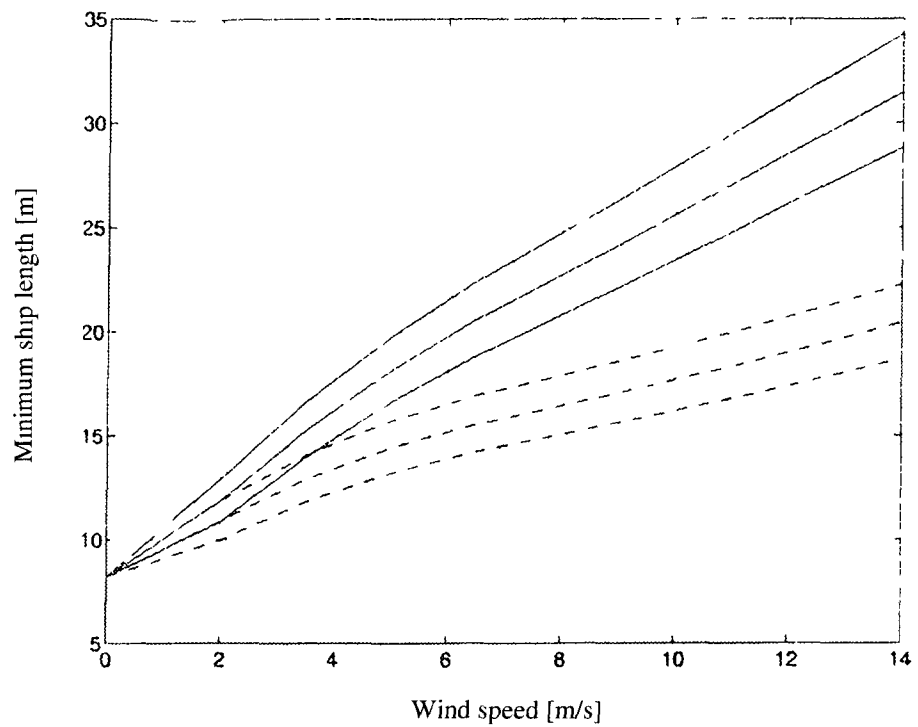


**Figure 2.6:** RADARSAT-1 S3 minimum detectible ship length [2].

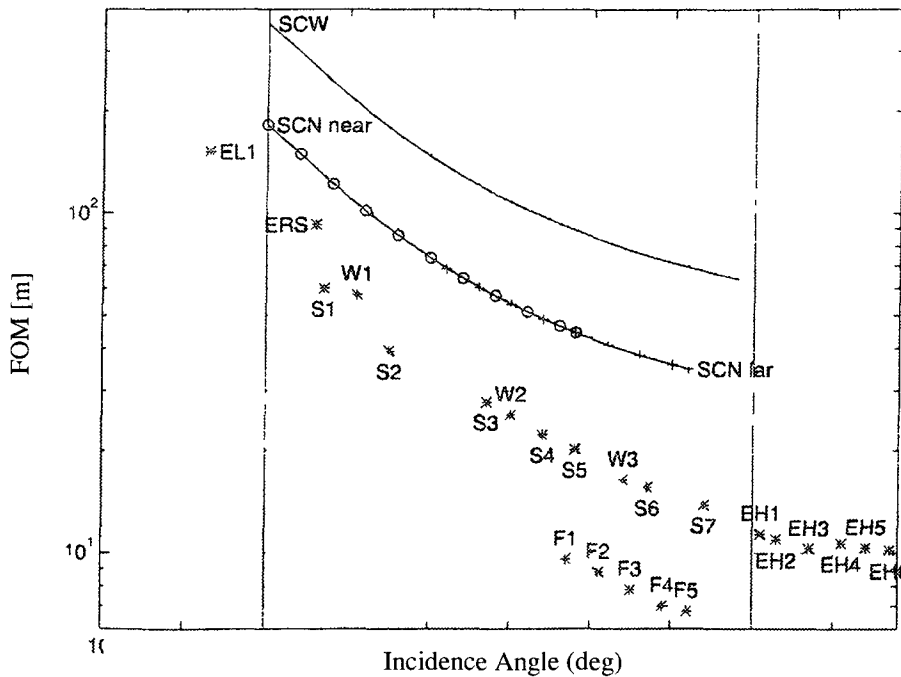


**Figure 2.7:** RADARSAT-1 Figure-of-merit for ship detection [2].

## **2.2 Digital Image Processing and Analysis**

An image can be defined as a two-dimensional function,  $f(x, y)$ , where  $x$  and  $y$  are spatial coordinates, and the amplitude of  $f$  at any pair of coordinates  $(x, y)$  is called the intensity or grey level of the image at that point [19]. When  $x$ ,  $y$  and  $f(x, y)$  are all finite and discrete quantities the image is considered to be a digital image. Digital image processing involves any modification or information extraction from an image with a computer.

When considering ocean target identification in SAR digital imagery, the key element of information extraction follows from target detection. The detection of targets in ocean SAR data as presented here is based on the expected  $K$ -distributed ocean clutter and the relatively strong response from ocean targets such as iceberg and ship backscatter.

### **2.2.1 Target Detection**

Image thresholding is a fundamental tool in image processing where objects of interest (or targets) can be identified in an autonomous process. Let  $f(x, y)$  be an image with a uniform background and also have targets of a different intensity than the background that are observable in the image. By setting a threshold,  $T$ , as an optimized boundary between the background and the target intensity, a binary image (or target mask) can be created.

Establishing a threshold can be accomplished by examining a histogram of the intensity of the image pixels. If the target of interest and the background form a bimodal distribution, a threshold  $T$  can be derived at the minimum point between the two maxima. Figure 2.8 shows an image clip of an EMISAR aerial SAR iceberg clip that has a relatively bright intensity compared to the ocean background. Considering the  $61 \times 61$  pixel region (outlined in red) containing both the iceberg and surrounding ocean response, the upper tail of the histogram is due to the target and the lower portion due to the ocean clutter. Therefore, as described above, by taking the minimum that is bounded by the two maxima we get good separation between the iceberg and the ocean background. If this

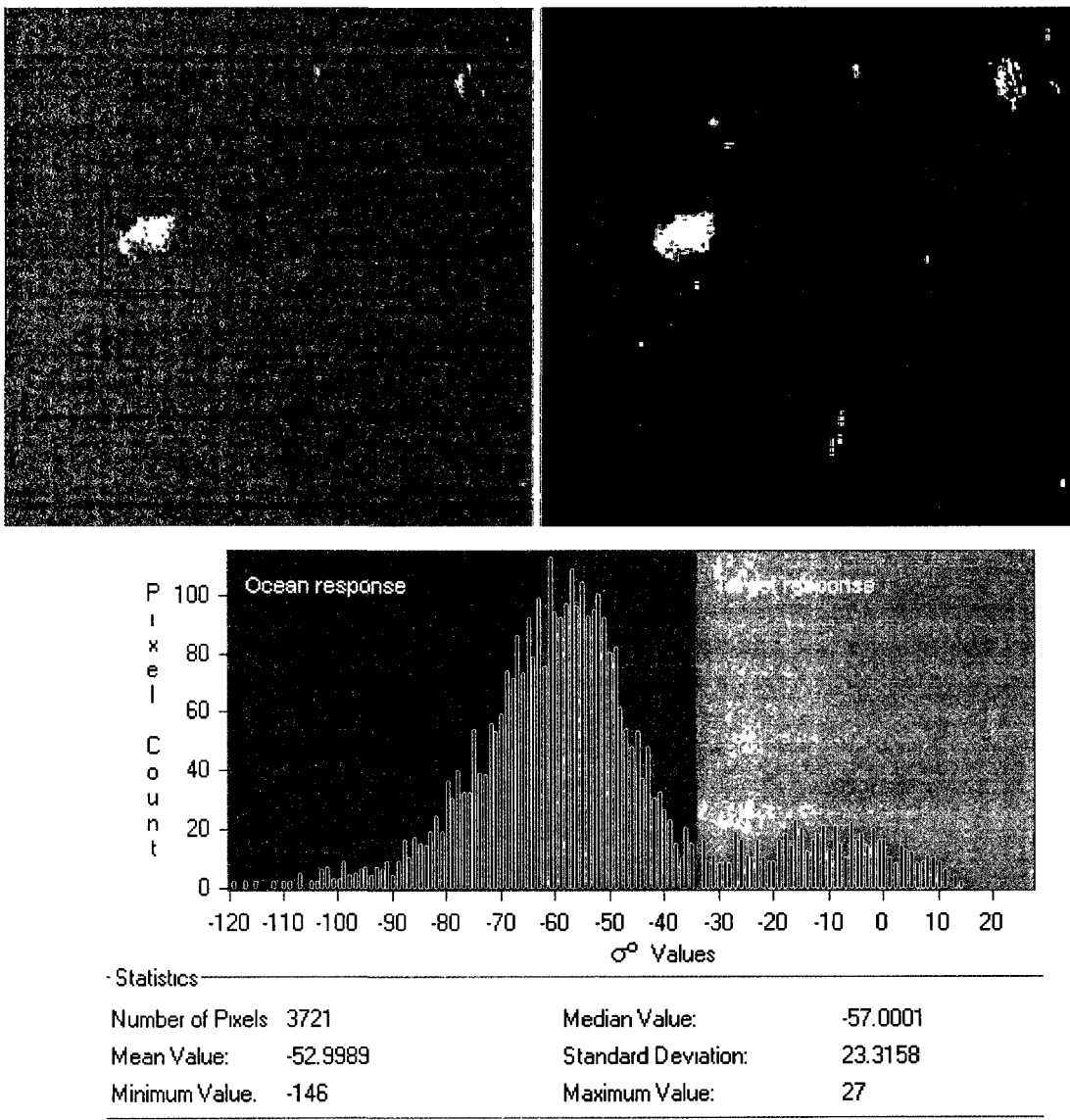


**Figure 2.8:** EMISAR sample iceberg detection via histogram local minima.

method is to be effective the processing window size must be target centered and allow for expected target sample size and ocean sample size to have comparable sample statistics.

Figure 2.9 demonstrates another way to achieve similar results by applying a threshold based on some combination of the mean and standard deviation for an area of interest

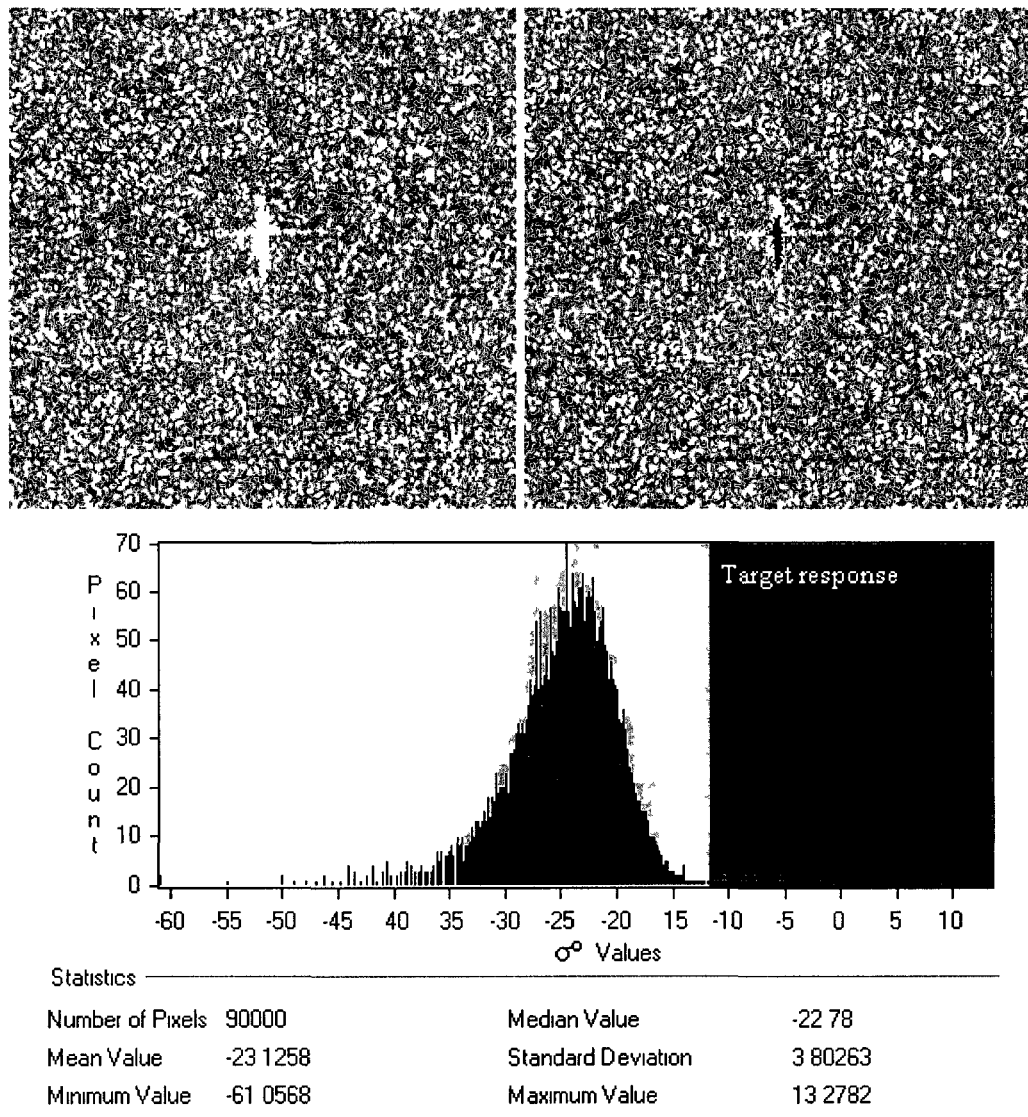


**Figure 2.9:** ENVISAT ASAR ship detection via adaptive threshold.

(AOI) clip or processing window. Since the background clutter for SAR has an expected distribution, and the targets (if present) are expected to be in the upper tail of the histogram, the assignment of the threshold can be derived based on an acceptable combination of target detection and ocean false alarm rates.

Just like in the previous example, the target samples appear in the upper tail of the histogram but due to the relative sample size difference in ocean backscatter versus target

backscatter pixels, there is no longer a visual decision boundary. Here, the threshold was set as three standard deviations from the mean for demonstration purposes.

Formally, the threshold process can be thought of as a functional test  $T$  of the form

$$T = T[x, y, p(x, y), f(x, y)] \quad (2.9)$$

where  $x$  and  $y$  are the column and row position in the image,  $f(x, y)$  is the image, and  $p(x, y)$  is some local property. Let the threshold image  $g(x, y)$  be defined as

$$g(x, y) = \begin{cases} 1, & f(x, y) > T \\ 0, & f(x, y) \leq T. \end{cases} \quad (2.10)$$

When  $T$  depends on  $f(x, y)$  alone it is considered a global threshold. If the threshold is based on  $f(x, y)$  and  $p(x, y)$  it is considered a local threshold. If  $x$ ,  $y$ ,  $f(x, y)$  and  $p(x, y)$  are considered, the threshold is called dynamic or adaptive [19].

### 2.2.2 Local/Adaptive Threshold and CFAR

Local threshold methods are useful when an image has uneven illumination [19]. As introduced in Section 2.1.2, this is the case in SAR ocean processing, where the background intensities decrease across an image due to an increasing incidence angle. As well, local atmospheric conditions can vary significantly. Also possible is the existence of sea ice or unmasked land that when mixed with the ocean background will not produce the expected  $K$ -distribution.

Local oceanic windowing methods are driven by a higher spatial probability of having a homogeneous background due to being collected in and exposed to similar conditions. It should also be noted that statistical histogram detection is driven by adequate sample statistics. Thus, window size is optimized by minimizing uneven image illumination and maximizing statistical stability. Once an adequate segmentation is achieved, the threshold methodology can be derived as described in Section 2.1.2.1.

The traditional approach for SAR target detection is through applying a CFAR algorithm. This method is based on a statistically expected sample of false alarm pixels or bright

ocean clutter that exists in the upper tail of the measured ocean SAR response. A threshold is set based on the acceptable and statistically expected number of false alarms pixels per image. For example, a CFAR rate of  $2.46 \times 10^{-5}$  will produce 612 individual false alarm pixels in a  $150 \text{ km} \times 150 \text{ km}$  RADARSAT-1 wide 3 image [18].

CFAR (Section 2.1.2.1) has a significant radar background and is considered here as one specific application of adaptive thresholding. As described, a sliding window sequentially covers the image such that the entire image is processed. There has to be some overlap in the windowing process to account for targets that could potentially exist on the windows edge. In processing a window or area of interest (AOI), the upper tail of the histogram can be truncated to avoid target contamination of the measured ocean clutter (otherwise known as setting guard cells or using an ordered statistic (OS)). The ocean statistics are measured and a threshold is adaptively set for that window based on the predetermined CFAR rate and the measured ocean distribution. For the resolution and number of looks in the data presented in this thesis, a  $K$ -distribution is expected.

### 2.2.3 Region Growing

Post target detection via the CFAR methodology, the entire target area (or region) identified may not be fully represented by the initial CFAR threshold layer. This is due to lower intensity target pixels that do not meet the initial (more aggressive) CFAR threshold. Region growing is a post processing technique to better identify the target boundary from background response.

Formally, region growing involves identifying neighboring pixels of seed pixels that have a high likelihood of being part of the target. Neighboring pixels (a pixel has 8 connected neighbors) of the seed pixels may be assigned to the target region based on some decision criteria that is more liberal than the initial threshold [19]. The process can be iterative; if identified neighboring pixels are assigned to the region they can be considered seeds in the next iteration. It is also possible to grow a region exclusively from the original seed with a lower threshold and/or a distance criterion. Whichever method is implemented, it

is important to consider and design a stop criterion such that potential region overgrowth is avoided.

Figure 2.10 shows an example of a region-grown ship target. Here initial seed pixels were set by thresholding 13 standard deviations from the background mean. The region growing algorithm is implemented with a difference equation, where each iteration neighboring pixels of seed pixels that are greater than 6 standard deviations from the background mean are assigned seed pixel status. This could be problematic if the background expectations (preconditions) are broken, as a loop bounded only by the processing window size is conceivable. The final region grown product is binary filled and morphological opened to create a clean target boundary.

Another similar approach which leads to acceptable results is to pass a ceiling threshold (primary) and a floor threshold (secondary) over the processing window. All objects that are detected in the ceiling threshold are assigned target status. Post detection from the ceiling threshold, the floor threshold is run for region growth and the intersecting target from the floor threshold is taken as the target. A criterion that protects region overgrowth can be implemented such that the ceiling and floor threshold objects have nominally aligning centers.

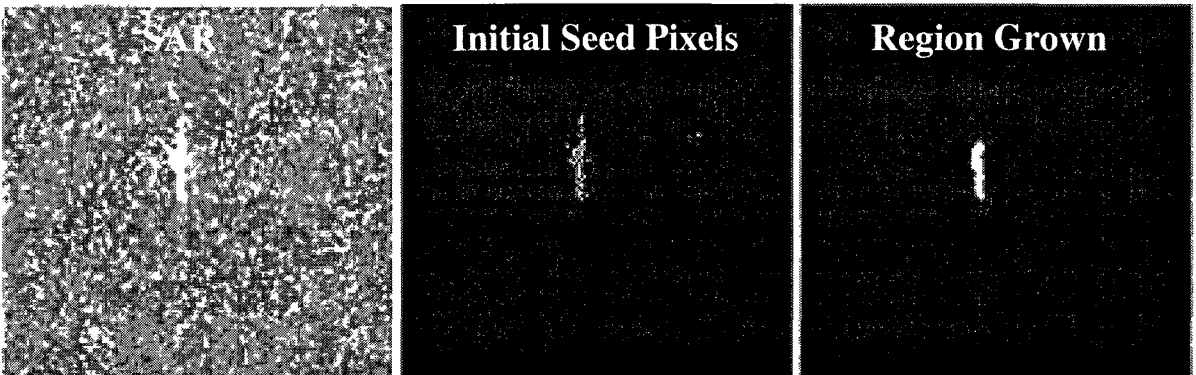


**Figure 2.10:** RADARSAT-1 ship target region growing example.

## **2.2.4 Feature Extraction**

Feature extraction is a processing step that follows once a target has been identified. Once a target has been detected (with region growing), the binary layer that describes the target can be used for feature extraction. Feature extraction allows for common shape features like area, major axis length, minor axis length, elongation, compactness, circularity, roughness and central moments to be collected for any given target. In addition, the intensity or normalized radar cross section ( $\sigma^0$ ) features like mean, maximum and variance are extracted by overlaying the binary target mask on the original SAR window.

The process of feature extraction was implemented here in an attempt to mimic the human visual interpretation process and to achieve significant data compression. Consider a human interpreter, the process of labeling or discriminating targets is often based on the collective experience of the interpreter and their ability of identify reoccurring tendencies for particular objects based on their shape, size and brightness. The second reason for feature extraction is data compression, the process allows for each target to be represented by a fixed set of features that are significantly easier to work with compared to the raw target imagery. Specific features were extracted with the aid of commercial image processing software packages such as MATLAB and HALCON. The process of selecting which features to be collected was based on previous experience and their availability from the aforementioned commercial image processing libraries.

## **2.3 Pattern Recognition**

Post processing of all identified targets involves a classification algorithm that assigns or labels a specific target to a class. Based on the unknown target's best fit to one of the  $n$  class models, a target classification can be assigned. There are a variety of different approaches for developing a class model. Here we will focus solely on supervised parametric models which are based on Bayesian decision theory.

### 2.3.1 Bayesian Decision Theory

Bayesian decision theory is a fundamental statistical approach when solving pattern recognition problems [20]. Bayes formula is

$$P(\omega_j | \mathbf{x}) = \frac{p(\mathbf{x} | \omega_j)P(\omega_j)}{p(\mathbf{x})}, \quad (2.11)$$

where  $p(\mathbf{x} | \omega_j)$  is the class conditional density function of class  $j$ ,  $P(\omega_j)$  is the prior probability for class  $j$ , and  $p(\mathbf{x})$  is a scale factor which normalizes the sum of the posterior probabilities  $P(\omega_j | \mathbf{x})$  to one. From this, the Bayes (minimum error) decision rule for a two class system can be written as

$$\text{if } P(\omega_1 | \mathbf{x}) > P(\omega_2 | \mathbf{x}) \text{ decide } \omega_1; \text{else } \omega_2. \quad (2.12)$$

Since  $p(\mathbf{x})$  is only a scale factor, it does not influence an unknown sample  $\mathbf{x}$  classification assignment, and thus we write the discriminant function (DF) as

$$f_i(\mathbf{x}) = p(\mathbf{x} | \omega_i)P(\omega_i). \quad (2.13)$$

This function is often modified by taking a monotonic transformation  $g_i(f_i(\mathbf{x}))$ , producing

$$g_i(\mathbf{x}) = \ln p(\mathbf{x} | \omega_i) + \ln P(\omega_i). \quad (2.14)$$

In doing so, all classification results will produce the same decision and at a reduced analytical and computational expense [20].

#### 2.3.1.1 Maximum Likelihood: a Quadratic Discriminant Function

The general multivariate normal density in  $n$  dimensions (feature space) is written as

$$p(\mathbf{x}) = \frac{1}{(2\pi)^{n/2} |\Sigma|^{1/2}} \exp\left[-\frac{1}{2} (\mathbf{x} - \boldsymbol{\mu})^T \Sigma^{-1} (\mathbf{x} - \boldsymbol{\mu})\right], \quad (2.15)$$

where  $\mathbf{x}$  is the sample column vector of length  $n$ ,  $\boldsymbol{\mu}$  is the mean sample column vector of length  $n$ ,  $\Sigma$  is the  $n \times n$  covariance matrix, and  $|\Sigma|$  and  $\Sigma^{-1}$  are its determinant and inverse, respectively. [20]

From the Bayesian classification presented in Equation 2.11, if we assume the class feature densities  $p(\mathbf{x} | \omega_i)$  are multivariate normal, then we can substitute Equation 2.15 into Equation 2.14, which gives,

$$g_i(\mathbf{x}) = \ln \left[ \frac{1}{(2\pi)^{n/2} |\Sigma|^{1/2}} \exp \left[ -\frac{1}{2} (\mathbf{x} - \boldsymbol{\mu})^T \Sigma^{-1} (\mathbf{x} - \boldsymbol{\mu}) \right] \right] + \ln P(\omega_i) \quad (2.16)$$

and from Equation 2.16 we get,

$$g_i(\mathbf{x}) = -\frac{1}{2} (\mathbf{x} - \boldsymbol{\mu})^T \Sigma^{-1} (\mathbf{x} - \boldsymbol{\mu}) - \frac{n}{2} \ln(2\pi) - \frac{1}{2} \ln |\Sigma| + \ln P(\omega_i). \quad (2.17)$$

The quadratic discriminant model  $g_i(x)$  for each class is built by estimating the population mean ( $\boldsymbol{\mu}$ ) and covariance ( $\Sigma$ ) from the known training data. This way, online classification of an unknown sample can be evaluated for distance from each  $g_i(x)$ . The class function which produces the maximum scalar value (minimum distance from class) is the class assignment for the unknown sample.

### 2.3.2 Feature Selection

One of the fundamental problems in statistical pattern recognition is to determine which features should be employed for the best classification results [21]. Feature selection can be defined as follows: given a set of candidate features, select a subset that performs the best under a classification system [22].

Feature selection algorithms can not only reduce the cost of running a classification algorithm by reducing the feature space, but can also provide a better classification model due to the statistically favored feature space that better fits the pattern recognition problem [23].

The feature selection algorithms presented in this thesis follow a wrapper approach when considering feature subset evaluation [24]. This means that the actual classifier discriminate function and the measured accuracy or error rate is directly used for comparing feature subsets. Aha and Bankert [25] suggest that the wrapper approach outperforms other indirect evaluation methods however at the cost of increased

computational effort. This is in agreement with Inza's work which suggests that for small data sets a wrapper approach is the method of choice [26].

### 2.3.2.1 Sequential Forward Selection

The sequential forward selection (SFS) algorithm [25, 26, 27] is a search method that starts with an empty “selected” feature set and iteratively evaluates and adds features in a forward manner from the available “test” feature set to the “selected” set. Once a feature has been identified to offer the most improved accuracy for the dimensionality (or feature space) being evaluated, it is permanently assigned as a member of the selected feature set and as well removed from the test feature set. Appendix I outlines pseudo code for the SFS algorithm. The SFS algorithm is  $O(n^2)$ , where  $n$  represents the number of features for the target feature space, and can be deduced from the number of iterations required by SFS as presented in Equation 2.18.

$$\sum_{k=1}^n k = \frac{n(n+1)}{2} \quad (2.18)$$

Some SFS algorithms stop once an increase in performance is not achieved [27]. However, the implementation employed in this thesis adds all available features based on a maximum gain / minimum loss strategy.

Other variants of this search strategy, such as sequential backward selection (SBS), are also viable methods [25]. SBS is very similar to the SFS algorithm with the exception that the data set starts full and removes features based on least additive effect. This algorithm is noted as (nominally) being more computationally expensive than the SFS algorithm even though the order and number of evaluations are the same. This is due to the SBS having to evaluate the bulk of the search in the higher order feature spaces where the discriminate function training and evaluation are more computationally expensive [22].

### 2.3.2.2 Exhaustive Search

The exhaustive search (ES) is the only algorithm that is guaranteed to find the optimal feature combination [28]. The cost of finding the optimal solution is tied to the extensive

computational effort to evaluate all  $2^n$  permutations,  $O(2^n)$ , where the exponent  $n$  represents the number of features that describe the target feature space. Generally, the ES is not utilized as a feature selection algorithm due to its exponential computational expense. This problem is even further amplified when considering more computationally expensive discrimination functions, larger feature spaces and larger sample sizes. Liu and Motoda propose two approaches to ES, the depth-first and breadth-first [29]. The depth first approach evaluates down (a tree structure) all combinations that contain a particular feature. For example, a 3 feature space would be evaluated, FS {1}, FS {1, 2}, FS {1, 3} FS {1, 2, 3}, FS {2}, FS {2, 3}, FS {3}. The breadth-first approach evaluates across all combinations of a feature space, and then expands its search space. For example, a 3 feature space would be evaluated, FS{1}, FS{2}, FS{3}, FS{1, 2}, FS{1, 3}, FS{2, 3}, FS{1, 2, 3}. Regardless of approach, both evaluate all possible combinations.

The implementation of ES presented in this thesis follows the breadth-first approach. The breath-first approach was adopted because it searches the lower feature spaces first. If doing a partial ES, focusing the search in lower feature spaces is advantageous since it minimizes the curse of dimensionality. This is especially important when approximating the maximum likelihood inverse covariance matrices since they will become singular when  $n$  or less samples are used to estimate  $n$  or more feature spaces [30]. Hence, this problem is avoided by stopping the search before the  $n^{\text{th}}$  feature space is evaluated in the breath-first implementation. Appendix II outlines pseudo code for the ES algorithm and the **incrementFS** function.

The MATLAB **incrementFS** function was designed by the author with code flexibility in mind, allowing data distribution to different processors (parallel processing on the data level) with unique start and stop combinations. Parallelization of the ES (PES) method described above leads to a linear speed-up as a function of the number of processors used. The overhead of assigning work to computers, managing message passing, and integrating results is negligible compared to the computational effort required for feature space evaluation. This said achieving a reasonable search time for larger search spaces

will eventually lead to unreasonable execution times due to the exponentially increasing computational cost of increasing feature spaces [28] combated by the linear decreasing computational cost of using more processors.

Two suboptimal variants of the ES were developed by the author for this thesis work: the exhaustive ranked search (ERS) and the limited exhaustive search (LES). The ERS work was inspired by exactly the reason why ES methods are often discredited: their exponential dependency on the number of features. Here it is proposed that as the number of features is reduced from the working training set, the ES will require exponentially less time to run. The LES is simply the ES with a time stop criteria as opposed to the evaluation of all combinations. The LES was inspired by the fact that the lower feature spaces can be evaluated exhaustively with reasonable computation times as the bulk of computational load exist in higher order feature spaces. As well, the LES supports limited data sets that would potentially suffer from the curse of dimensionality. The ERS, LES and PES algorithms are presented in Section 5.4 and 5.5.

### 2.3.3 Discriminant Performance

It is important to estimate the classifier performance for evaluation and prediction purposes. The three main methods for performance estimation are re-substitution, hold out, and cross-validation [21]. For re-substitution, all samples are used to train the classifier and to test its performance. The hold out method separates all samples into two groups, a training set and a test set. The cross-validation method iteratively divides all samples into two groups, a training set and a test set. For each iteration of cross-validation, a subset of data is extracted for training, and the remaining sample(s) are used for testing. The testing is such that each sample is tested only once during the entire process. The size of the testing subset can be as low as one sample. Cross-validation using one sample for testing is commonly known as the leave-one-out method [21].

The re-substitution method results in an optimistically biased estimate for performance and should only be used when the sample size is sufficiently large. The hold out method

is unbiased; however, all samples are not used in the training phase and as such the overall potential for classification and performance estimation could decrease. This is especially true for small sample size data. The cross-validation method is essentially an unbiased measure. However, recalculation of the classification model for each sample test creates a substantial computational effort compared to the hold out and re-substitution methods [21]. Given a small number of training samples and a relatively inexpensive DF, the cross-validation method is a reasonable compromise between potential evaluation bias and sample utilization. This process has been validated and described in Section 5.1.

## **2.4 Previous Works**

There has been a significant amount of study on automated target recognition in radar imagery. Of interest to this body of work are iceberg and ship target detection and discrimination. The following are a collection of significant journal and conference papers that have contributed to the direction of this work.

### **2.4.1 Marthaler's Iceberg and Ship Detection with SLAR**

In Marthaler and Heighway [31], the early development of an iceberg detection and classification capability was describe. This system for the US Coast Gurad used an aerial real aperture side-looking airborne radar (SLAR) system. The area of interest for iceberg and ship detection and classification was the Grand Banks of Newfoundland, Canada. The US Coast Guard through the International Ice Patrol (IIP) has been conducting iceberg reconnaissance in the North Atlantic since 1914. This reconnaissance was actually started in response to the sinking of the Titanic. The NASA Lewis research center in remote sensing was involved in this work in designing the hardware and software of the SLAR system. The goal of this work was to implement an automated way to detect and classify icebergs and ships. This work focused on a SLAR, X band (9.1 – 9.4 GHz), with a nominal resolution of 15 meters along track (ground) and 30 meters cross track (range).

A dynamic target threshold method was implemented for target detection. This was implemented during flight (real time), as average sea return was sampled to determine local threshold levels. This method is analogous to CFAR adaptive image histogram processing presented in Section 2.2.2, with the exception that a SAR image uses local sliding window statistics compared to sampling ocean response during flight.

Classification focused on the premise that, for targets of the same physical size, a ship will produce an echo of greater amplitude than that of an iceberg. This is theoretically based on the higher reflectivity of metal as compared with ice of glacial origin. The amount of energy returned from an object, its reflectivity  $R$ , can be expressed as

$$R = \left( \frac{n-1}{n+1} \right)^2 \quad (2.20)$$

where  $n$  is the index of refraction for the object. The value for the index of refraction of metal approaches infinity, thus the reflectivity of metal is 1. For ice of glacial origin, the index of refraction is approximately 1.79, giving a reflectivity of .08. The resulting ratio of reflectivity,  $(R_{metal}/R_{ice})$ , indicates that, theoretically, for targets of geometrically similar configuration, a ship would reflect 12.5 times (11dB) more energy than an iceberg. However, Marthaler and Heighway stressed that geometry and size varies significantly from iceberg to iceberg, and from ship to iceberg. As a result, the actual reflectivity differences between ships and icebergs can only be determined in a statistical sense from radar data collected for a large number of samples. The following key points were made:

- Ship and iceberg detection is successful using a dynamic threshold that is based on the average ocean background measured during flight.
- For targets of the same sizes, shape, and orientation to the SAR sensor, ship targets will theoretically reflect 11dB more energy than that of iceberg targets.
- Size, shape, and orientation vary significantly from iceberg to ship targets. Actual reflectivity differences between iceberg and ship targets can only be determined in a statistical sense from a large number of samples.

### **2.4.2 Vachon's Ship Detection with SAR**

The work of Vachon *et al.* on ship detection with SAR has been an ongoing effort for improved detection and operational evaluation [2, 32, 33]. The focus of this work has been on using the RADARSAT-1 C-band HH polarization SAR data. The study area for this work includes Canada's east and west coasts.

A statistical approach to ship target detection in a clutter background was used to show the performance capabilities of RADARSAT-1. Of specific importance were, (1) the optimization of a best fit distribution model for the ocean clutter, (2) the contribution effects from incidence angle, wind speed and wind direction on ocean clutter, and (3) the distinguishing of ship targets from the ocean background through a constant false alarm rate (CFAR) methodology.

Results suggest that a data-adaptive  $K$ -distribution produced an increased performance compared to assumed distribution methods. The proposed method measures the mean and standard deviation of a processing window and a parameter (called an order parameter) that defines the shape of the distribution. This way, the effect of variable winds and incidence angle on a local processing window are indirectly taken into account. Apparent strengths of this method are that the background is not assumed but modeled and in doing so removes potential variability when comparing unknown targets against the measured ocean background.

This method can be thought of as a specific form of adaptive image histogram processing presented in Section 2.2.2. Here, a statistically expected sample of false alarm pixels or bright ocean backscatter will exist in the upper tail of the known distribution of the measured SAR ocean response. A threshold is set based on an acceptable number of false alarm pixels per image being identified. Consequently, all targets that have backscatter greater than the accepted false alarm levels will be detected.

SAR ship backscatter has been reported as largely independent of incidence angle and environmental effects [34], whereas increased ocean response has been found to depend on decreasing incidence angle and increasing wind speed. The following key points were made:

- Ship detection performance improves for increased incidence angle due to the reduction in ocean clutter.
- Ship detection is best for fine beam modes due to their large incidence angle and high resolution.
- For larger incidence angles, the ship detection problem becomes the detection of bright point targets against a noise background.

#### **2.4.3 C-CORE’s Iceberg Detection with SAR**

Significant SAR iceberg research has come out of C-CORE [3, 6, 18, 50, 35, 36]. C-CORE is a research and development company that initially started out as the Centre for Cold Ocean Resources Engineering in 1975. C-CORE’s iceberg surveillance capabilities focus predominately on RADARSAT-1 (HH) and ENVISAT (HH and HH/HV) data in 8, 25, 50, 75, and 150-meter resolutions. The initial area of interest when doing validation studies for iceberg detection work was on Canada’s east coast, the Grand Banks of Newfoundland.

This work focused on an adaptive threshold detection method with an assumed  $K$ -distribution (see Section 2.2.2). Speckle noise (bright ocean response) was spatially filtered to remove potential false positive targets. Also, the target areas were morphologically closed (dilation followed by erosion) to smooth the target edges. This also had the added benefit of merging multiple pixel groupings that belonged to a unique target. The resulting target mask was then used to extract target characteristics required for the discrimination and classification process. Classification was initially proposed [3] based on the following three features: mean intensity, variance of intensity, and target area. Later works by this group describe a guard cell CFAR implementation, where the highest intensity pixels are excluded from the background intensity approximation via a

truncated sorted (or ordered) statistic. This ensures that the ocean clutter measure is representative of the sea clutter alone [6].

Iceberg radar backscatter arises from two mechanisms, specifically surface and volume scattering [17]. Volume scattering, which is dominant, is due to the low absorption of the non-saline glacial ice, allowing for considerable penetration of the radar energy into the iceberg volume. The penetration depth for glacial ice—at the frequency of 5.3 GHz—has been cited as 3 – 14 meters depending on the specific ice properties [16]. The penetrated energy is scattered by dielectric discontinuities (change in medium) that are caused by trapped air bubbles. Surface scattering depends on the surface structure of individual icebergs, including variations due to snow or water on the surface. The orientation of the local surface roughness, vertical relief relative to other portions of the iceberg and to the sea surface, are contributing factors in the total backscattered intensity [6]. The following key points were made:

- Iceberg and ship target mean, maximum, and variance features hold promise for classification.
- Iceberg detection performance improves for increased incidence angle due to the reduction in clutter level.
- The limits for iceberg target size detection are on the order of the SAR resolution.
- Iceberg backscatter is a complex combination of surface and volume scattering.

#### **2.4.4 Haykin’s Remote Sensing of Iceberg, Ship, and Sea Ice Targets**

Haykin *et al.* has contributed to remote sensing of icebergs, ships and sea ice through *Remote Sensing of Sea Ice and Icebergs* [17] and *Detection and Classification of Ice* [16]. He has also contributed to the topic significantly through conference and journal papers [1, 4, 5]. This review focuses on two areas of Haykin *et al.* work: the detection of radar ship targets, and the classification of iceberg and sea ice via statistically driven Bayesian methods.

#### **2.4.4.1 The Detection of Ship Targets by Ground Radar**

The work by Haykin *et al.* [1] on ship detection is well summarized in a report prepared for Transport Canada. The focus is on comparing Neural Network detection to the CFAR detection approach. Of interest to this body of work specifically is the conventional assumed Rayleigh,  $K$ -distribution, and ordered statistic (OS) CFAR approaches.

In low resolution radar (antenna beamwidth  $> 1^\circ$  and pulse length  $> 0.5 \mu\text{s}$ ) the sea clutter amplitude distribution has been shown to be Rayleigh. The Rayleigh distribution can be described by one parameter, as the standard deviation equals some constant times the mean. As the resolution of the radar increases, the statistics of sea clutter increasingly deviate from a Rayleigh distribution. This is a function of large sea clutter amplitudes leading to distributions with long upper “tails”, which can be accurately modeled as  $K$ -distribution [37]. The  $K$ -distribution of ocean clutter can be considered as being based on the underlying physics of the sea surface. It is a compound distribution, using a Rayleigh distribution to represent the small wind waves with short decorrelation times (fast changing relative to the SAR), but with the mean of the Rayleigh distribution changing with time according to gamma distribution, representing the effect of the larger swell waves, having longer decorrelation times (slow changing relative to the SAR). These longer-tail distributions are characterized by two parameters, one related to the mean and one related to the width. These are often termed scale and shape parameters [1].

Assuming that clutter is drawn from a  $K$ -distribution, a target detection threshold can be set to yield the desired probability of false alarms ( $P_{fa}$ ). This is accomplished dynamically for a processing window by thresholding  $\tau$  standard deviations from the mean. Here  $\tau$  is derived from the area under the probability density function that has been set as the accepted  $P_{fa}$ . This method will work as long as the clutter continues to match the assumed distribution. If the statistics change over time and location, the decision threshold, determined *a priori* based on the assumed distribution, will be incorrect [1].

The OS CFAR was designed to negate the effect of target pixels being included in the sampled ocean response. An OS CFAR generally collects data from a sliding window as in the adaptive threshold method, but the local sampling statistics are sorted in ascending order. Then a suitable percentile (empirically derived) of the sorted sampling statistic is culled. This way, as long as the percentile is significant enough to exclude multiple targets (based on expected maximum size and distribution), the remaining background sample will exclusively represent ocean clutter. Rather than try to model the clutter distribution specifically, the OS approach reduces variation found in the upper tail of the histogram, where the major factor determining  $P_{fa}$  actually exists [1]. The following key points were made:

- Ocean backscatter distribution is dependent on the resolution of the radar.
- The K-distribution physically models SAR ocean clutter.
- An OS CFAR can be useful for negating the effects of variable  $P_{fa}$ .

#### 2.4.4.2 Bayesian Classification of Icebergs and Sea Ice

Haykin *et al.* also contributed to work on iceberg and sea ice classification which focused on both single [4] and dual [5] polarized surface-based microwave radar. A Bayesian methodology for pixel-based classification of first year ice, multi year ice, icebergs, and iceberg shadow was investigated.

Initial work focused on single polarization (one feature space) reflectivity, which is known to depend on certain physical characteristics of ice type. The Bayesian classifier was trained on collected pixel samples to estimate distribution parameters for each class type. Both the Pearson system beta [38] and maximum likelihood Gaussian [39] distribution classifiers were investigated and the performance results were found to be essentially the same. This is of importance since the Gaussian classifiers have fewer parameters to estimate and are conceptually easier to work with. Later work expanded to included HH/VV (dual co polarization) and HH/HV (dual cross polarization) reflectivity. The use of dual polarization data for deriving a multivariate Bayesian maximum

likelihood classifier improved classification accuracy from 77% for HH to 82% for HH/HV reflectivity.

In approximating the performance of the classifier, the re-substitution method was employed (Section 2.3.3). Here, classification accuracy was calculated by finding the percentage of correctly classified ice type pixels of the total number of sample points.

It was concluded that sea ice in surface-based marine radar does exhibit considerable statistical variability. Hence, decision theory pattern recognition techniques to classify sea ice fields may be used. Non-parametric classification techniques and multilevel thresholding may not yield optimal classification results like Bayesian methods. The following key points were made:

- Maximum likelihood Gaussian distribution classifiers had essentially the same performance as more complicated Pearson system beta distributions.
- Dual polarized HH/HV radar showed improved Maximum likelihood classification for iceberg and sea ice over single polarized HH.
- Decision theory pattern recognition is demonstrated and found successful for iceberg and sea ice radar targets.

## **3 SAR Iceberg and Ship Target Detection**

This section presents the building of three distinct iceberg and ship target training data sets: single polarization HH RADARSAT-1 Wide, dual polarization ENVISAT AP, and quad polarization EMISAR. Here a summary for the sensors and the number of correlated detected targets is presented. Feature extraction for the RADARSAT-1 and ENVISAT AP iceberg and ship targets was collected using the iceberg detection software (IDS), which is proprietary software developed by C-CORE. The software uses the CFAR methodology as described in Section 2.2.2. For the EMISAR data set, due to the large image size (~12 Gigabytes for the Tango Denmark data set), resolution and data format, the author developed a CFAR methodology for target detection and routine feature extraction as described in Section 2.2.2.

### **3.1 Data**

Three data sources for ground truth (verified) SAR iceberg and ship targets have been collected. The RADARSAT-1 Wide 2 and 3 mode data were part of a research and development program that started in the late 1990's. The early goal of this work was to demonstrate the operational capabilities of SAR for iceberg and ship detection and discrimination. The dual polarization ENVISAT AP (HH/HV) mode data was part of a continuation study to quantify the potential benefits of using a dual channel SAR. This work started in 2002, and from the demonstrated benefits of dual channel SAR, this mode is the current sensor of choice. EMISAR, an airborne SAR, data has been used here to benchmark classification performance of iceberg and ships when using polarimetric sensors (HH/HV/VH/VV with phase). This is of importance since the soon to be launched RADARSAT-2 satellite will also have polarimetric modes and its classification capabilities are unknown.

#### **3.1.1 RADARSAT-1**

RADARSAT-1 is a Canadian Earth observation satellite developed to monitor environmental change and to support resource sustainability [40]. This platform was launch in 1995, and has outlived its original planned lifetime of five years as it is still

operational. RADARSAT-1 is an active SAR sensor. Thus, it is not dependent on daylight for data collection like other satellite-based optical sensors. As well, its HH C-Band microwave operational frequency of 5.3 GHz has minimal interference from clouds, haze, smoke, fog and rain.

RADARSAT-1 SAR offers an array of mode selections, with swath width ranges from 35 to 500 km and resolutions from 10 to 100 meters respectively. Through the various modes, incidence angle variations range from 20 to 50 degrees. Specifically of interest to this work are the 25 meter resolution Wide 2 and 3 mode data. Based on previous work [6], this mode is the best compromise between swath coverage and required resolution for iceberg and ship detection. This data has incidence angle range from 31 to 39 degrees for Wide 2 and from 39 to 45 degrees for Wide 3. All data have 12.5 meter pixel sampling in both azimuth and range, and an effective number of looks of 4 (one in range and four in azimuth). The NESZ in RADARSAT-1 is nominally -22 dB. [41]

### 3.1.2 ENVISAT

ENVISAT is an Earth observation satellite developed by the European Space Agency (ESA) to extend an already established observation program. ENVISAT is a multiple sensor platform. Of interest in this context is its advanced synthetic aperture radar (ASAR) sensor [42]. The platform was launched in 2002 and had a planned orbit lifetime of five years. Like RADARSAT-1's SAR, ENVISAT's on board ASAR has the advantages of being an active sensor in that it is not dependent on daylight for data collection like other satellite-based optical sensors. As well, its C-Band operational frequency of 5.3 GHz allows for minimal to non-existent interference from clouds, haze, smoke, fog and rain. Unlike the single polarization HH RADARSAT-1 sensor, ASAR has the added flexibility of choosing image modes in either HH or VV single polarization. Additionally, there are dual or alternating polarization modes offering HH/HV, VV/VH, or HH/VV combinations.

The ASAR sensor offers an array of mode selections where swath width ranges from 56 to 400 km and resolutions from 30 to 150 meters. Through the various modes, incidence angle variations range from 15 to 45 degrees [43]. Specifically of interest to this work is the nominal 30 meter resolution collected at IS 4 though 7. These have been selected based on optimization of incidence angle, swath coverage, required resolution, and polarization. This data has incidence angle range from 31 to 45 degrees. All AP data included in this study have 12.5 meter pixel sampling in both azimuth and range, and an effective number of looks of 1.8. The NESZ for ASAR ranges from worst case -19.4 to best case -27.0 dB for differing AP modes.

### **3.1.3 EMISAR**

EMISAR is an Earth observation twin engine jet platform that was developed by the Electromagnetics Institute (EMI) in Denmark. The EMISAR SAR sensor has been in a state of development since 1989, where it started out as a single polarization VV C-Band sensor and has since evolved into a C and L-Band polarimetric sensor. Like RADARSAT-1's and ENVISAT's SAR, EMISAR is an active sensor, thus, it is not dependent on daylight for data collection. As well, its C-Band operational frequency of 5.3 GHz allows for minimal interference from clouds, haze, smoke, fog and rain. Unlike the single polarization HH RADARSAT-1, or dual polarization (without phase) ASAR, EMISAR has the added capability of collecting quad polarization (HH, HV, VH and VV with phase) SAR data.

EMISAR offers an array of mode selections with swath width ranges from 12 to 48 km and resolutions of 2m with pixel spacing ranging from 1.5 to 6 meters respectively [44]. Incidence angle variations for the data sets used here range from 36 to 71 degrees. Specifically of interest to this work is the high 2 meter resolution. This is single look complex (SLC) data. The NESZ in EMISAR is nominally -40 dB.

### **3.2 Target Detection and Correlation**

As described in Section 2.2.2, a CFAR detection algorithm developed by C-CORE has been used for identification of iceberg and ship targets. Here the results of using the CFAR algorithm for iceberg and ship detection are presented for the three sensors. Data correlation was achieved by overlaying ground truth flight and target spatial information on the SAR data using geographic information system (GIS) software. This process was manually completed through visual interpretation.

#### **3.2.1 RADARSAT-1**

Seven images were acquired through a collaborative initiative investigating RADARSAT-1 Wide 2 and 3 modes in 2000 and 2001. Figure 3.1 shows an overview map of the images acquired that contain targets that have a valid correlation with ground truth. Figure 3.2 shows ground truth photographs (courtesy of Denny Christian, C-CORE), RADARSAT-1 Wide 3 iceberg targets and their associated CFAR target detected mask. Figure 3.3 shows RADARSAT-1 Wide 3 ship targets and their associated CFAR target detected mask. Ground truth for the ship targets and the Hibernia oil platform was provided by Provincial Airlines Limited (PAL). Table 3.1 is an image summary, where 27 correlated iceberg targets and 16 correlated ship targets make up the verified data set.

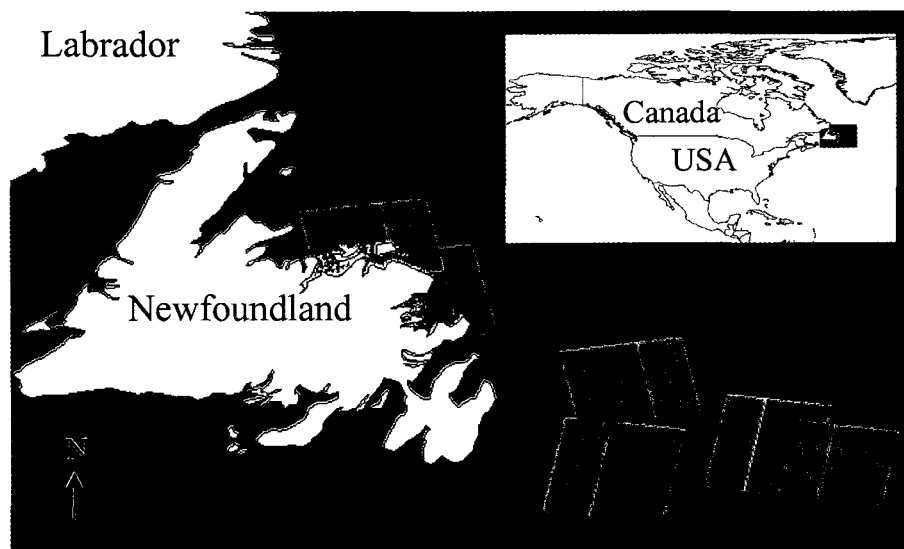


**Figure 3.1:** RADARASTA-1 imagery overview.

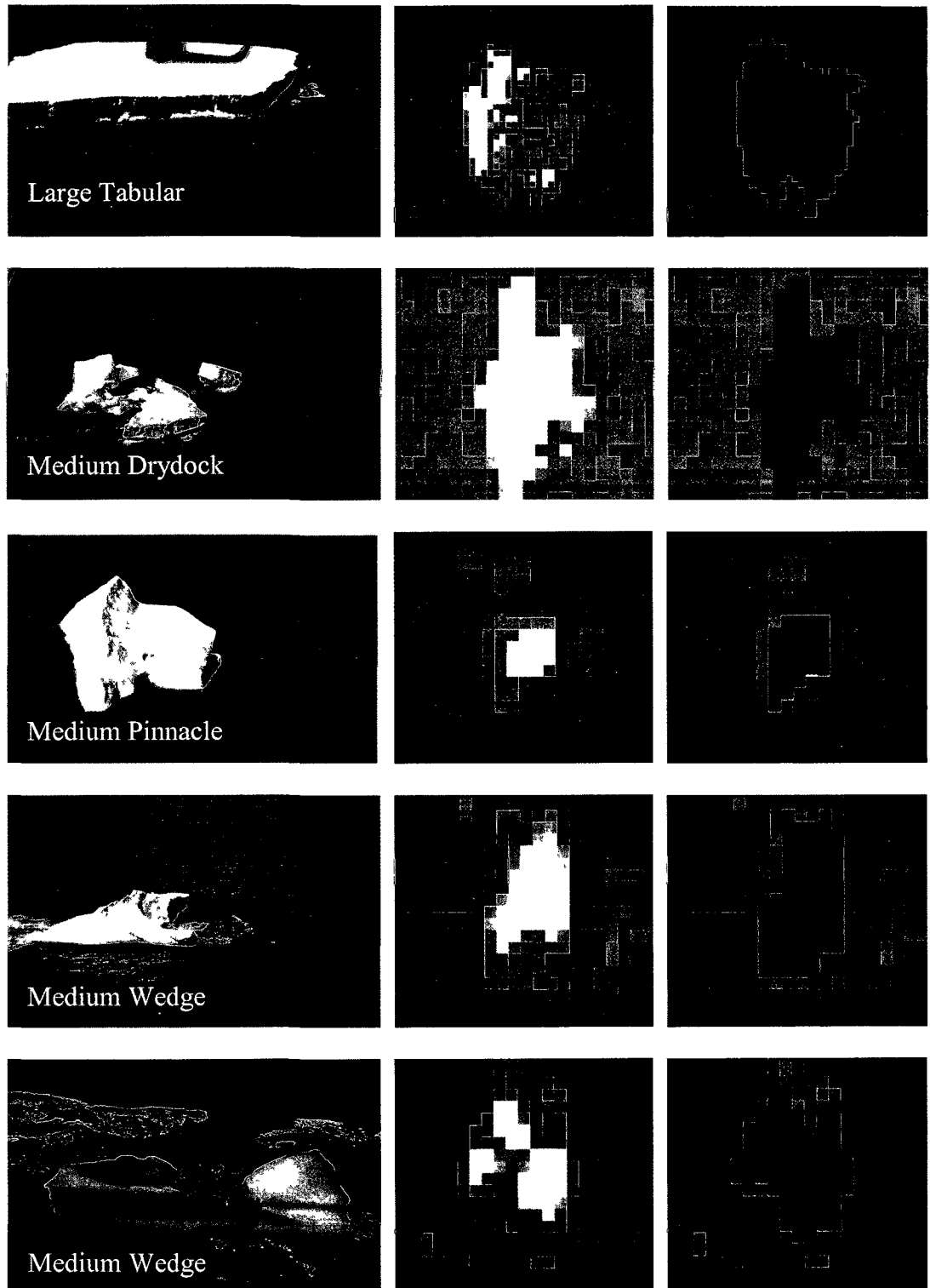


**Figure 3.2:** RADARSAT-1 W3 icebergs.

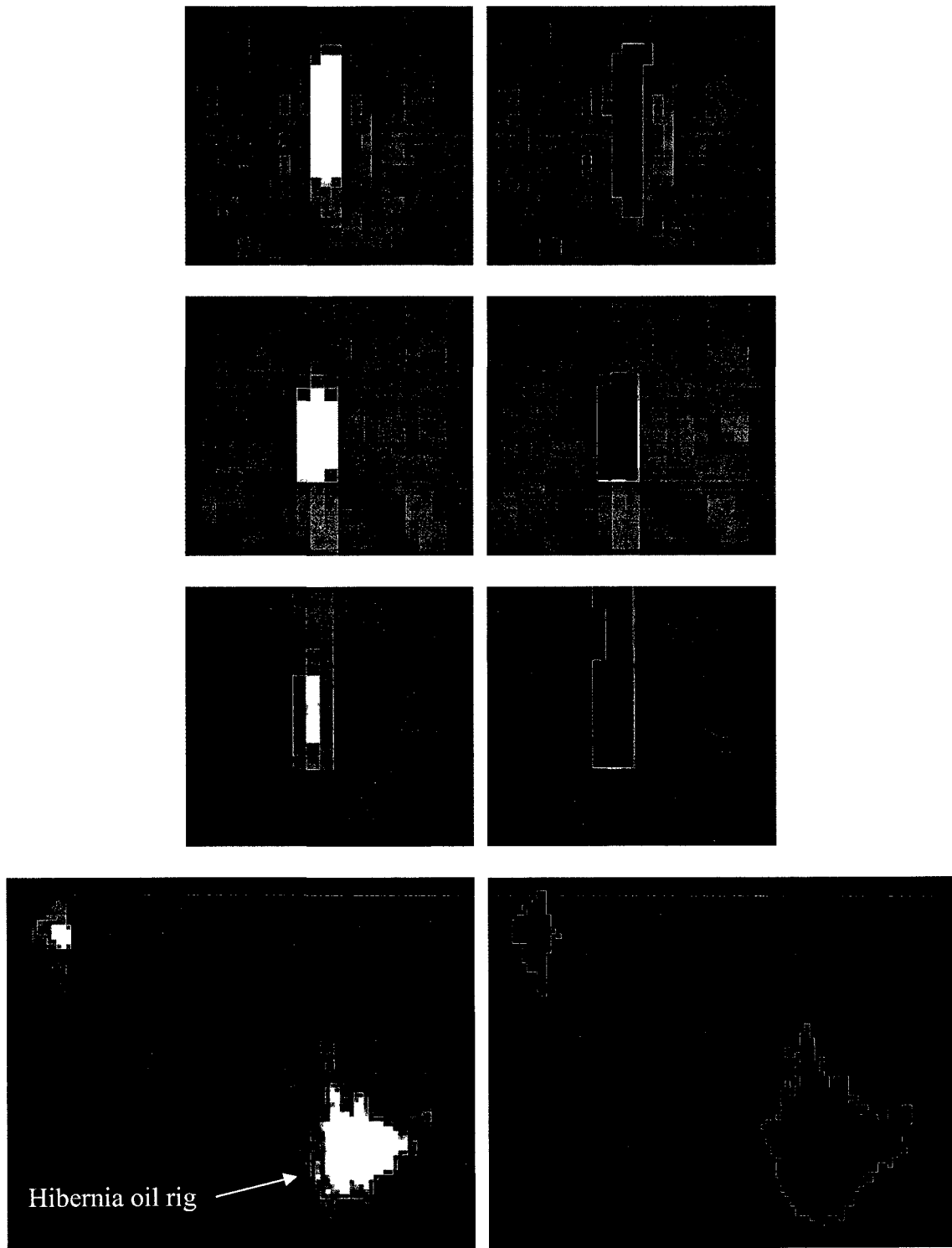


**Figure 3.3:** RADARSAT-1 W3 ships.

**Table 3.1:** Summary of RADARSAT-1 iceberg and ship data.

Date	Mode	Validation	Icebergs	Ships	Start Latitude	Start Longitude	End Latitude	End Longitude
31-May-00	W3	C-CORE	8	0	50.154177	-55.381058	49.320760	-53.333988
14-Jun-00	W2	C-CORE	10	0	49.429906	-55.103297	48.438839	-52.590392
24-Jun-00	W3	C-CORE	8	0	49.471843	-55.226611	48.597988	-53.197391
29-Apr-01	W3	PAL	1	3	48.171922	-51.704120	47.298031	-49.724600
14-May-01	W3	PAL	0	9	47.550157	-49.369573	46.066683	-48.239609
21-May-01	W3	PAL	0	3	47.167259	-48.400411	45.943083	-47.213016
24-May-01	W3	PAL	0	1	47.227293	-51.642456	45.717469	-50.293334

### 3.2.2 ENVISAT

Twenty-six images were acquired through a collaborative C-CORE / Industry initiative investigating ASAR surveillance capabilities in 2003 through 2006. Figure 3.4 shows a map of the images acquired that contain targets that have a valid correlation with ground truth. Figure 3.5 shows ground truth photos (courtesy of Denny Christian, C-CORE), ENVISAT ASAR iceberg targets for both the HH and HV channel, and the associated CFAR HH target detected mask. Available ground truth for the targets in Newfoundland waters was collected by C-CORE, PAL, and the IIP. Unfortunately, there was only secondary ground verification for some of the ship targets. This means that given the season and geographic location for these data (Vancouver Harbor, Canada), the targets were designated as manmade and thus likely to be ship. Further to this, target change detection—any target that is detected in a non-stationary position from subsequent dates—was implemented to differentiate between permanent natural scatters from manmade ones. Ultimately, primary ground truth is desired. However, the nature of moving ship targets makes them difficult to ground truth and correlate within reasonable error. From this, a decision to accept secondary truth targets was made acknowledging the increased potential for error. Table 3.2 is an image summary where 97 correlated iceberg targets and 125 correlated ship targets make up the verified data set.

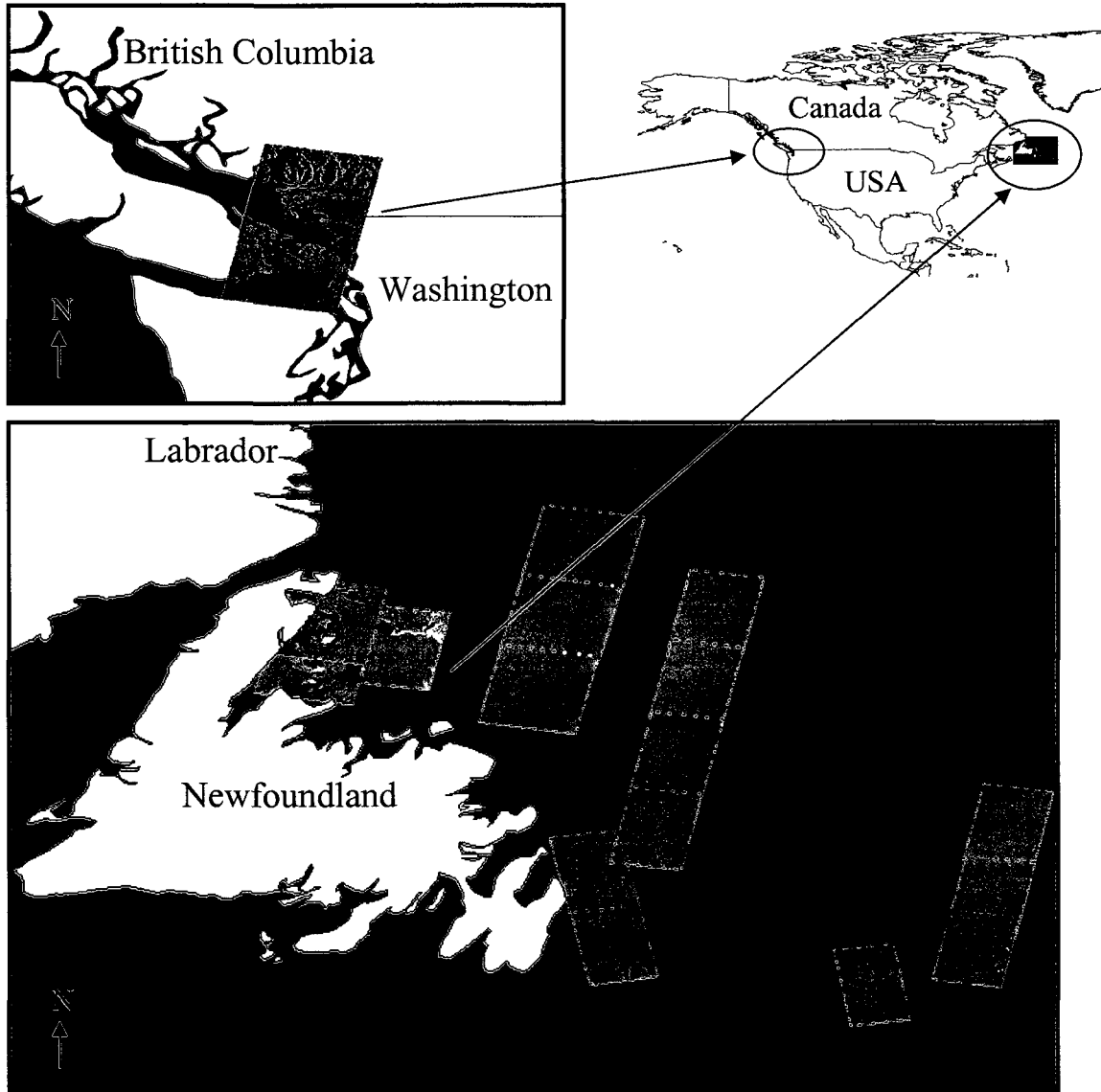


**Figure 3.4:** ENVISAT ASAR AP (HH/HV) imagery overview.

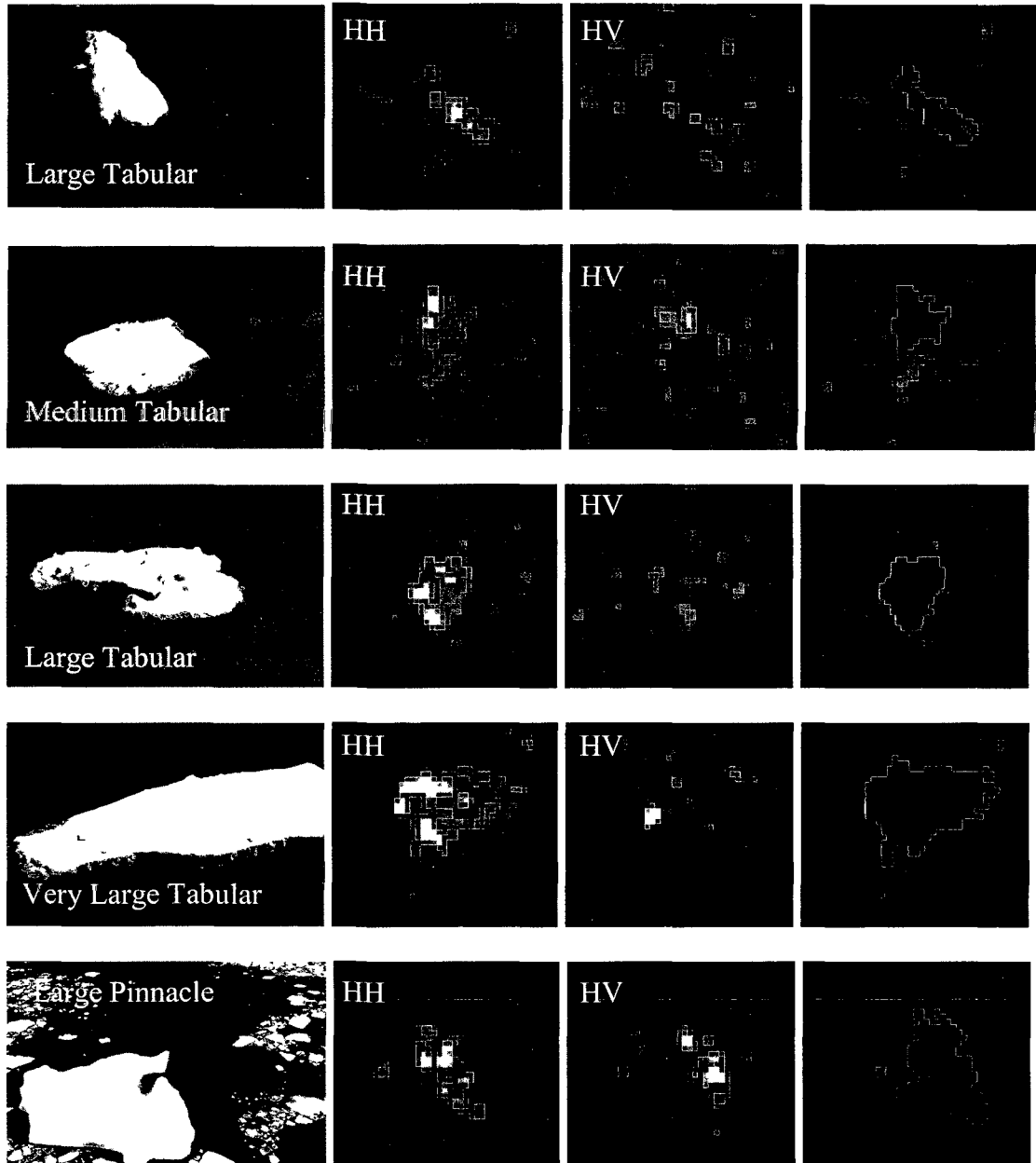


**Figure 3.5:** ENVISAT AP icebergs.

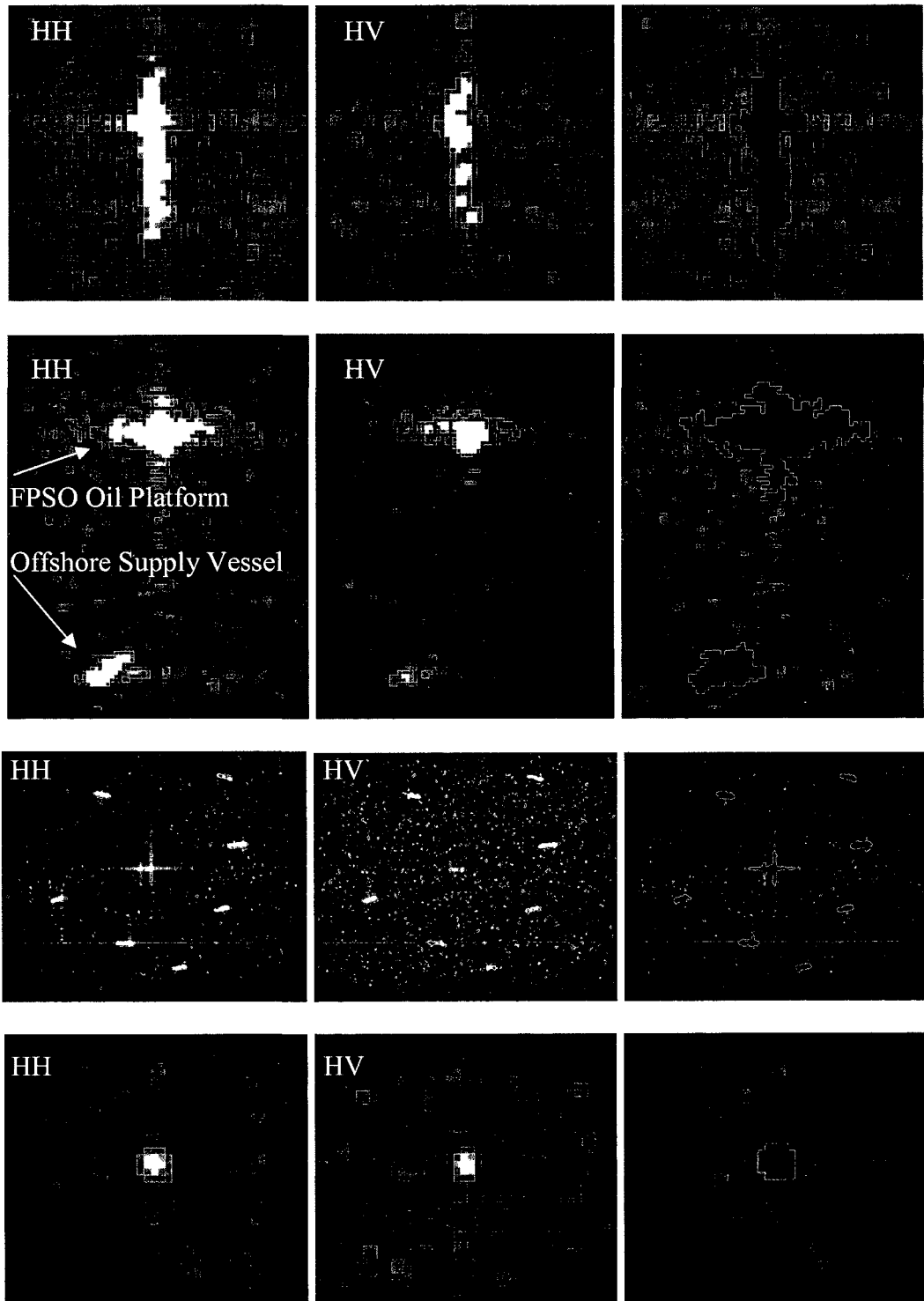


**Figure 3.6:** ENVISAT AP ships.

**Table 3.2:** Summary of ENVISAT ASAR AP (HH/HV) iceberg and ship data.

Date	Time	Mode	Validation	Iceberg	Ship	Start Latitude	Start Longitude	End Latitude	End Longitude
1-Apr-03	1:13:14	IS7	PAL	0	4	45.907547	-49.100028	46.939567	-48.583405
2-May-03	13:46:49	IS6	C-CORE	6	0	51.071134	-54.042730	50.223376	-55.298595
8-May-03	13:58:08	IS4	C-CORE	2	0	51.366650	-54.811087	50.577269	-56.325943
8-May-03	13:58:16	IS4	C-CORE	2	0	50.884712	-54.962751	50.080018	-56.466316
16-Nov-03	18:26:02	IS4	Secondary	0	22	49.570532	-122.17499	48.780146	-123.63451
16-Nov-03	18:26:14	IS4	Secondary	0	15	48.861703	-122.39001	48.145735	-123.80701
5-Dec-03	1.19:19	IS5	Secondary	0	3	46.437085	-52.331296	47.499293	-51.740996
5-Dec-03	1.19:34	IS5	Secondary	0	1	47.329201	-52.570844	48.375883	-51.965906
18-Dec-03	13:18:46	IS5	Secondary	0	4	48.834724	-46.609741	47.979835	-47.741863
18-Dec-03	13.19.01	IS5	Secondary	0	11	47.943697	-46.856062	47.103828	-47.964728
18-Dec-03	13:19.13	IS5	Secondary	0	4	47.255664	-47.042446	46.493798	-48.116156
21-Dec-03	18:26:05	IS4	Secondary	0	29	49.584023	-122.17964	48.778264	-123.64402
21-Dec-03	18:26:17	IS4	Secondary	0	23	48.874429	-122.39491	48.144941	-123.81599
15-May-04	13:35:16	IS5	PAL	9	0	51.500583	-50.158152	50.662994	-51.350434
15-May-04	13:35:31	IS5	PAL	10	0	50.625709	-50.415799	49.771999	-51.589913
15-May-04	13:35:46	IS5	PAL	9	3	49.734920	-50.673249	48.896356	-51.820781
15-May-04	13:36:02	IS5	PAL	9	5	48.796554	-50.938123	47.956750	-52.065017
21-May-04	13:46:32	IS4	IIP	9	0	52.259886	-51.632852	51.472159	-53.179761
21-May-04	13:46:47	IS4	IIP	11	0	51.385560	-51.919049	50.581436	-53.439410
21-May-04	13:47:02	IS4	IIP	9	1	50.511019	-52.198195	49.705459	-53.689842
7-Jun-2005	1:34:59	IS7	IIP	1	0	51.960474	-55.616461	51.093834	-55.616461
23-May-2006	1:35:09	IS7	IIP	1	0	53.084097	-55.921028	52.131551	-54.814687
5-Jun-2006	1:26:36	IS6	PAL	2	0	53.115993	-54.778238	52.268869	-53.463298
5-Jun-2006	01:26.50	IS6	PAL	5	0	54.081495	-55.063016	53.087059	-53.677643
8-Jun-2006	1.32:20	IS6	PAL	1	0	53.038336	-56.195559	52.208472	-54.887533
8-Jun-2006	1:32.35	IS6	PAL	11	0	54.149390	-56.524176	53.089242	-55.118618

### 3.2.3 EMISAR

Two images were acquired through a collaborative initiative investigating the capabilities of iceberg and ship classification using polarimetric sensors such as EMISAR, CV-580 SAR [45], and RADARSAT-2 [46]. This work was ongoing from 2005 to 2006. Figure 3.7 shows a map of the images acquired that contain targets that have secondary ground truth. Figure 3.8 and Figure 3.9 shows EMISAR iceberg and ship detections respectively. There was only secondary ground verification for the targets. This means that given the season and geographic location for these data, the targets were designated as ships in the Tango Denmark port and icebergs in the Greenland Sodalen Fjord.

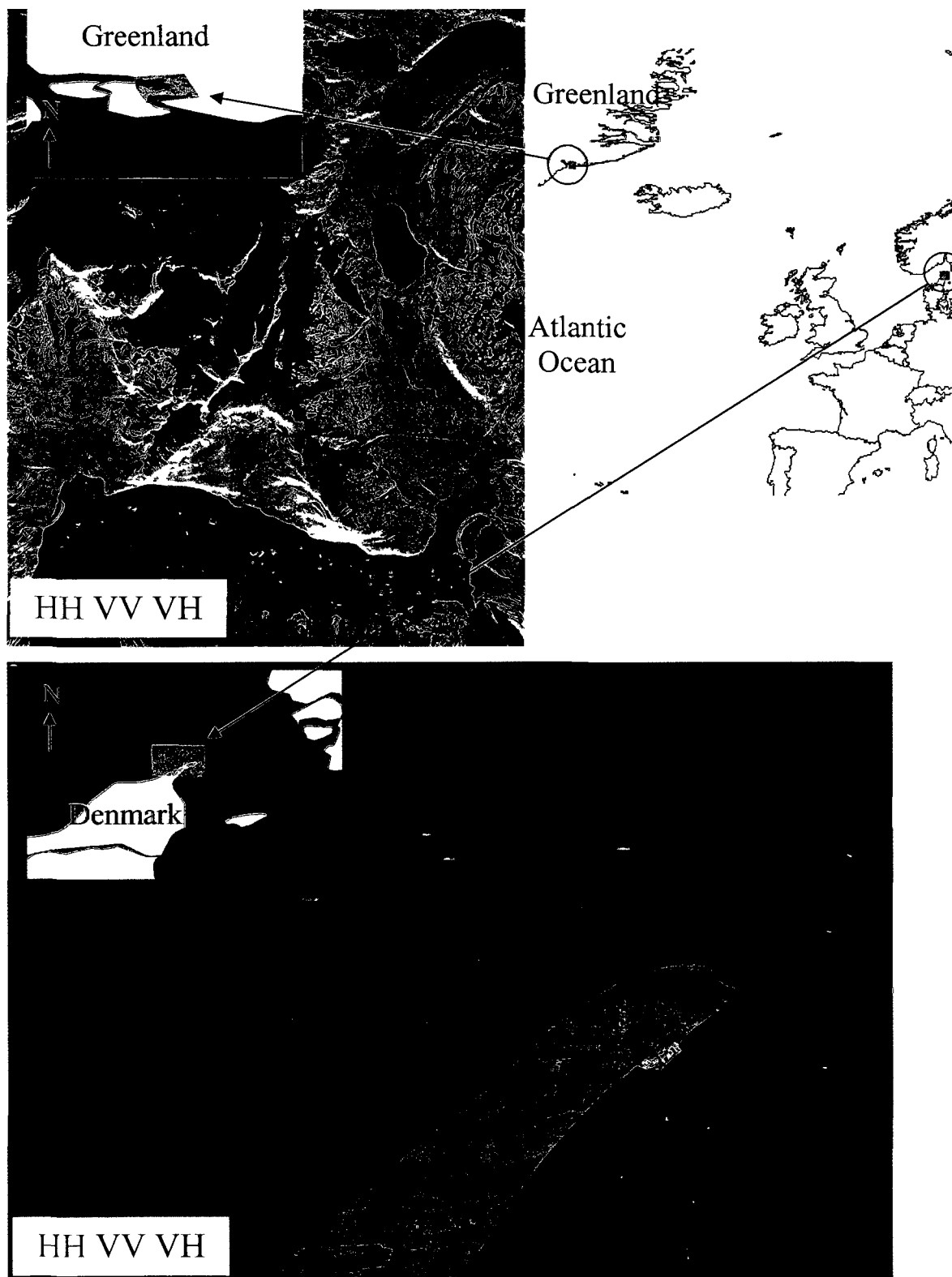


**Figure 3.7:** EMISAR imagery overview.

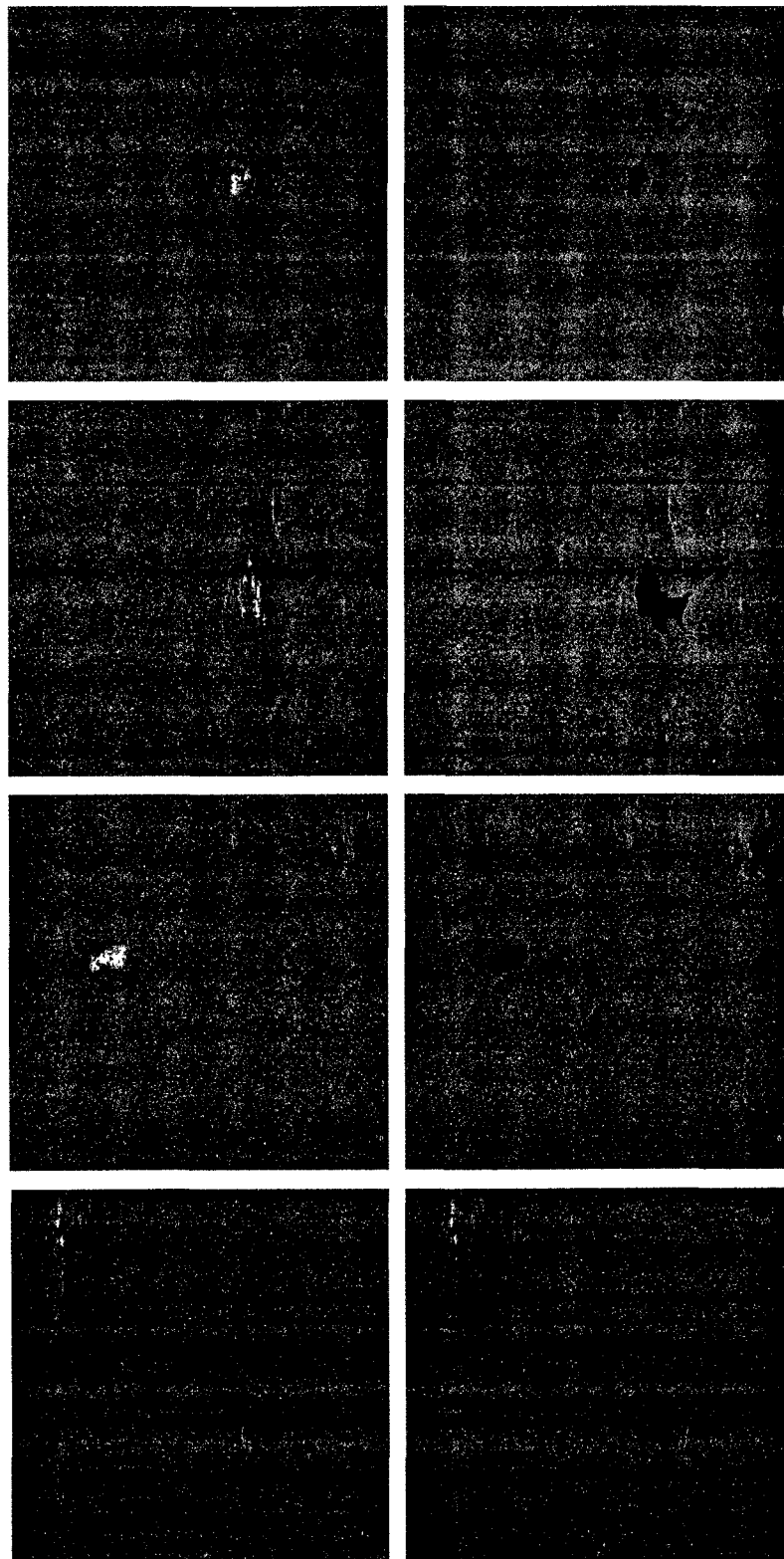


**Figure 3.8:** EMISAR HH icebergs.

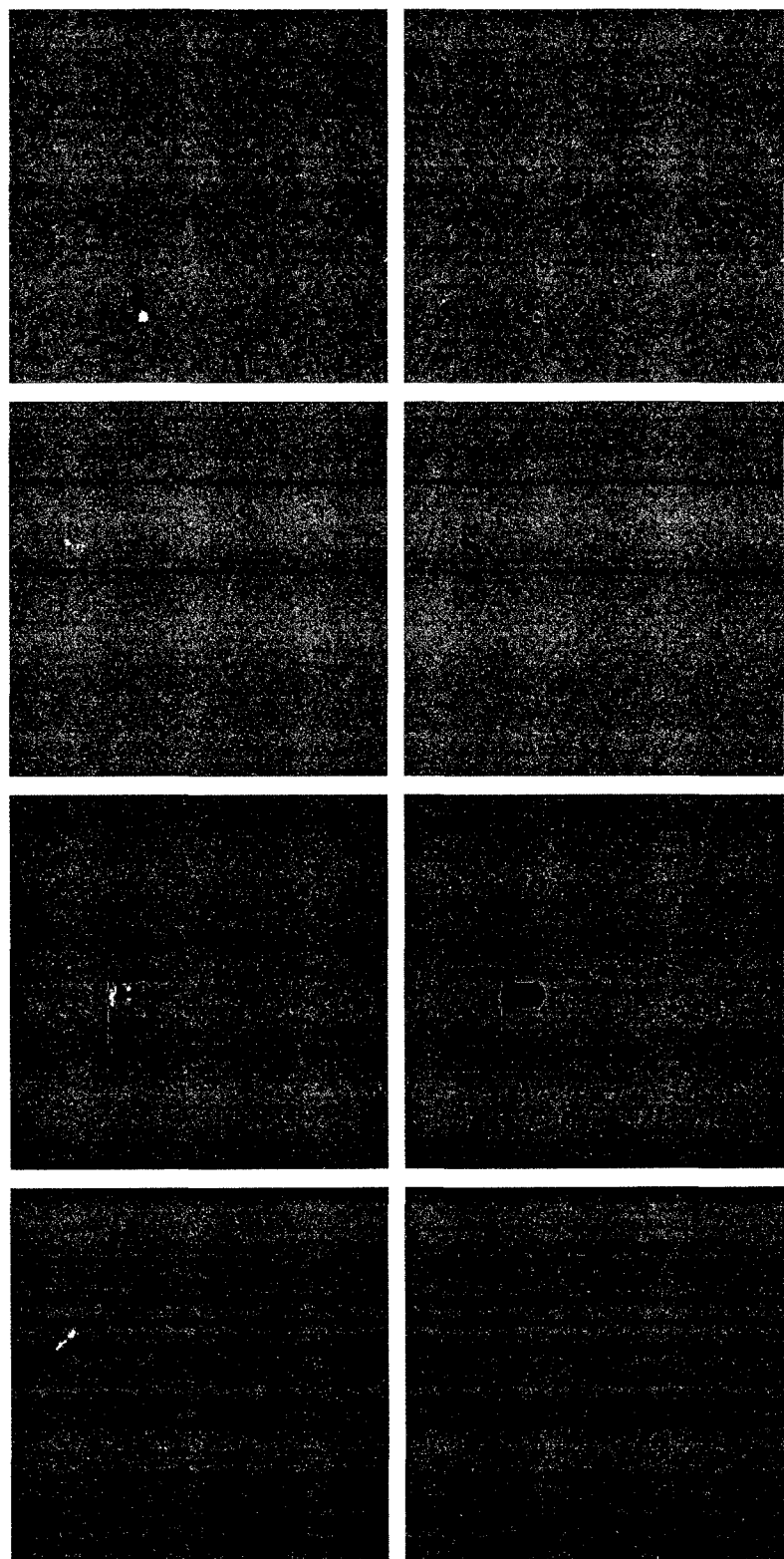


**Figure 3.9:** EMISAR HH ships.

Further to this, target change detection—any target that is detected in a non-stationary position from subsequent dates—was implemented to differentiate between permanent land forms and detected targets. Landsat optical data was used for change detection [47]. Table 3.3 is an image summary, where 78 iceberg targets and 30 ship targets make up the accepted data set.

**Table 3.3:** Summary of EMISAR iceberg and ship data.

Date	Time	Validation	Icebergs	Ships	Start Latitude	Start Longitude	End Latitude	End Longitude
18 Jul 96	10 11 00	Secondary	78	0	57 895278	10 263333	57 631944	10 691389
23 Aug 00	12 33 00	Secondary	0	30	68 246389	31 600833	68 156944	31 292778

## 4 SAR Iceberg and Ship Target Discrimination

It is ultimately desired to have the capability of passing unknown SAR targets to a classification model that makes an automated decision. For this thesis a statistical approach is taken where known targets belonging to iceberg and ship classes (identified in Chapter 3) are used to infer differentiating characteristics between classes. Of interest is the optimization of an  $n$ -class quadratic discriminant - maximum likelihood model with various feature selection methodologies. The results collected from the computational extremes of SFS and ES methods are compared. Though the optimal results acquired from the ES are of primary interest, knowing the trade-offs when comparing such sub-optimal algorithms, such as the SFS, is also useful when considering future pattern recognition work.

The methodology for algorithm development follows closely from Raudys and Jain [21] where target training data are extracted from available imagery. Post target identification, an  $n \times m$  matrix training data set is formed from all known targets, where  $n$  is the total number of targets and  $m$  is the number of features. It is this data set that is fundamental to this work. From the training set, a feature subset is likely to exist that will increase classification performance, lighten computational complexity and increase robustness of the discrimination algorithm. Using the SFS, ES, ERS, and LES methods described in Section 2.3.2 and Section 5.4, feature spaces are evaluated by testing the training data and evaluating the classification accuracy. The RADARSAT-1 data set evaluated ES that was implemented through parallel processing as described in Section 5.5. A cross-validation leave-one-out methodology was used for its nominally non-biased results and maximizing training set potential properties. Appendix VI describes the confusion matrix notation which has been used to present all feature selection iceberg and ship classification results.

For the RADARSAT-1 target data, four combinations of feature selection paired with the maximum likelihood model were evaluated: SFS 2-Class, ERS 2-Class, ES 2-Class, and SFS 4-Class. A two class model has a binary decision: iceberg or ship. The four class

model was investigated due to expected physical scattering differences between small wooden fishing boats and large metal vessels. Since the maximum likelihood model is dependent on Gaussian feature spaces when trying to obtain minimum error rates [20], a potential gain was expected from splitting the ship class based on size.

For the ENVISAT ASAR target data, four combinations of feature selection paired with the maximum likelihood model were evaluated: SFS 2-Class, ERS 2-Class, LES 2-Class, and SFS 6-Class. A two class model has a binary decision: iceberg or ship. The LES was used instead of ES to demonstrate LES as a viable option. Figure 4.1 shows a ES benchmark plot of the required computation time as a function of the number of features. From this, the ERS can exhaustively run a 21 feature set on the order of a day. The LES was evaluated for 3.5 days.

In addition, a 6 class model is presented for the ENVISAT data. It takes into account the expected physical scattering differences between small wooden fishing boats, medium sized ships with significant structure, and large metal vessels. Since the maximum likelihood model is dependent on Gaussian feature spaces when trying to obtain minimum error rates [20], a potential gain was expected from splitting the ship class into separate groups based on size.

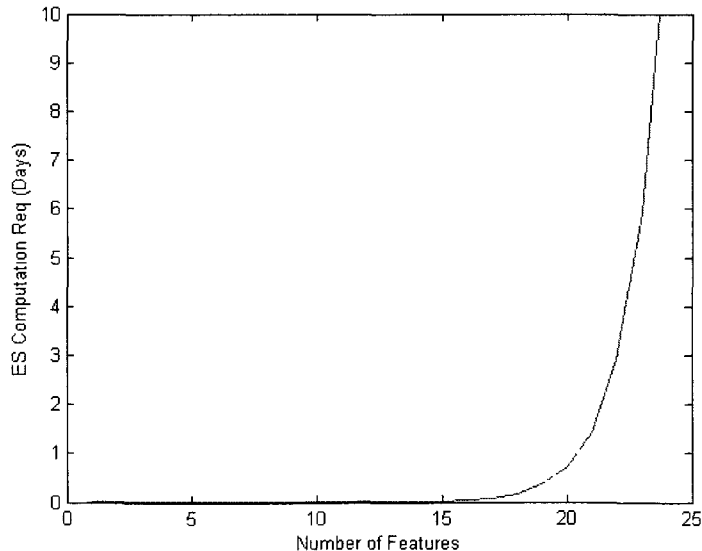


**Figure 4.1:** ENVISAT ASAR ES benchmark.

The EMISAR data set has only been evaluated using the SFS 2-Class feature selection with the maximum likelihood model. SFS allowed for rapid algorithm development when evaluating the various polarization (feature) and decomposition combinations. Using ERS, LES or ES as presented here would make this work a time consuming task. Several permutations of polarization modes similar to RADARSAT-1, ENVISAT AP, and RADARSAT-2 were evaluated: Quad Polarization (HH/HV/VH/VV with phase) with and without Cameron decomposition metrics [7], dual channel HH/HV, dual channel HH/VV, dual channel VH/VV, single channel HH and single channel VV. This data set gives insight into the potential gains of using various polarization combinations with high resolution SAR.

## **4.1 RADARSAT-1**

The 43 (27 iceberg and 16 ship) detected targets of interest were used to extract features for training the proposed four feature selection algorithms. Features included in the data set are  $\sigma^0$  mean,  $\sigma^0$  variance,  $\sigma^0$  maximum pixel value, area, major axis, minor axis, circularity, compactness, contour length, convexity, maximum diameter, anisometry, bulkiness, structure factor, inner circle radius, product of inertia, M20 (2<sup>nd</sup> order line moment), M02 (2<sup>nd</sup> order column moment), main axis inertia, 2<sup>nd</sup> main axis inertia, M21 (3<sup>rd</sup> order line moment), M12 (3<sup>rd</sup> order column moment), M03 (3<sup>rd</sup> order column moment), M30 (3<sup>rd</sup> order line moment), orientation, outer circular radius, outer rectangle length radius, outer rectangle width radius and HH signal to clutter.

### **4.1.1 SFS 2-Class**

The SFS 2-Class algorithm coupled with the maximum likelihood discriminate model was found to have a leave-one-out accuracy of 81.4%, since 35 of the 43 targets were correctly identified (Table 4.1). The feature set identified producing these results was the six feature space:  $\sigma^0$  mean,  $\sigma^0$  variance, circularity, structure factor, orientation and HH signal-to-clutter.

#### **4.1.2 ES 2-Class**

The ES 2-Class algorithm coupled with the maximum likelihood discriminate model was found to have a leave-one-out accuracy of 90.7% (Table 4.1). The feature set identified producing these results was the eight feature space:  $\sigma^0$  mean,  $\sigma^0$  maximum, minor axis, M30, orientation, outer circular radius, outer rectangle length radius and outer rectangle width radius.

#### **4.1.3 ERS 2-Class**

The ERS 2-Class algorithm coupled with the maximum likelihood discriminate model was found to have a leave-one-out accuracy of 90.7% (Table 4.1). The feature set being the same one identified in the ES 2-Class was the eight space:  $\sigma^0$  mean,  $\sigma^0$  maximum, minor axis, M30, orientation, outer circular radius, outer rectangle length radius and outer rectangle width radius.

#### **4.1.4 SFS 4-Class**

The SFS 4-Class algorithm coupled with the maximum likelihood discriminate model was found to have a leave-one-out accuracy of 86.0% (Table 4.1). Here a decision tree approach was taken where target size was used to navigate the tree. This size criterion was empirically optimized for a two branch tree. As seen in Figure 4.2, the first branch of the decision tree criteria is set for large targets (greater than or equal to 35 pixels), and small targets (less than 35 pixels). For small targets the selected feature space consisted of: minor axis, M20 and outer rectangle length radius. For the larger targets,  $\sigma^0$  variance, major axis, convexity and anisometry were the feature space selected.

### **4.2 *Discussion of RADARSAT-1 Results***

The maximum accuracies obtained for the methods investigated ranged from 81 to 91%. The ES and ERS (working on a ranked 24 feature subset) converged to the same feature set finding the highest performance combination of 91%. The SFS 4-Class focuses on optimization within classes, and fell short of the ES 2-Class methods. It is speculated that

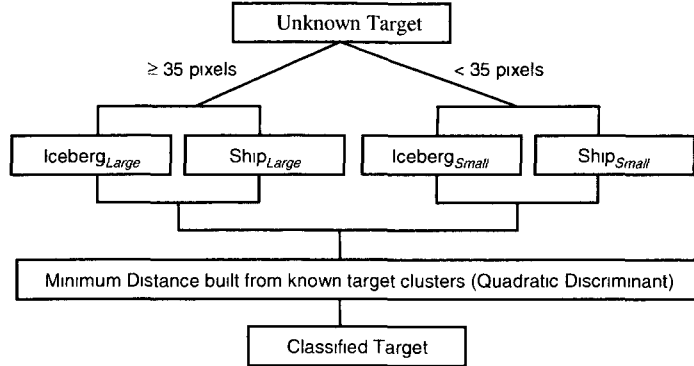


**Figure 4.2:** RADARSAT-1 SFS – 4 class decision tree structure.

this is due to an insufficient training data population (43 targets) being further reduced to represent four classes as opposed to two.

As seen in Figure 4.3, the SFS had a reasonable performance gain with a feature reduction from 28 to 6, however the ES and ERS provide a more significant improvement. Further to this, ERS found the same feature subset as ES, thus finding the optimal feature combination on the order of a day on a single desktop computer. It is important to note that due to the limited number of samples in the ship class, the covariance matrix singularity limited the search space for all methods employed. Also from Figure 4.3 the ES shows the classification performance increase as a function of increasing dimensionality.

Notably, the ES was benchmarked for this data set to be on the order of several months of computation time using a 3 GHz Intel Pentium 4 processor with 1 Gigabyte of RAM. The ES was accomplished though parallel processing (see Section 5.5) on 14 desktop computers (similar to the aforementioned performance specification) in order to make the results available in days rather than months. The development of this parallel processing code was solely developed for this thesis by the author. In contrast to this significant computational effort, the ERS with only four of the original features removed was completed over a weekend (72 hours) on one desktop computer. The SFS algorithm in both 2 and 4 class instances was evaluated on the order of minutes. Section 5.4 presents

the specific benchmarked time results for the ES, ERS, and SFS feature selection methods employed.

Based on these results, for RADARSAT-1 wide mode iceberg and ship classification, the 2-class maximum likelihood model with feature space  $\sigma^0$  mean,  $\sigma^0$  maximum, major axis, M30, orientation, outer circular radius, outer rectangle length radius, and outer rectangle width radius is recommended.

**Table 4.1:** Summary of RADARSAT-1 iceberg and ship classification accuracy.

		SFS 2 – Class		ERS 2 – Class				
		Truth		Truth				
Classified		Iceberg	Ship	Iceberg	Ship	Iceberg	Ship	
		Iceberg	23	4		Iceberg	26	3
Classified		Ship	4	12		Ship	1	13
		ES 2 – Class		SFS 4 – Class				
		Truth		Truth				
Classified		Iceberg	Ship	Iceberg	Ship	Iceberg	Ship	
		Iceberg	26	3		Iceberg	23	2
Classified		Ship	1	13		Ship	4	14
		SFS 4 – Class		SFS 4 – Class				
		area $\leq 35$		area $> 35$				
Classified		Truth		Truth				
		Iceberg	Ship	Iceberg	Ship	Iceberg	Ship	
Classified		Iceberg	8	0		Iceberg	15	2
		Ship	2	6		Ship	2	8

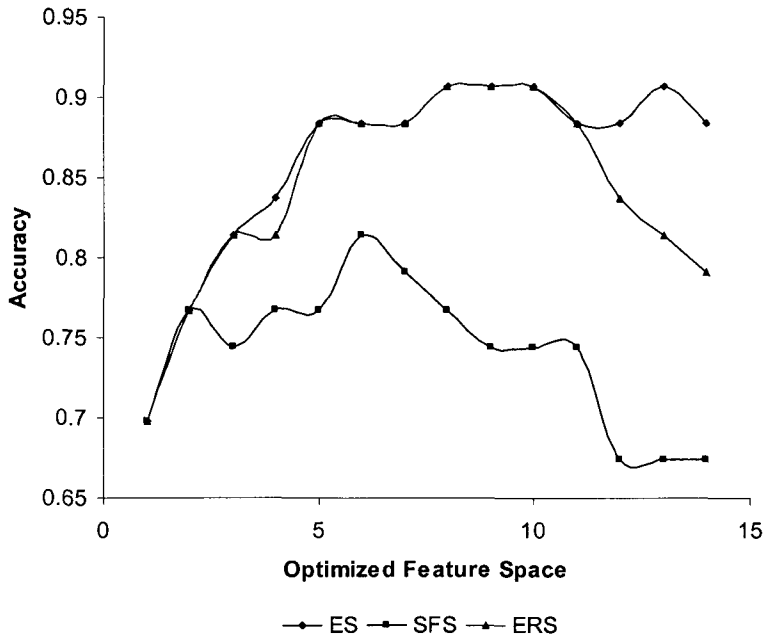


**Figure 4.3:** RADARSAT-1 feature selection comparison.

### 4.3 ENVISAT AP HH/HV

The 222 (97 iceberg and 125 ship) detected targets of interest were used to extract features for training the proposed four feature selection algorithms. Features included in the data set are HH signal-to-clutter ratio, HV signal-to-clutter ratio, HH mean  $\sigma^o$ , HH variance  $\sigma^o$ , HH maximum  $\sigma^o$ , area, major axis, minor axis, circularity, compactness, contour length, convexity, maximum diameter, anisometry, bulkiness, structure factor, inner circle radius, product of inertia, M20 (2<sup>nd</sup> order line moment), M02 (2<sup>nd</sup> order column moment), main axis inertia, 2<sup>nd</sup> main axis inertia, M21 (3<sup>rd</sup> order line moment), M12 (3<sup>rd</sup> order column moment), M03 (3<sup>rd</sup> order column moment), M30 (3<sup>rd</sup> order line moment), outer circular radius, outer rectangle length radius and outer rectangle width radius. Here the signal-to-clutter ratios are the target maximum  $\sigma^o$  pixel value ratio with the mean  $\sigma^o$  background clutter value. If a target was not detected in the HV channel, the maximum target  $\sigma^o$  HV pixel value was extracted using the corresponding HH detection mask.

### **4.3.1 SFS 2– Class**

The SFS 2–Class algorithm coupled with the maximum likelihood discriminate model was found to have a leave-one-out accuracy of 91.4%, since 203 of the 222 targets were correctly identified (Table 4.2). The feature set identified producing these results was the seven space: HV signal-to-clutter ratio, HH mean  $\sigma^0$ , HH variance  $\sigma^0$ , area, circularity, convexity and structure factor.

### **4.3.2 ERS 2–Class**

The ERS 2–Class algorithm coupled with the maximum likelihood discriminate model was found to have a leave-one-out accuracy of 91.9% (Table 4.2). The feature set identified producing these results was the five space: HV signal-to-clutter ratio, HH variance  $\sigma^0$ , area, structure factor and inner circle radius.

### **4.3.3 LES 2–Class**

The LES 2–Class algorithm coupled with the maximum likelihood discriminate model was found to have a leave-one-out accuracy of 91.9% (Table 4.2). The feature set identified producing these results was the five space: HV signal-to-clutter ratio, HH variance  $\sigma^0$ , area, structure factor and inner circle radius.

### **4.3.4 SFS 6–Class**

The SFS 6–Class algorithm coupled with the maximum likelihood discriminate model was found to have a leave-one-out accuracy of 94.1% (Table 4.2). Here a decision tree approach was taken where target size and detection confidence (an IDS specific metric) were used to navigate the tree. The combination of size criterion and detection confidence was empirically optimized for a three branch. As seen in Figure 4.4, the first branch of the decision tree criteria is set for large targets (greater than or equal to 70 pixels), next is less than 70 pixels with a high detection confidence (HDC), and finally the

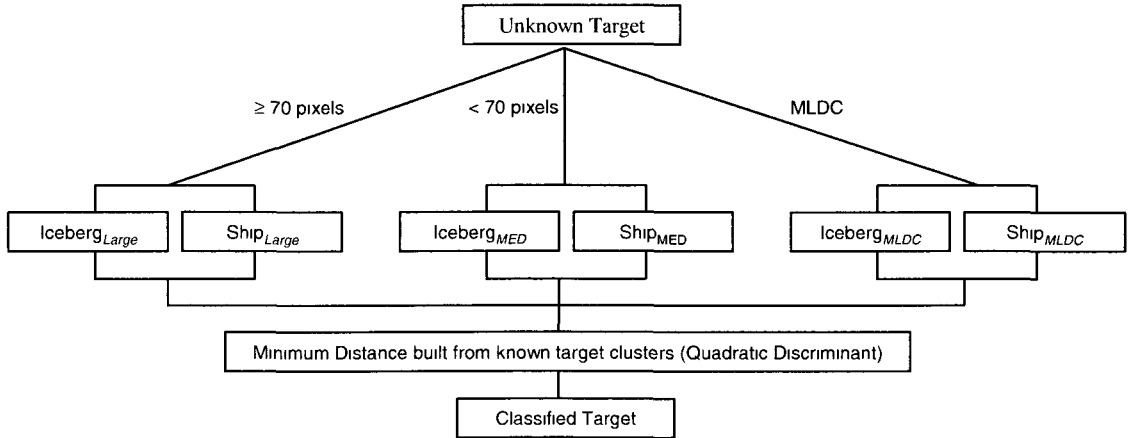


**Figure 4.4:** SFS ENVISAT AP 6-Class decision tree structure.

remaining medium and low detection confidence (MDC and LDC) targets. The IDS detection confidence metric is a measure of target strength based on a combination of intensity and area. Here each branch of the decision tree had unique feature spaces identified. For MDC and LDC targets the feature space was anisometry. For HDC targets less than 70 pixels the feature space was HH signal-to-clutter ratio, HV signal-to-clutter ratios, and circularity. For targets greater than or equal to 70 pixels the feature space was the HV signal-to-clutter ratio and HH  $\sigma^0$  variance.

#### 4.4 Discussion of ENVISAT AP HH/HV Results

The maximum accuracies obtained for the methods investigated ranged from 91.4 to 94.1%. The SFS 6-Class found the highest performance combination. The LES and RES converged to the same feature set and thus the same classification accuracy. The SFS 2-Class accuracy results were nominally less than LES and RES (one ship target in 222). Of interest, a user-based six class knowledge system was shown to outperform the two class models. This was achieved though the six class model using the computationally lighter SFS feature selection algorithm compared to the two class systems which incorporated the ES variants. Common features selected by the methods tested were HV signal-to-clutter ratio, HH variance  $\sigma^0$ , area, circularity OR inner circle radius and structure factor.

As a matter of interest relative to SAR iceberg backscatter, the HH variance  $\sigma^0$  was shown to significantly improve classification performance and was routinely selected by feature selection methods tested. This is in agreement with early C-CORE works [3] where large vessels were observed to have a higher variance compared to icebergs detected in RADARSAT-1 Fine mode data. As well, HV signal-to-clutter ratio was shown to significantly add to the classification performance. This is in agreement with early works by the author [19] on a limited large vessel and iceberg training data set. Interestingly enough, the SFS algorithm working on 29 features selected these two dominant features. From Figure 4.5 the large (greater than 70 pixels at 12.5 meter pixel spacing) ship and iceberg category was observed to have a no error classification boundary based on the limited 26 iceberg and 56 ship samples available.

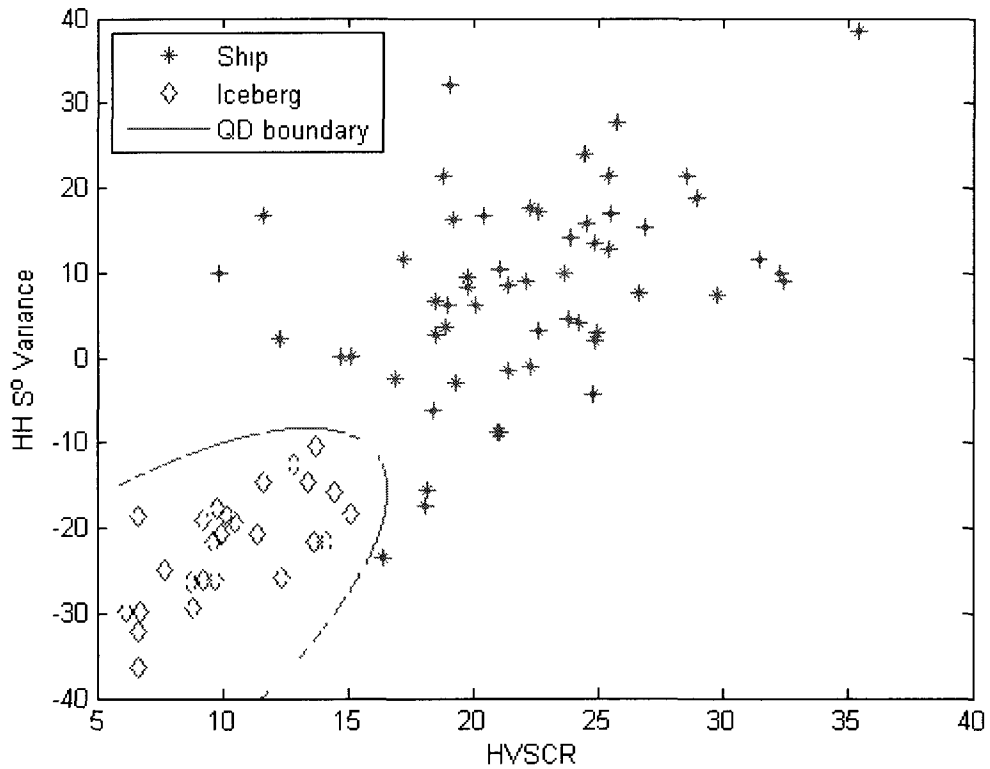


**Figure 4.5:** ENVISAT ASAR HH/HV: Large iceberg and ship classification.

The SFS, ERS and LES methods all performed extremely similarly. As mentioned previously, there was only one misclassified ship target separating the SFS from the ERS and LES obtained results. From Figure 4.6, the ERS does successfully find the globally optimal results for the first six feature spaces benchmarked by LES. These results are encouraging for the robustness of these three feature selection methods, as they converge to common features and accuracies even though they vary significantly in methodology.

The ES was benchmarked for this data set to be on the order of a year using a 3 GHz Intel Pentium 4 processor with 1 Gigabyte of RAM. The ES was not evaluated partly due to the ERS success in the RADARSAT-1 data case, the extensive computational effort required even on a distributed computer system, overhead with manually distributing/harvesting data to the computer cluster, and the fact that the LES will give the

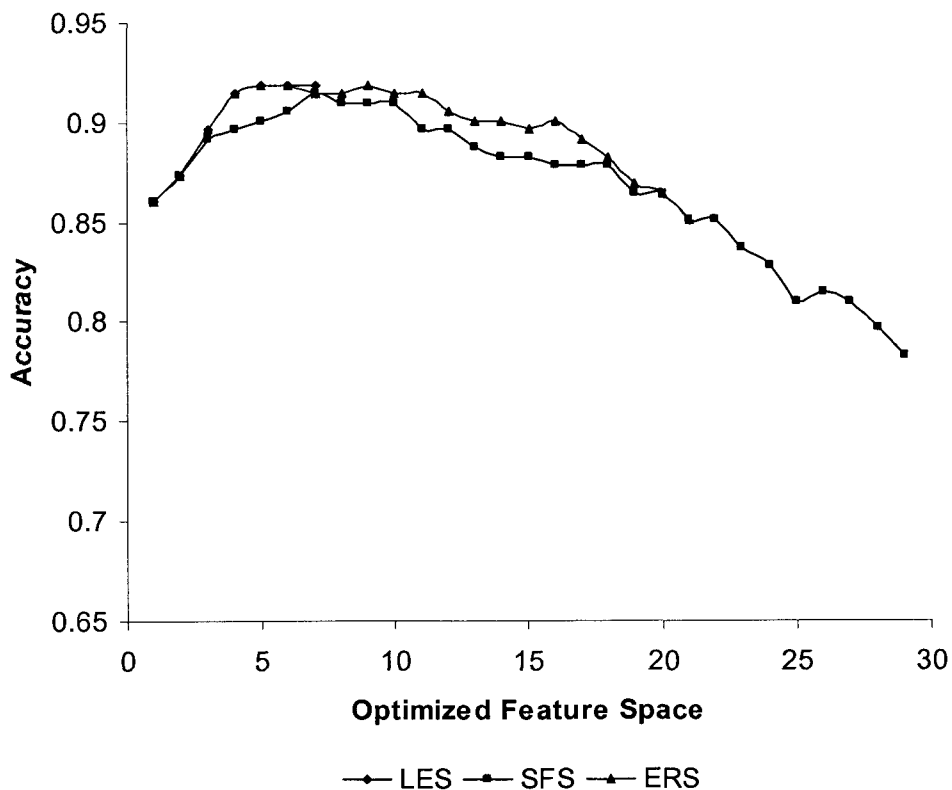


**Figure 4.6:** ENVISAT ASAR feature selection comparison.

optimal feature set up to the space evaluated. The ERS with eight of the original features removed was completed in little over a day and the LES over a weekend (72 hours) on one desktop computer. The SFS algorithm in both 2 and 6 class instances was evaluated on the order of minutes. Section 5.4 presents the specific benchmarked time results for the LES, ERS and SFS feature selection methods employed.

**Table 4.2:** Summary of ENVISAT ASAR iceberg and ship classification accuracy.

**SFS 2 – Class**

		Truth	
		Iceberg	Ship
Classified	Iceberg	<b>91</b>	13
	Ship	6	<b>112</b>

**ERS 2 – Class**

		Truth	
		Iceberg	Ship
Classified	Iceberg	<b>91</b>	12
	Ship	6	<b>113</b>

**LES 2 – Class**

		Truth	
		Iceberg	Ship
Classified	Iceberg	<b>91</b>	12
	Ship	6	<b>113</b>

**SFS 6 – Class**

		Truth	
		Iceberg	Ship
Classified	Iceberg	<b>89</b>	5
	Ship	8	<b>120</b>

**SFS 6 – Class**

(MDC/LDC)

		Truth	
		Iceberg	Ship
Classified	Iceberg	<b>14</b>	0
	Ship	2	<b>6</b>

**SFS 6 – Class**

(HDC/area<70)

		Truth	
		Iceberg	Ship
Classified	Iceberg	<b>49</b>	5
	Ship	6	<b>58</b>

**SFS 6 – Class**

(HDC/area>=70)

		Truth	
		Iceberg	Ship
Classified	Iceberg	<b>26</b>	0
	Ship	0	<b>56</b>

Based on these results, for ENVISAT AP HH/HV iceberg and ship classification, the 6-class (see Figure 4.4) maximum likelihood model is suggested. For small-low intensity targets (MLDC) the maximum likelihood model using the one feature space, anisometry is recommended. For medium size targets (HDC less than 70 pixels) the maximum likelihood model using the three feature space: HH signal-to-clutter ratio, HV signal-to-clutter ratios and circularity is recommended. For large sized targets (HDC greater than or equal to 70 pixels) the maximum likelihood model using the two feature space HV signal-to- clutter ratio and HH  $\sigma^0$  variance is recommended.

## 4.5 EMISAR

The 108 (78 icebergs and 30 ships) detected EMISAR targets were used to extract features for training the SFS maximum likelihood models. Of interest to this work is the classification performance relative to the levels of polarization. Recall that EMISAR is a quad polarization sensor, thus single and dual polarization combinations are inherently contained. When quad polarization data is collected, there is potential for improved target detection and classification accuracy by using polarimetric SAR decomposition methods [48, 49]. Features included in the data set are intensity, shape and decomposition based:  $\sigma^0$  mean (HH, VV, HV),  $\sigma^0$  variance (HH, VV, HV),  $\sigma^0$  maximum pixel value (HH,VV,HV), area, major axis, minor axis, eccentricity, orientation, equivalent diameter and Cameron metrics [7]. The Cameron Decomposition produces a pixel-based classification for the scatter classes: dihedral, narrow diplane, diplane, cylinder, trihedral and quarter wave. To integrate this pixel-based method into a target classification regime, two groups of target-based metrics were formed. The first metric group takes the ratio of trihedral, dihedral, dipole, narrow diplane, cylinder, and quarter wave to the total number of targets pixels. The second metric group was designed to capture the distribution or clustering effect of dominant class types. Here the mean of the neighboring (8-connected) like class pixels are calculated for targets: mean neighboring trihedral, mean neighboring dihedral, mean neighboring dipole, mean neighboring narrow diplane, mean neighboring cylinder and mean neighboring quarter wave.

### **4.5.1 Quad Polarization with Cameron**

The SFS 2-Class algorithm coupled with the maximum likelihood discriminate model was found to have a leave-one-out accuracy of 99%, since 105 of the 106 targets were correctly identified (Table 4.3). The feature set identified using the SFS method was the two feature space: eccentricity and quarter wave. The quarter wave and eccentricity plot (see Figure 4.7) for the iceberg and ship targets presented here is almost ideal. Quarter wave is one of six symmetric scatter types defined by the Cameron decomposition. Figure 4.7 demonstrates the class separation based on the relatively low ship quarter wave measures compared to that of icebergs. Eccentricity is a shape measure that describes a target's difference of ellipse foci to the major axis. Thus it is a measure that reflects the extremes of circularity to linearity. From Figure 4.7 it is apparent that iceberg eccentricity has a wider range than that of ship eccentricity, this has been attributed to the random size and shape of icebergs as opposed to the well defined structure of man-made ship targets.

### **4.5.2 Quad Polarization**

The SFS 2-Class algorithm coupled with the maximum likelihood discriminate model was found to have a leave-one-out accuracy of 97% (Table 4.3). The feature set producing these results was: area, orientation, equivalent diameter, HV  $\sigma^0$  mean and HV  $\sigma^0$  variance. It is important to note that this combination of features is not unique to quad polarization and both the dual cross polarization combinations that contain the HV channel (HH/HV and VH/VV) produce the same results.

### **4.5.3 Dual Polarization HH/HV**

The SFS 2-Class algorithm coupled with the maximum likelihood discriminate model was found to have a leave-one-out accuracy of 97% (Table 4.3). Refer to Section 4.5.2.

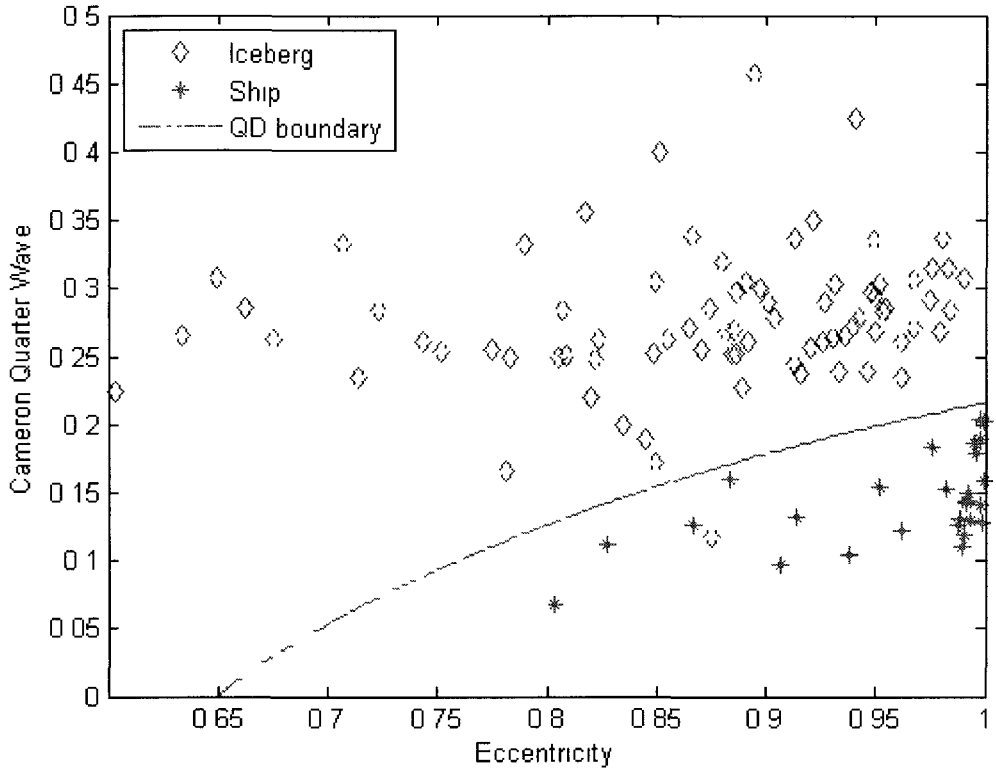


**Figure 4.7:** EMISAR quad polarization iceberg and ship classification.

#### 4.5.4 Dual Polarization HH/VV

The SFS 2-Class algorithm coupled with the maximum likelihood discriminate model was found to have a leave-one-out accuracy of 96% (Table 4.3). The feature set producing these results was: area, eccentricity, orientation, equivalent diameter, HH  $\sigma^0$  mean, VV  $\sigma^0$  mean and VV  $\sigma^0$  variance.

#### 4.5.5 Dual Polarization VH/VV

The SFS 2-Class algorithm coupled with the maximum likelihood discriminate model was found to have a leave-one-out accuracy of 97% (Table 4.3). Refer to Section 4.5.2.

#### **4.5.6 Single Polarization HH**

The SFS 2-Class algorithm coupled with the maximum likelihood discriminate model was found to have a leave-one-out accuracy of 94% (Table 4.3). The feature set producing these results was: area, eccentricity, orientation and equivalent diameter.

#### **4.5.7 Single Polarization VV**

The SFS 2-Class algorithm coupled with the maximum likelihood discriminate model was found to have a leave-one-out accuracy of 95% (Table 4.3). The feature set producing these results was: area, eccentricity, orientation, equivalent diameter, VV  $\sigma^0$  mean and VV  $\sigma^0$  variance.

#### **4.5.8 Single Polarization HH (without shape)**

The SFS 2-Class algorithm coupled with the maximum likelihood discriminate model was found to have a leave-one-out accuracy of 79% (Table 4.3). The feature set producing these results was HH  $\sigma^0$  mean, HH  $\sigma^0$  variance and HH  $\sigma^0$  maximum. This combination was included to demonstrate the significant effect that removing shape metrics has on the classification of these targets.

### **4.6 Discussion of EMISAR Results**

The maximum accuracies obtained for the methods investigated ranged from 79% to 99%. The SFS 2-Class was exclusively used for feature selection to allow rapid algorithm development and polarization comparison. Generally, quad polarization (with target decomposition metrics) outperformed dual polarization, and dual polarization outperformed single polarization for iceberg and ship classification.

As seen in Figure 4.7, the Cameron Decomposition feature quarter wave and the shape measure eccentricity feature space is almost non-error. These results are very promising as the soon-to-be-launched RADARSAT-2 will produce high resolution, quad polarization data similar to that of EMISAR data. From this, we expect that

RADARSAT-2 quad polarization modes will have an improved probability of classification for all size targets over dual polarization modes.

When offering an operational surveillance program, resolution, NESZ and polarization are often traded for improved swath coverage. The quad polarization results (without Cameron) were observed to produce a high classification accuracy of 97%. This is of significant importance because the feature set selected was composed of CFAR detected shape metrics and exclusively cross polarization (HV) intensity metrics. This implies that any dual cross polarization (HH/HV OR VH/VV) combination should have almost the classification accuracy of quad polarization. HV was not evaluated as a single polarization mode by itself as it has not been traditionally offered in that way. Another point of consideration is that spaceborne SAR will have limiting factors over airborne SAR with respect to NESZ. It is speculated that the cross-polarized (HV) channel with a low NESZ (like that of the airborne EMISAR sensor) would produce superior classification potential to that of co-polarized channels (HH or VV). Thus, a single cross polarization (HV) mode—with low NESZ, high resolution, and large swath coverage—would be a desirable mode of choice for future iceberg and ship classification research and development.

Dual polarization results were always better than single polarization. Dual polarization combinations were observed to have a range of classification accuracy ranging from 96 to 97%, with both dual cross polarization combinations (HH/HV OR VH/VV) nominally outperforming the dual co-polarization. Common features selected by the SFS for all dual polarization combinations were area, orientation, equivalent diameter,  $\sigma^0$  mean and  $\sigma^0$  variance.

Single polarization (HH or VV) results have a range of classification accuracy from 94 to 95%, with VV nominally outperforming HH. As a special case, HH without shape features was also run and produced 79% accuracy.

Notable were the generally high classification rates observed, compared to single and dual polarization RADARSAT-1 and ENVISAT AP results in Sections 4.1 and 4.3. This has been attributed to the higher resolution and significantly lower noise floor of the EMISAR sensor.

The SFS algorithm was successful in evaluating combinations of polarization in this data set. Due to the inexpensive computation and the confidence built with using the SFS algorithm on the RADARSAT-1 and ENVISAT data sets, all polarization combinations were compiled, collected and evaluated in relatively short order.

Based on these results of quad polarization SAR, the Cameron decomposition quarter wave and eccentricity feature space is a near-optimal way to discriminate iceberg and ship targets. Dual and single polarization (HH/HV, HH/VV, VH/VV, HH, VV) combinations are relatively similar in performance with shape-based area, eccentricity, orientation, equivalent diameter, and intensity-based  $\sigma^0$  metrics being repeatedly selected.

**Table 4.3:** Summary of EMISAR iceberg and ship classification accuracy.

**Quad**

+ Cameron

Truth

		Iceberg	Ship
Classified	Iceberg	78	0
	Ship	1	27

**Quad**

Truth

		Iceberg	Ship
Classified	Iceberg	77	1
	Ship	2	26

**Dual**

HH/VV

Truth

		Iceberg	Ship
Classified	Iceberg	79	4
	Ship	0	23

**Dual**

HH/HV

Truth

		Iceberg	Ship
Classified	Iceberg	77	1
	Ship	2	26

**Dual**

VH/VV

Truth

		Iceberg	Ship
Classified	Iceberg	77	1
	Ship	2	26

**Single**

VV

Truth

		Iceberg	Ship
Classified	Iceberg	77	3
	Ship	2	24

**Single**

HH

Truth

		Iceberg	Ship
Classified	Iceberg	78	5
	Ship	1	22

**Single**

HH(without shape)

Truth

		Iceberg	Ship
Classified	Iceberg	65	8
	Ship	14	19

## 5 Computational Considerations

The development and implementation of some of the key scientific programming components of this work are presented here. These issues were found to be important to this work. Notable is a demonstration for the need for the leave-one-out cross validation when using small sample size data, benchmarking the ES, the development of the ES variants ERS and LES, parallelization of ES and the implementation of a non-intrusive parallel ES.

### 5.1 *The Necessity for Cross Validation*

As presented in Section 2.3.3, Raudys and Jain [21] summarized the main methods for performance estimation. Three of these are re-substitution, hold-out and cross-validation. And as previously discussed, it was concluded that the cross-validation method is a reasonable compromise given a small number of training samples and a relatively inexpensive DF (such as the maximum-likelihood used here). The following examples demonstrate the shortfalls encountered when using re-substitution and hold-out rather than cross-validation.

Early in the initial stages of this work the re-substitution method was employed. Here, the SFS algorithm was used for feature selection and the maximum-likelihood was used as a discriminant function. Preliminary results for the limited RADARSAT-1 wide data were encouraging as the confusion matrix indicated a near perfect accuracy. Figure 5.1 shows the accuracy assessment results for SFS using both re-substitution and leave-one-out. Post implementation of this version of DF in software, it became apparent that the projected re-substitution accuracy was not being met with the new ground verified targets. It was known at the time that re-substitution was biased. However, the bias was not expected to be as significant as what was observed. This led to the investigation of other methods such as hold-out and cross-validation.

The hold-out method can also be problematic. This is especially true for small sample size cases since every target is important in establishing the multivariate distributions for

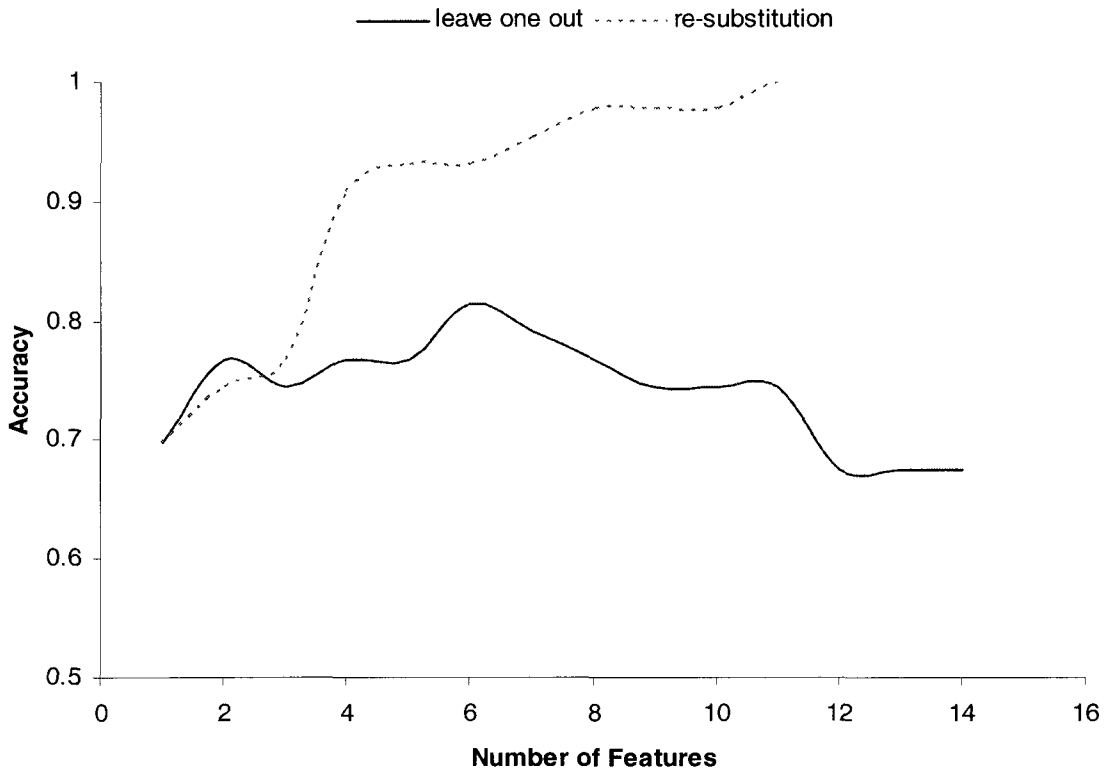


**Figure 5.1:** RADATSAT-1 accuracy for leave-one-out and re-substitution.

its associated class. Table 5.1 shows the leave-one-out, re-substitution and hold-out performance presented in the form of confusion matrices. The hold-out performance was evaluated based on a random split of the available data for the optimal feature space identified using ES methodology.

This significant difference in performance from 90% using the ES leave-one-out to 54% using hold-out is a dramatic demonstration for the need for sample utilization in small sample size problems. Based on these results, when using a maximum-likelihood and a small number of training samples, the cross-validation which minimizes training bias and maximizes sample utilization is recommended. The only notable drawback is the increased cost of using the leave-one-out in the retraining of the DF when evaluating each target. This issue is addressed in the next section.

**Table 5.1:** RADARSAT-1 validation methodologies.

SFS-2C leave-one-out		Truth		SFS-2C re-substitution		Truth	
Classified		Iceberg	Ship	Classified		Iceberg	Ship
		23	4			27	0
	Optimal Feature Space (ES) Retrained using hold out	Iceberg	Ship			0	26
		4	12				
Truth		Iceberg		Iceberg		Ship	
Classified		Iceberg	Ship			9	5
		Ship				5	3

## 5.2 Maximum Likelihood Mean and Covariance Calculation

When evaluating the DF using leave-one-out, the mean vector, covariance matrix, determinant and inverse of the covariance matrix have to exist for each feature subset being evaluated. This is true for all feature selection methods. During development and optimization of the exhaustive search code it was noticed that a significant portion of the exhaustive search work occurred when calculating the mean and covariance for each class. Of specific importance is that the mean and covariance can be calculated up front before any evaluation occurs, producing a mean vector of length  $n$  and covariance matrix of size  $n \times n$ . All evaluations of subsets of features (feature subspaces) can be extracted from the master mean vector and covariance matrix. This can also be extended to a leave-one-out methodology where the mean vector and covariance matrix for each of the  $m$  targets being evaluated is estimated prior to search evaluation. The implementation used here has  $m + k$  mean and covariance matrices calculated up front. This takes negligible memory and computational effort for small sample size problems. The  $k$  extra instances are considered for the mean and covariance calculations necessary for each class using all the class samples. For example, consider the case when an iceberg  $p$  is

being left out and the remaining icebergs and all ships are being used to train: the covariance  $\sim p\_ice$ , mean  $\sim p\_ice$ , covariance  $ship$ , mean  $ship$  are used to build the DF and evaluate the feature space.

Unfortunately, there is no known way at this time to pre-calculate the determinant or inverse for any feature subset combination for the covariance metrics. Thus these need to be calculated during the training phase.

### **5.3 Benchmarking Exhaustive Search**

Unlike the SFS or other suboptimal feature selection algorithms, evaluating the ES can be a significant undertaking. From preliminary trials, it became apparent that it is useful to estimate in advance the computing time an ES would take on a particular data set. This is especially true when considering code parallelization and deciding upon the number of computer processors required for reasonable turnaround times. Here, a simple yet accurate method for doing a benchmark is derived.

Since the implementation of ES is breadth-first, the benchmark also works on the breadth-first premise. Consider that for each feature space their are  $n$ -choose- $k$  permutations. For each permutation of a feature space, the cost of computing the mean vector, covariance, inverse covariance, determinant covariance and discriminant function (DF) evaluation are nominally equal. Thus, the benchmark proposed is based on a fixed number of permutations multiplied by the actual time sampled to build and evaluate each feature space. It is important to note that as the feature space increases the computation time required to train and evaluate will also increase due to the higher dimensionality. Formally, the benchmark takes the form of

$$\sum_{k=1}^n f_k \binom{n}{k} \quad (2.19)$$

where  $n$  is the total number of features,  $k$  is the feature space being evaluated, and  $f_k$  is the benchmarked time required to evaluate one classifier in sample space  $k$  [50].

## **5.4 Variants of Exhaustive Search**

Early work in feature selection focused on SFS and ES. It became obvious early on that SFS had limitations when optimizing a DF and that a more extensive search space such as ES would likely lead to increased classification performance. However, implementing the ES has extensive computational cost. Even for the small sample size problems presented in this work, ES would be on the order of years to complete on a single processor CPU.

Table 5.2 presents a benchmark for the ES on the Envisat AP data set, using an Intel Pentium 4, 2.6 Giga Hertz processor, 3 Giga Bytes of RAM, demonstrating the exponential cost as a function of increasing number of features. This data is in agreement with the theory and benchmarks presented in Section 2.3.2.2. and Section 5.3

From benchmark times such as presented in Table 5.2, it became apparent that feature subsets could be exhaustively evaluated with acceptable turn around times. This lead to the notion that the ES could be scaled down, where for each feature omission there would be was a corresponding exponential decrease in computational requirement. Thus, based on the constraints of a benchmark and a predetermined acceptable run time, a desired feature subset of size  $k$  could be exhaustively evaluated. The feature subset could be selected in a random, ad hoc, or ranked process. Here a ranked approach is explored, where features are ranked in decreasing order based on the SFS ranking. The SFS was selected as a ranking methodology as it naturally produces a feature vector which has a minimum loss / maximum gain ranking based on decreasing order of importance relative to the SFS algorithm.

Thus, the  $n - k$  features removed from the available feature set produces an ES that can be completed in desired time. This search is no longer guaranteed to be globally optimal like the true ES, since the potential exists for the global solution to contain features that were removed in the ranking process. The algorithm for ERS-(  $n - k$  ) is presented in Appendix III.

**Table 5.2:** ES benchmark for ENVISAT AP data.

# of Features	Days
1	0.000001
2	0.000002
3	0.000004
4	0.000008
5	0.000017
6	0.000036
7	0.000073
8	0.000146
9	0.000298
10	0.000600
11	0.001210
12	0.002449
13	0.005027
14	0.010025
15	0.020312
16	0.040940
17	0.082639
18	0.167506
19	0.338998
20	0.682285
21	1.390965
22	2.824745
23	5.743248
24	11.708289
25	23.612310
26	47.941402
27	96.759610
28	194.275616
29	394.708097

A second variant of ES was also implemented. It is based on the notion that a limited portion, or first  $m$  feature spaces (1 to  $m$  space) is relatively computationally inexpensive to evaluate considering the breath-first approach. This method supports the small sample set problem of under-sampling and the curse of dimensionality that occurs in higher order feature spaces. Thus, the first  $m$  spaces can be exhaustively evaluated in desired time (on the order of a day). This search is no longer guaranteed to be globally optimal like the true ES. However, the results are globally optimal for the first  $m$  feature spaces evaluated. The algorithm for limited exhaustive search, LES- $m$  is presented in Appendix IV.

Both ERS and LES variants of ES are systematic and evaluate significantly more feature space when compared to the SFS method. Based on this, they are presented as viable options when considering the feature selection problem and when a more robust method is required.

## **5.5 Non-Intrusive Parallel Exhaustive Search**

The pre-conceived notion that the ES can take months or even years to complete for even small training data sets is often why it is quickly discredited as a reasonable approach to feature selection. However, due to the independence of each feature evaluation, parallelization of the ES is relatively easy to achieve. A small data set, such as the RADARSAT-1 43 samples and 29 features, can take half a year to complete on a single processor (benchmarked on an Intel Pentium 4, 2.6 Giga Hertz processor, 3 Giga Bytes of RAM). If the time to completion is  $\tau$  on a single computer, it will be  $\tau/n$  if  $n$  such computers are used. Thus, the time is reduced by a factor of  $n$ .

Due to the independence of evaluation, message passing and input/output can be essentially independent from each block of search space being evaluated by each processor. For simplicity, each processor can also own its own copy of the data set which the feature selection is being evaluated, and as well, its own results file that records performance gains and their feature permutations. Post completion of the  $n$  processors work, a master data collection process where each computer's results are merged and used to create a master output from which the optimal solution can be extracted.

As a consequence of today's business environment, it is common for a work place to have desktop computers that have relatively modern computing power. This is often coupled with a relatively low continuous usage of this processing power. Unfortunately, these resources are not free to utilize all the time as people need their desktop to work. Thus, it is desirable to find a way to utilize this resource in a non-intrusive way to the computer owner and maximize processing utility. This led to the author's development of the Non-Intrusive Parallel Exhaustive Search (NIES) software for this thesis. The idea is not new,

as it already has a well known implementation through a web-based search for extra-terrestrial intelligence (SETI) screen saver [51].

The implementation developed here is simplified compared to a web-based parallel processor. Each processor has its own screen saver and block of search space to evaluate which is managed though a configuration file. When a computer is idle, the screen saver runs and spawns the ES executable. When the screen saver is interrupted by the user regaining control of their computer, the configuration file is updated, the ES closes, and finally the screen saver closes. The ES program close is accomplished in code by continuously checking the configuration file for screen saver activity status. When ES shuts down, it stores necessary information, such as current iteration number, feature space evaluated and improved performance feature space.

NIES was chosen for two reasons. First, the computer resources were freely available at the author's workplace. Second, the foundation code executable (single processor ES) was easily spawned from screen saver code and expanded to parallel on the data level. Appendix V presents the pseudo code algorithm for parallel ES (PES).

Results from the PES are encouraging and were definitely worthwhile for completion of this research. The time reduction when using PES was linear based on the number of processors, as the benchmark and actual computation times were in agreement. Most beneficial as a pattern recognition practitioner was the comparison of the ES results with that of other much computationally lighter search methods such as LES, ERS and SFS. That is, ES allows the scientist to compare the actual optimal solution combination with that of the optimized solution found with suboptimal methods.

The screen saver implemented here (screen capture shown in Figure 5.2) actually consisted of a set of 107 randomly selected photographs of icebergs that were collected for the ground truth targets in this study. An animated C-CORE logo (2006) starts in a random position on the screen and “bounces” around the screen in a linear fashion until

the user shuts down the screen saver with the click of a mouse button. The screen saver start-up was managed by the Windows 2000 NT and XP operating systems task scheduler. Originally it was planned to load NIES as a screen saver in the Windows environment. However, a screen saver in this environment is “owned” by the operating system. Thus, writing permissions to the user’s hard disk space are restricted. This restriction is not acceptable since the search results and indexing place are required to be updated in the configuration text files. A work-around was implemented using the Windows Task Scheduler. The Task Scheduler supports user-tasked software execution when a computer is idle. Thus, writing permissions to the local hard disk were implicit.



**Figure 5.2:** Non-intrusive parallel exhaustive search (NIES) screen saver

## 6 Conclusion

This thesis work has demonstrated successfully that iceberg and ship discrimination in synthetic aperture radar data is possible. A constant false alarm rate, which is an adaptive threshold method, was used for target detection following the most current accepted CFAR approach. Post target detection, a Bayesian-based maximum likelihood quadratic discriminant approach was adopted for target discrimination. Here, known iceberg and ship samples were used to build the quadratic discriminant functions and were found to produce at least 90% classification accuracy for said targets for the three different sensors: RADARSAT-1, ENVISAT ASAR HH/HV, and EMISAR. These results are essentially unbiased as they were calculated using the cross validation leave-one-out methodology.

Feature selection using the sequential forward selection and exhaustive search variants were found to be successful to optimize feature subspaces when using quadratic discriminant functions. Notably, the sequential forward selection repeatedly produced a “good” feature subset that was obtained in minutes of processing time. Exhaustive search was implemented to find the optimal feature combination, but at a cost where parallelization was necessary to have a run time of two weeks. Non-intrusive parallel exhaustive search software was implemented and demonstrated to be an effective way to achieve optimal feature space evaluation. Variants of the exhaustive search were also developed, the limited exhaustive search and exhaustive ranked search. These were found to produce superior feature selection results compared to sequential forward selection. The only parameter to consider for either of the limited exhaustive search and exhaustive ranked search is the scalable run time based on the user requirements.

RADARSAT-1 iceberg and ship, two class, discrimination was evaluated with three different feature selection methods, sequential forward selection, exhaustive search and exhaustive ranked search. In addition, a four class hierarchy was also developed and evaluated using sequential forward selection. The discrimination results for these four

methods ranged from 81% to 91% accuracy. The optimized feature combination was found commonly by the exhaustive search and exhaustive ranked search feature selection methodology. The two class maximum likelihood model using the five feature space: HV signal-to-clutter ratio, HH variance  $\sigma^0$ , area, structure factor and inner circle radius produced the 91% discrimination accuracy.

ENVISAT HH/HV dual polarization iceberg and ship, two class, discrimination was evaluated with three different feature selection methods, sequential forward selection, exhaustive ranked search and limited exhaustive search. In addition, a six class hierarchy was also developed and evaluated using sequential forward selection. The discrimination results for these four methods ranged from 91.4% to 94.1% accuracy. The optimized feature combination was found with the six class hierarchy methodology. The six class maximum likelihood model was based on a three branch decision, which separated targets based on size and target detection confidence. For small-low intensity (MLDC) targets the maximum likelihood model using the one feature space, anisometry was selected. For medium size targets (< 70 pixels) the maximum likelihood model using the three feature space: HH signal-to-clutter ratio, HV signal-to-clutter ratios and circularity was selected. For large sized targets ( $\geq 70$  pixels) the maximum likelihood model using the two feature space HV signal-to- clutter ratio and HH  $\sigma^0$  variance was selected.

Target size was observed to be an important indirect measure for classification confidence. For example, the ENVISAT iceberg and ship targets greater than 70 pixels were observed to have an error free classification accuracy, while targets less than 70 pixels were expected to be falsely classified 10% of the time. This strongly supports the volume and surface scattering mechanisms for iceberg compared with dominant surface scattering of large metal vessels. Since the scattering mechanisms for these targets are so different, it is expected that the discrimination potential would exist. However, small wooden fishing boats and moderate to small icebergs can produce similar scattering behavior, thus targets with too few pixels, relatively similar radar intensities, and relatively similar shape will always be problematic to discriminate.

It is hard to directly compare the RADARSAT-1 single polarization results to the ENVISAT dual polarization results as they were trained on different samples of icebergs and ships, collected in differing geographical regions, during different years, with different sample frequencies. That said, RADARSAT-1 HH and ENVISAT AP HH/HV produced 90 and 94% accuracies respectively. Thus, the data suggests that a dual polarization HH/HV produces an improved classification over HH alone. This trend is also reflected in the EMISAR data set.

EMISAR iceberg and ship discrimination was evaluated for eight polarization combinations, Quad Pol with Cameron Decomposition, Quad Pol, Dual Pol HH/HV, Dual Pol VV/VH, Dual Pol HH/VV, Single Pol HH, Single Pol VV, and Single Pol HH without shape features. The methodology chosen for rapid algorithm development and evaluation of the aforementioned polarization combinations was sequential forward selection two class maximum likelihood models. The discrimination results for these four methods ranged from 79% to 99% accuracy. Generally, quad polarization (with decomposition) outperformed dual polarization, and dual polarization outperformed single polarization for iceberg and ship classification.

The EMISAR Quad Polarization with Cameron Decomposition feature space optimization selected quarter wave and (the target shape measure) eccentricity. This feature space was found to be almost non-error with 105 of 106 targets correctly discriminated. These results are very promising as the soon-to-be-launched RADARSAT-2 will produce high resolution, quad polarization data similar to that of EMISAR data. From this, we expect that RADARSAT-2 quad polarization modes will have an improved probability of classification for iceberg and ship targets over dual polarization modes.

The EMISAR Dual Polarization results were always better than single polarization. Dual polarization combinations were observed to have a range of classification accuracy ranging from 96 to 97%, with both dual cross polarization combinations (HH/HV OR

VH/VV) nominally outperforming the dual co-polarization. Common features selected by the SFS for all dual polarization combinations were area, orientation, equivalent diameter,  $\sigma^0$  mean and  $\sigma^0$  variance.

The EMISAR single polarization (HH or VV) results range in classification accuracy from 94 to 95%, with VV nominally outperforming HH. As a special case, HH without shape features was also run and produced 79% accuracy.

## 6.1 Future Work

As a continuation to this thesis work, there are several areas that are of interest for future research. These are relevant to iceberg and ship discrimination with SAR data and the general topic of pattern recognition. Specifically:

- $P(\omega_{ue})$  and  $P(\omega_{shp})$  were not estimated in this study. It is believed that these prior probabilities for the iceberg and ship classes would improve the discrimination accuracy of the models presented in this work. However, producing a good “general” estimate for the prior probabilities is expected to be an onerous task. The factors when modeling these prior probabilities is expected to be dominated by geographic location and season. This is based on the expectation for vessel targets to exist geographically near ports, shipping lanes and fishing grounds. As well, the occurrence of icebergs is known to be dependent on seasonal glacial calving rates, prevailing wind conditions, prevailing oceanic currents, sea surface temperatures and bathymetry.
- Current and future spaceborne SAR can be simulated from high resolution, low NESZ, multi polarization airborne SAR data. Such sources for airborne SAR would be from EMISAR as presented in this thesis or the Environment Canada Convair-580 SAR. This work would validate the expected decrease in discrimination potential as a function of resolution, NESZ and polarization. This methodology would remove potential sample bias when trying to compare results collected with different sensors.

- A feature selection software package for pattern recognition can be developed. Of interest would be to support benchmarking and running the sequential forward selection, genetic algorithm, exhaustive ranked search, limited exhaustive search, and exhaustive search feature selection applications. It would also be desired to support parallel processing of these algorithms based on modern multi core desktop architectures.
- An  $n$ -class algorithm that specifically models icebergs, ships, sea ice, land, and ocean SAR targets can be developed. This would be first investigated by a  $n$ -class maximum likelihood approach.
- Other discrimination methodologies should be evaluated such as linear discriminant, nearest neighbor, neural networks and support vector machines for iceberg and ship discrimination. Further to this, compare the above evaluations with the maximum likelihood-quadratic discriminant results found in this thesis.
- An investigation into HV target detection can be evaluated. Iceberg and ship detection has traditionally focused on shallow incidence angles in HH and VV based on maximizing the target signature-to-clutter ratio. Based on observed ASAR HV imagery, the NESZ dominates the background signature and is largely invariant of wind conditions but dependant more on the deterministic noise floor constraints of the sensor. Thus, a target collected under certain wind conditions, incidence angles and favorable NESZ levels could have improved delectability in the HV channel over HH or VV.

## 7 References

- [1] Haykin, S., Currie, B., Ukrainec, A. *Development of a Neural Network Processor for the Improved Radar Detection of Vessels in a High Sea Clutter Environment – Phase I*, McMaster University, 1996.
- [2] Vachon, P., Campbell, J., Bjerkelund, C., Dobson, F., Rey, M. “Ship detection by the RADARSAT SAR: validation of detection model predictions,” *Canadian Journal of Remote Sensing*, vol. 23, no. 1, p. 48-59, 1997.
- [3] Randell, C., Rokonuzzaman, M., Youden, J., Khan, R. “Evaluation of RADARSAT for detection, classification and discrimination of icebergs,” in *proceedings of Agency Application Development and Research Opportunity (ADRO) Symposium*, Canadian Space Agency, 1999.
- [4] Murthy, H. and Haykin, S. “Bayesian classification of surface-based ice-radar images,” *IEEE Journal of Oceanic Engineering*, vol.12, no. 3, p. 493-502, 1987.
- [5] Orlando, J., Mann, R., Haykin, S. “Classification of sea-ice images using a dual-polarized radar,” *IEEE Journal of Oceanic Engineering*, vol.15, no. 3, p. 228-237, 1990.
- [6] Power, D., Youden, J., Lane, K., Randell, C., Flett, D. “Iceberg detection capabilities of RADARSAT synthetic aperture radar,” *Canadian Journal of Remote Sensing*, vol. 27, no. 5, p. 476-486, 2001.
- [7] Cameron, W.L., Youssef, N., Leung, L.K. “Simulated polarimetric signatures of primitive geometrical shapes,” *IEEE Transactions on Geoscience and Remote Sensing*, vol. 34, no. 3, p. 793-803, 1996.
- [8] Cameron, W. and Leung, L. “Feature motivated polarization scattering matrix decomposition,” in *Proceedings of IEEE 1990 International Radar Conference*, p. 549-557, 1990.
- [9] Cloude, S. and Pottier, E. “A Review of Target Decomposition Theorems in Radar Polarimetry,” *IEEE Transactions on Geoscience and Remote Sensing*, vol. 32, no. 2, p. 498-518, 1996.
- [10] Van Zyl, J, “Unsupervised Classification of Scattering Behaviour Using Radar Polarimetry Data,” *IEEE Transactions on Geoscience and Remote Sensing*, vol. 27, no. 1, p. 36-45, 1989.

- [11] Touzi, R. and Charbonneau, F. “Characterization of Target Symmetric Scattering Using Polarimetric SAR,” *IEEE Transactions on Geoscience and Remote Sensing*, vol. 40, no. 11, p. 2507-2516, 2002.
- [12] Lillesand, T. and Kiefer, R. *Remote Sensing and Image Interpretation, 4<sup>th</sup> Edition*, New York, Wiley, 2000.
- [13] Skolnik, M. *Radar Handbook*, McGraw Hill, Ontario, Canada, 1990.
- [14] Holt, B. “SAR Imaging of the oceans surface,” in *Synthetic Aperture Radar Marine User's Manual*, C. Jackson, J. Apel, Eds. US department of Commerce, 2004.
- [15] Curlander, J. and McDonough, R. *Synthetic aperture radar: systems and signal processing*, New York, Wiley, 1991.
- [16] Lewis, E., Currie, B., Haykin, S. *Detection and Classification of Ice*, New York, Wiley, 1987.
- [17] Haykin, S., Lewis, E., Raney, R., Rossiter, J. *Remote Sensing of Sea Ice and Icebergs*, New York, Wiley, 1994.
- [18] Lane, K., Power, D., Chakraborty, I., Youden J., Randell, C. “RADARSAT-1 Synthetic Aperture Radar Iceberg Detection Performance ADRO-2 A223,” in Proceedings of the International Geoscience and Remote Sensing Symposium, vol. 4, p. 2273-2275, 2002.
- [19] Gonzalez, R. and Woods, R. *Digital Image Processing (second Edition)*, Prentice Hall, New Jersey, 2002.
- [20] Duda, R., Hart, P., Stork, D. *Pattern Classification, 2nd edition*, John Willey and Sons Inc., 2001.
- [21] Raudys, S. and Jain, A. “Small Sample Size Effects in Statistical Pattern Recognition: Recommendations for Practitioners,” *IEEE Transactions on Pattern Analysis and Machine Intelligence*, vol. 13, no. 3, p.252-264, 1991.
- [22] Jain, A. and Zongker, D. “Feature Selection: Evaluation, Application, and Small Sample Performance,” *IEEE Transactions on pattern analysis and machine intelligence*, vol. 19, no. 2, p. 153-158, 1997.
- [23] Jain, A. and Chandrasekaran, B. “Dimensionality and sample size considerations,” in *Proceedings of the Pattern Recognition Practice*, vol. 2, no. 39, p. 835-855, 1982.
- [24] Dash, M. and Liu. H. “Feature Selection for Classification,” *Intelligent Data Analysis*, vol. 1, p. 131-156, 1997.

- [25] Aha, D. and Bankert, R. “A comparative Evaluation of Sequential Feature Selection Algorithms,” *Learning from Data: AI and statistics*. Edited by Fisher and Lenz, 1996.
- [26] Inza, I., Larrañaga, P., Etxeberria, R., Sierra, B. “Feature Subset Selection by Bayesian network-based optimization,” *Artificial Intelligence*, vol.123, p. 157-184, 2000.
- [27] Kittler, J. “Feature Set Search Algorithms,” in *Proceedings of Pattern Recognition and Signal Processing*, p. 41-60, 1978.
- [28] Cover, T. and Van Campenhout, J. “On the Possible orderings in the Measurement selection problem,” *IEEE Transactions Systems, Man, and Cybernetics*, vol. 7 no. 9 p. 657-661, 1977.
- [29] Liu, H. and Motoda, H. *Feature Selection, for knowledge discovery and data mining*. Kluwer Academic Publishers, Massachusetts, 1998.
- [30] Hoffbeck J. and Landgrebe, D. “Covariance matrix Estimation and Classification with Limited Training Data,” *IEEE Transactions on Pattern Analysis and Machine Intelligence*, vol. 18, no. 7, p.763-767, 1996.
- [31] Marthaler, Lt. J. and Heighway, J. “Radar Image Processing of Real Aperture SLAR Data for the Detection and Identification of Iceberg and Ship Targets,” *5<sup>th</sup> Canadian Symposium on Remote Sensing*, p. 483-494, 1978.
- [32] Vachon, P. and Olsen R. “RADARSAT SAR mode selection for marine applications,” *Backscatter, Newsletter of the Atlantic Centre for Remote Sensing of the Oceans*, vol. 6, no. 3, p. (3-4, 18), 1995.
- [33] Vachon, P., Thomas, S., Cranton, J., Edel, H., Henschel, M. “Validation of Ship Detection by the RADARSAT Synthetic Aperture Radar and the Ocean Monitoring Workstation,” *Canadian Journal of Remote Sensing*, vol. 26, no. 3, p. 200-212, 2000.
- [34] Freeman, N., Gray, A., Hawkins, R., Livingstone, C. “Canada Center for Remote Sensing (CCRS) Convair 580 results relevant to ERS-1 wind and wave calibration,” *Proceedings of an ESA Workshop on ERS-1 Wind and Wave Calibration*, p. 101-109, 1986.
- [35] Lane, K., Power, D., Youden J., Randell, C., Flett D. “Validation of Synthetic Aperture Radar for Iceberg Detection in Sea Ice,” in *Proceedings of the International Geoscience and Remote Sensing Symposium*, vol. 1, p.126-128, 2004.

- [36] Howell, C., Youden, J., Lane, K., Power, D., Randell, C., Flett, D. “Iceberg and Ship Discrimination with ENVISAT Multi-Polarization ASAR,” in *Proceedings of the International Geoscience and Remote Sensing Symposium*, vol. 1, p.13-16, 2004.
- [37] Watts, S. “Radar detection prediction in sea clutter using the compound  $K$ -distribution model,” in *Proceedings of the IEEE Communications, Radar and Signal Processing*, vol. 132, no. 7, p. 613-620, 1985.
- [38] Johnson, N. and Kotz, S. *Continuous Univariable Distributions*. New York, Houghton Mifflin, 1970.
- [39] Orlando, J. *Classification of radar returns from sea ice*. M.Eng Thesis, McMaster University, Hamilton, Ontario, Canada, 1989.
- [40] MDA Website. “MDA Geospatial Services, Essential Information Solutions, Overview.” Available at, <http://gs.mdacorporation.com/>, July 2006.
- [41] *RADARSAT USERS GUIDE*, RADARSAT International, 1998.
- [42] ESA Website, “Missions, ENVISAT Tour, ASAR.” Available at, <http://ENVISAT.esa.int/instruments/tour-index/>, July 2006.
- [43] *ASAR Hand Book*, European Space Agency, 2006.
- [44] Technical University of Denmark Website. “The EMISAR Sensor.” Available at, [http://www.oersted.dtu.dk/English/research/emi/dcrs/airborne\\_sensors/emisar.aspx](http://www.oersted.dtu.dk/English/research/emi/dcrs/airborne_sensors/emisar.aspx), July 2006.
- [45] Livingstone, C., Gray, A., Hawkins, R. Vachon, P. Lukowski, T. Lalonde, M. “CCRS airborne SAR systems: radar for remote sensing research,” *Canadian Journal of Remote Sensing*, vol. 21, no. 4, p. 468-491, 1995.
- [46] Staples, G. and Sanden, J. “RADARSAT-2 Polarimetric Applications,” *Anais XI SBSR*, Brazil, 2003.
- [47] University of Maryland Website. “Global Land Cover Facility.” Available at, <http://glcf.umiacs.umd.edu/data/>, July 2006.
- [48] Touzi, R., Charbonneau, F., Hawkins, R., Vachon, P. “Ship Detection and characterization using polarimetric SAR,” *Canadian Journal of Remote Sensing*, vol. 30, no. 3, p. 552-559, 2004.

- [49] Novak, L., Owirka, G., Netishen, C. “Performance of a High-Resolution Polarimetric SAR Automatic targets Recognition System,” The Lincoln Laboratory Journal, vol. 6, no. 3, p.11-24, 1993.
- [50] Howell, C., Mills, J., Power, D., Youden, J., Dodge, K., Randell, C., Churchill, S., and Flett, D.. “A Multivariate Approach to Iceberg and Ship Classification in HH/HV ASAR Data,” in *Proceedings of the International Geoscience and Remote Sensing Symposium*, 2006.
- [51] Search for extra-terrestrial intelligence (SETI) Website. “SETI at Home.” Available at, <http://www.seti.org/site/pp.asp?c=ktJ2J9MMIsE&b=179086>, July 2006.

## **Appendix I – Pseudo code algorithm for Sequential Forward Selection (SFS)**

1.  $FS \{ \}$
2.  $TS \{ f_1, f_2, \dots, f_n \}$
3. FOR  $i = 1$  TO  $n$ 
  - a.  $accuracy = 0$
  - b.  $bestFeature = \{ \}$
  - c.  $bestAccuracy = 0$
  - d. FOR  $j = 1$  TO  $\text{length}(TS)$ 
    - i.  $ES = TS(j) \cup FS$
    - ii. Train Discriminant Functions for feature space  $ES$
    - iii. Calculate  $accuracy$  from Discriminant Functions ( $ES$ )
    - iv. IF ( $accuracy > bestAccuracy$ )
      1.  $bestAccuracy = accuracy$
      2.  $bestFeature = TS(j)$
    - v. END
  - e. END
  - f.  $bestFeature$  assigned to  $FS$
  - g.  $bestFeature$  removed from  $TS$
4. END

## Appendix II - Pseudo code algorithm for Exhaustive Search (ES)

1.  $FS \{ \}$
2.  $nIterations = 2^n - 1$
3. FOR  $i = 1$  TO  $nIterations$ 
  - a. **incrementFS**( $FS$ )
  - b. Train Discriminant Functions for feature space  $FS$
  - c. Calculate *accuracy* from Discriminant Functions ( $ES$ )
  - d. IF ( $accuracy > bestAccuracy$ )
    - i.  $bestAccuracy = accuracy$
    - ii.  $bestFeatureSet = ES$
  - e. END
4. END

```
function vec = incrementFS(vec,nFeat)

sVec = length(vec);
vec(sVec) = vec(sVec) + 1; % increment combination

if(vec(sVec) > nFeat)
vec(sVec) = vec(sVec) - 1; %
% decrement combination, combination over : low...
%
if( ((nFeat-sVec + 1):nFeat) == vec) % new dimension
if(sVec < nFeat) % catch the end of the iteration...
    vec = 1 : (sVec + 1);
end
else % bump the index...
    i = sVec;
    while(vec(i) == vec(i-1) + 1) %increment the bump location
        i = i - 1;
    end
    i = i - 1;
    vec(i) = vec(i) + 1; % increment the index
    vec(:) = [vec(1:i-1), vec(i) : ((sVec-i)+vec(i))]; %
    % finish the vector from the index to the end sequentially
end
end
```

## **Appendix III - Pseudo code algorithm for Exhaustive Ranked Search (ERS)**

1. benchmark computer
2. define acceptable work time
3. feature reduction from  $\{f_1, f_2, \dots, f_n\}$  to some subset  $\{f_1, f_2, \dots, f_m\}$ ,  $m < n$ ,  
(e.g. via SFS) to match acceptable work time<sup>1</sup>
4. Run algorithm for ES (Appendix II) working on  $F_{\text{sub}}$

---

<sup>1</sup> Based on benchmark presented in Section 5.3

## **Appendix IV - Pseudo code algorithm for Limited Exhaustive Search (LES)**

1. benchmark computer
2. define acceptable work time
3.  $nIterations$  is set to match acceptable work time<sup>1</sup>
4. Run algorithm for ES ( Appendix II ) working on new  $nIterations$

---

<sup>1</sup> Based on benchmark presented in Section 5.3

## Appendix V - Pseudo code algorithm for Parallel Exhaustive Search (PES)

1. allocate computer resources{C<sub>1</sub>,C<sub>2</sub>,...,C<sub>n</sub>}
2. benchmark computer resources{C<sub>1</sub>,C<sub>2</sub>,...,C<sub>n</sub>}
3. load balance computer resources{C<sub>1</sub>,C<sub>2</sub>,...,C<sub>n</sub>}
4. FS is the working feature set {f<sub>1</sub>,f<sub>2</sub>,...,f<sub>n</sub>}
5. BEGIN PARALLEL: Distribute search (C<sub>1Start</sub>,C<sub>1Stop</sub>, ..., C<sub>nStart</sub>,C<sub>nStop</sub>)
6. calculate FS for C<sub>k</sub>
7. FOR i = C<sub>kStart</sub> TO C<sub>kStop</sub>
  - a. **incrementFS(FS)**
  - b. Train discriminant functions for feature space FS
    - i. Calculate *accuracy* from discriminant functions (ES)
    - ii. IF (*accuracy*>*bestAccuracy*)
      1. *bestAccuracy* = *accuracy*
      2. *bestFeatureSet* = ES
    - iii. END
  - c. END
8. END PARALLEL
9. data merge {C<sub>1</sub>,C<sub>2</sub>,...C<sub>n</sub>} results

## Appendix VI - Confusion Matrix Notation

One way for measuring the class truth data versus classification output is through a confusion matrix (Table AVI.1). The confusion matrix is set up such that all samples are allocated to a finite set of possible truth and classification combinations. Truth is the real world existence of the samples, whereas classification is the predicted class from the algorithm output.

One performance measure that can be calculated from confusion matrices is the classification accuracy, denoted as  $A$  in Equation A.1, which is a measure of how often the classifier is correct. Another performance measure is the class precision, or  $CP$  in Equation A.2, which is a measure of the rate of classification correctness for a class. The true positive, or  $TP$  in Equation A.3, is a measure of how often a target was correctly classified. False positive and overall error measures calculated as  $(1-TP)$  and  $(1-A)$ , respectively.

$$A = \frac{\sum \text{Matrix Diagonal}}{\sum \text{All Samples}} = \frac{\sum_{i=1}^n C(i,i)}{m} \quad (\text{A.1})$$

$$CP_{(i)} = \frac{C(i,i)}{\sum_{j=1}^n C(i,j)}, i \in \{1, \dots, n\} \quad (\text{A.2})$$

$$TP_{(j)} = \frac{C(j,j)}{\sum_{i=1}^n C(i,j)}, j \in \{1, \dots, n\} \quad (\text{A.3})$$

Accuracy is an acceptable measure for overall performance and can be used as an evaluation function in feature selection algorithms; however, it can be misleading when classes with a large sample size are classified with a high level of precision and classes with smaller sample size are classified with a low level of precision. In other words, the

**Table AVI.1:** Class confusion matrix for an  $n$  class system

		Truth			
Classification		Class 1	Class 2	...	Class n
	Class 1	C(1,1)	C(1,2)	...	C(1,n)
	Class 2	C(2,1)	C(2,2)	...	C(2,n)
	...	...	...	...	...
	Class n	C(n,1)	C(n,2)	...	C(n,n)

accuracy could be relatively high even though a particular class was relatively poorly classified. If the sample size for each class is the same, then this problem does not exist.





